Energy & Environmental Science

Carbon Dioxide and Nitrogen Reduction Reactions using 2D Transition Metal Dichalcogenide (TMDC) and Carbide/Nitride (MXene) Catalysts

Journal:	*Energy & Environmental Science*
Manuscript ID	EE-REV-10-2021-003211
Article Type:	Review Article
Date Submitted by the Author:	13-Oct-2021
Complete List of Authors:	Li, Zhaodong; National Renewable Energy Laboratory Attanayake, Nuwan; National Renewable Energy Laboratory Blackburn, Jeffrey; NREL, miller, elisa; national renewable energy laboratory, chemical and nano science center

Carbon Dioxide and Nitrogen Reduction Reactions using 2D Transition Metal Dichalcogenide (TMDC) and Carbide/Nitride (MXene) Catalysts

Zhaodong Li[#], Nuwan H. Attanayake[#], Jeffrey L. Blackburn*, Elisa M. Miller*

Materials and Chemical Science and Technology Directorate, National Renewable Energy Laboratory, Golden, CO 80401

[#] authors contributed equally
^ corresponding authors: Jeffrey.Blackburn@nrel.gov and Elisa.Miller@nrel.gov

Abstract

Improving carbon dioxide and nitrogen reduction reactions (CO_2RRs and NRRs) can reduce anthropogenic greenhouse gas emissions while selectively producing chemicals needed for the fuel, plastic, and chemical industries. Efficient CO_2RRs can be used to replace fossil fuels as well as repurpose captured CO_2, while new NRR pathways can be used to supplement or replace the energy intensive Haber-Bosch process for NH_3 generation with no CO_2 emissions. Therefore, this review article focuses on (photo)electrocatalytic and photocatalytic conversion of CO_2 and N_2 molecules into useful products, such as carbon monoxide, methanol, formic acid, and ammonia, using 2D transition metal dichalcogenides (TMDCs) and metal carbides/nitrides (MXenes). These highly tunable 2D catalysts will be evaluated for their ability to selectively and efficiently undergo CO_2RR and NRR by controlling defects, phases, edge sites, interfaces, and functional groups. We first address the CO_2RR and NRR challenges, with a particular focus on theoretical mechanisms and minimum energy pathways. We follow this discussion with a detailed review of state-of-the-art 2D TMDC and MXene experimental catalysts for CO_2RR and NRR (photo)electrocatalytic and photocatalytic reactions, and then address areas of opportunity for these catalytic reactions.

1. Introduction

Motivated by growing environmental concerns and the demand of sustainable feedstocks in the chemical sector, carbon dioxide reduction reactions (CO_2RR)[1] and nitrogen reduction reactions (NRR)[2] have garnered significant attention. Improving these catalytic production processes could reduce anthropogenic CO_2 and replace/supplement the Haber–Bosch process, the industrial ammonia (NH_3) production process that consumes ~1–2% of the world's energy production and is responsible for ~1% of anthropogenic greenhouse gas emissions[3] (Scheme 1). While many new catalysts are being researched and developed to overcome these challenges, more progress needs to be made before these catalysts are widely deployable. One promising class of materials for such catalytic reactions are two-dimensional (2D) layered materials.

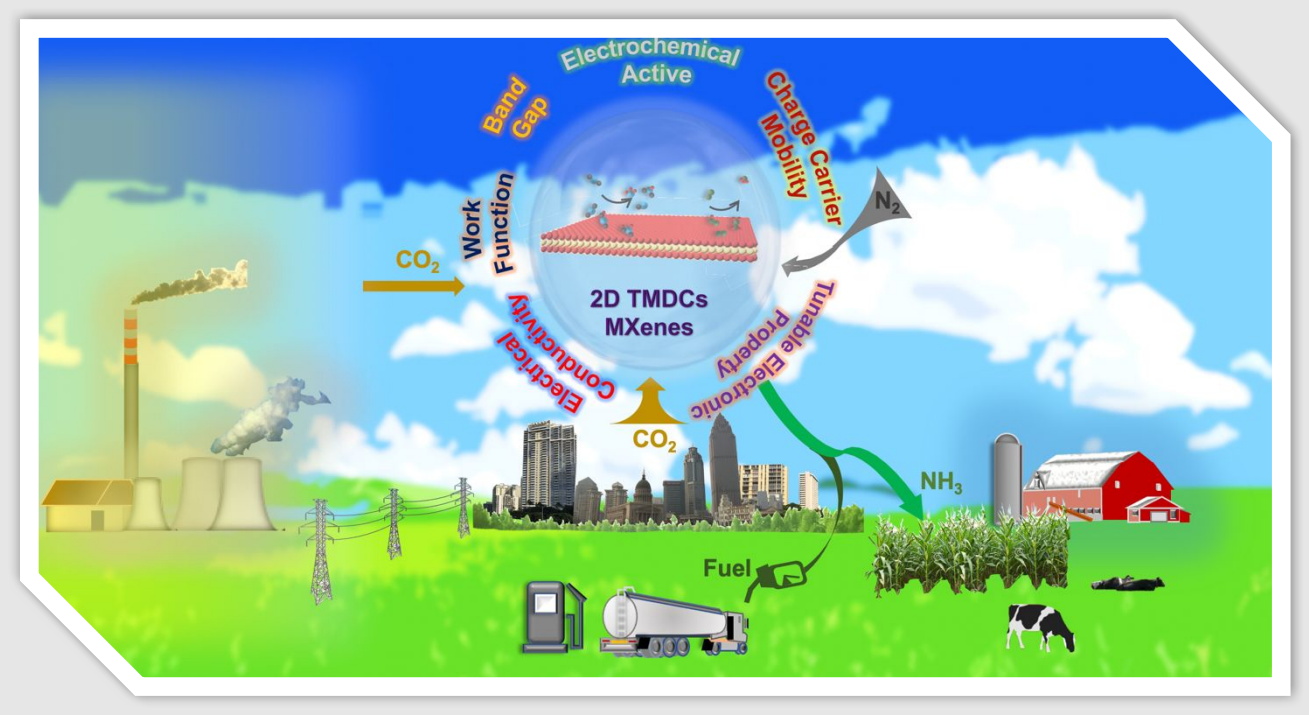

Scheme 1. Future CO_2RR and NRR by novel 2D layered catalysts for sustainable feedstocks and fuels.

Since graphene was successfully isolated from graphite in 2004, 2D materials (quantum confined in one dimension only) have thrived due to their intriguing mechanical, chemical, electronic, and optical properties.[4-8] Building on the appeal of graphene, several other 2D materials have received a surge of interest, such as 2D transition metal dichalcogenides (TMDCs), 2D transition metal carbides/carbonitrides/nitrides (MXenes), Xenes (such as silicene, stanene, and germanene), 2D hexagonal boron nitrides (h-BNs), 2D metals, phosphorenes, graphynes, covalent organic frameworks (COFs), and 2D metal−organic frameworks (MOFs).[9-16] We focus in this review on 2D TMDCs and MXenes, since they are highly tunable, relatively easy to synthesize/exfoliate, light-active, and cost-effective compared to other classes of 2D materials. Additionally, they are composed of transition metal catalysts (e.g. Mo and W), which can be catalytically active. TMDCs have the general formula MX_2, where M is a transition metal (*e.g.,* Mo or W) and X is a chalcogen (*i.e.,* S, Se, or Te). MXenes have the typical formula of $M_{n+1}X_nT_x$, where M is an early transition metal, X is carbon and/or nitrogen, and T is a surface functional group (*e.g.*, O, OH, and/or F).[17]

TMDCs and MXenes are attractive for a number of catalytic applications – including water splitting, CO_2RR, and NRR – for several reasons. First, theoretical simulations have predicted that the coordinated active sites on 2D TMDCs and MXenes lower the activation energy barriers for chemisorption and hydrogenation of gaseous molecules (*e.g.,* CO_2 and N_2), which significantly overcomes the sluggish kinetics and poor selectivity of the reactions.[18, 19] Second, the surface structures, electronic states, and mechanical properties of TMDCs and MXenes are generally more tunable than other 2D materials to target different reactions and reduce unwanted side reactions, *e.g.,* the hydrogen evolution reaction (HER).[20, 21] Specifically, rich tunability of the electronic structure of the TMDCs and MXenes results from (1) the ability to combine numerous transition

metal atoms with non-transitional metal atoms, (2) additional tunability via doping or alloying, and (3) phase engineering via doping, strain, etc. Third, the typical transition metal elements in TMDCs and MXenes, W and Mo for example, are roughly 250 times more abundant in the earth's crust than Pt and Ru (traditional metal catalysts). Sulfur is also an abundant element, and while Se is less abundant than S (by ~3 orders of magnitude), it is ten times more abundant than Pt and Ru and is typically produced as a byproduct of mining metal sulfide (e.g. copper sulfide) ores.[22] All of these advantages suggest that 2D TMDCs and MXenes may be promising catalysts for eco-friendly chemical conversion to produce fuels and value-added chemicals under mild conditions. In recent years, 2D TMDCs especially have led to a breakthrough in catalytic studies, specifically water splitting, hydrocarbon fuel output, and chemical feedstock production.[19, 23, 24] While less studied for catalytic applications than TMDCs, MXenes have a number of attractive properties for heterogeneous catalysis and are now finding their way into pioneering fundamental and applied studies.[25]

To frame the research needed to realize commercially viable 2D catalysts, it is important to note that heterogeneous catalysis relies upon a delicate balance of the thermodynamics and kinetics of surface-reactant interactions. A highly efficient and selective catalytic surface can be designed by optimizing the substrate↔reactant interaction strength per the Sabatier principle: strong enough to drive a reaction forward by absorbing the reactants, but weak enough to regenerate the catalytic surface by desorbing the products.[26] As such, appreciable research on 2D TMDCs and MXenes catalysis has focused on surface activation, charge separation and transport, and electronic structure manipulation for redox reactions. For example, the electronic and crystal structures of certain 2D TMDC compounds can be tuned by phase engineering and optimized for catalytic reactions.[27] Many fundamental and applied studies have focused on metallic TMDCs,

which feature higher conductivity and activated basal plane sites.[28] In contrast, many studies on semiconducting TMDCs search for mechanisms that improve charge transport and the activity of (typically inactive) basal plane sites. In this vein, surface functionalization, defect engineering, and doping have emerged as potential routes towards tuning catalytic active sites on both the edge and basal planes.[29, 30] TMDCs can also be integrated with nanoparticles and single-atom catalysts to trigger catalytic activity by forming new electronic states.[31] Similar to 2D TMDCs, modification of surface termination and heteroatom incorporation of 2D MXenes are mainly applied to optimize the chemical and electronic configurations of active sites for intrinsically enhanced catalytic kinetics.[32, 33] Fabrication of various nanostructures, heterostructures, and hybrid interfaces for increased density and accessibility of active sites is another common method for superior 2D catalysts.[28, 34]

Several recent reviews have covered either advanced CO_2RR and NRR catalysts by using 2D materials other than TMDCs and MXenes (*e.g.*, graphene, g-C_3N_4, CuS, $ZnIn_2S_4$, layered double hydroxides (LDHs))[35-37] or electrochemical HER and pollution degradation catalysts by 2D TMDCs and MXenes.[38-41] However, there is a gap in the literature reviewing 2D TMDCs and MXenes for CO_2RR and NRR. The reported yields and Faradaic efficiencies for CO_2 RR and NRR are quite low, but there is a lot of space and opportunity to learn from these transition metal-based catalysts, which could lead to large-scale deployment. When compared to other 2D materials, there are more variables on 2D TMDCs and MXenes that can be adjusted to manipulate binding sites and reaction pathways to increase Faradaic efficiencies and yield rates. The aim of this review article is to highlight the potential of these two broad classes of 2D materials that arises from this tunability. Moreover, it is necessary for a review of the current mechanistic understanding, much of its theory-based, of reduction reactions within the transition metal-based 2D materials. As such,

we hope that this grouping of 2D TMDCs and MXenes can identify additional mechanistic understanding that still needs to be gleaned (especially experimentally), both for these materials and generally for 2D nanostructures in catalytic CO_2RR and NRR. Challenges and opportunities still exist in 2D TMDC and MXene catalysts for CO_2RR and NRR, which will be thoroughly discussed below.

This review article focuses on (photo)electrochemical and photochemical CO_2RR and NRR using 2D TMDCs and MXenes. Electrochemical reactions utilize electricity from an external circuit (Scheme 2a), photoelectrochemical reactions use both electrical and photon energy (Scheme 2b), and photochemical catalytic reactions utilize only photon energy (Scheme 2c). The structure, optoelectronic properties, and synthesis of 2D TMDC- and MXene-based catalysts will be introduced in **Section 2**. Then the features of CO_2RR state-of-art achievements using 2D TMDC and MXene catalysts are reviewed with separate discussions on the CO_2RR mechanism and the (photo)electrochemical/photochemical processes in **Section 3**. **Section 4** provides a comprehensive review of 2D TMDC and MXene catalysts for NRR and addresses the remaining challenges in this field, which includes selectivity, Faradaic efficiencies, and impurities. Finally, in Section 5, we will provide a summary and outlook highlighting opportunities for 2D TMDC and MXene catalysts in (photo)electrochemical and photochemical systems.

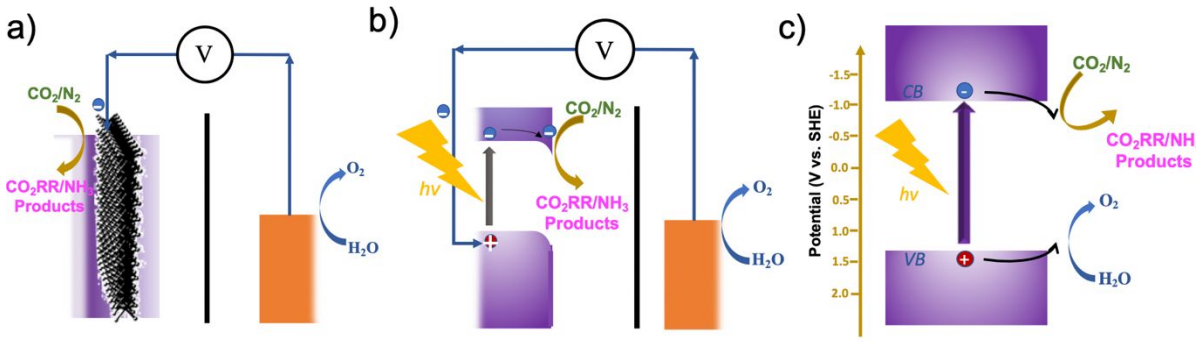

Scheme 2. Schematic of a) electrochemical catalytic, b) photoelectrochemical catalytic, and c) photochemical CO_2 reduction when 2D materials are applied as the catalyst.

2. Structure and electronic properties as well as synthesis of 2D TMDCs and MXenes

2.1 Classification of 2D layered materials

In 2D layered materials, each layer is held together by van der Waals (vdW) forces along the crystallographic c-axis; therefore, the thickness of these materials is increased by incremental amounts that are determined by the thickness of one layer (monolayer). From the bulk, it is possible to apply sheer mechanical stress[42] or chemical methods[43] to exfoliate the bulk material to obtain few-layer and monolayer sheets due to the weak vdW forces[44].

2.2 Structure and electronic properties

2.2.1 TMDCs

The most common TMDCs are composed of Mo or W as the transition metal and S or Se as the chalcogenide; therefore, we will be detailing properties of TMDC materials by using these Mo and W series as examples unless otherwise specified. Modification of interlayer interactions,[45-47] symmetry elements, and quantum confinement of carriers in these few-layer to monolayer materials yields unique physical and electronic properties relative to their bulk counterparts. For example, during the transition of bulk MoX_2 and WX_2 to monolayer, the electronic structure evolves from an indirect to a direct bandgap. For the monolayer, this direct bandgap is accompanied by strong photoluminescence (PL), large exciton binding energy, and high charge carrier mobility.[48-51] These characteristics make these materials attractive candidates in a variety of opto-electronic devices such as solar cells, light emitting diodes, phototransistors, photodetectors, chemical sensors, and logic applications.[50, 52-57] TMDCs also have the ability to intercalate ions/atoms in the vdW gaps (between layers), making them strong candidates for energy

storage devices such as supercapacitors.[58-61] Moreover, these unique and tunable properties make TMDCs great candidates for facilitating various catalytic reactions.[45, 47]

TMDCs are generally found in three polymorphic forms: hexagonal, tetragonal, or rhombic. Hexagonal (2H or 1H), where 2H refers to 2 or more layers and 1H refers to monolayer, has trigonal prismatic coordination of chalcogen atoms around the transition metal, tetragonal (1T) has octahedral coordination of the chalcogen atoms around the transition metal, and less common rhombic (3R) has trigonal prismatic coordination around the transition metal.[50] The number used to denote each phase is the number of layers along the crystallographic plane that comprise a repeating stacking unit, and the letter refers to the symmetry (Fig. 1a). 2H TMDCs have a point group of D_{3h}, 1T TMDCs have a point group of D_{3d}, and 3R TMDCs have a point group of C_{3v}. For the most common TMDCs, 2H and 3R are semiconducting, while the 1T phase is metallic.

For MoS_2, the symmetry-induced ligand field splits the Mo 4d orbitals into three states in 2H and 3R (Fig. 1b); the filled, non-degenerate lower energy $4d_z^2$ orbital leads to the semiconducting properties observed for 2H and 3R MoS_2. In the case of metallic 1T-MoS_2, the ligand field splitting of the 4d orbitals results in two states: the three lower energy degenerate Mo $4d_{xy, yz, xz}$ orbitals and two higher energy unoccupied Mo $4d_z^2$ and $4d_{x^2-y^2}$ orbitals (Fig. 1c). The lower energy, degenerate orbitals are incompletely occupied by two electrons, leading to a metallic ground state and unstable 1T phase.[62]

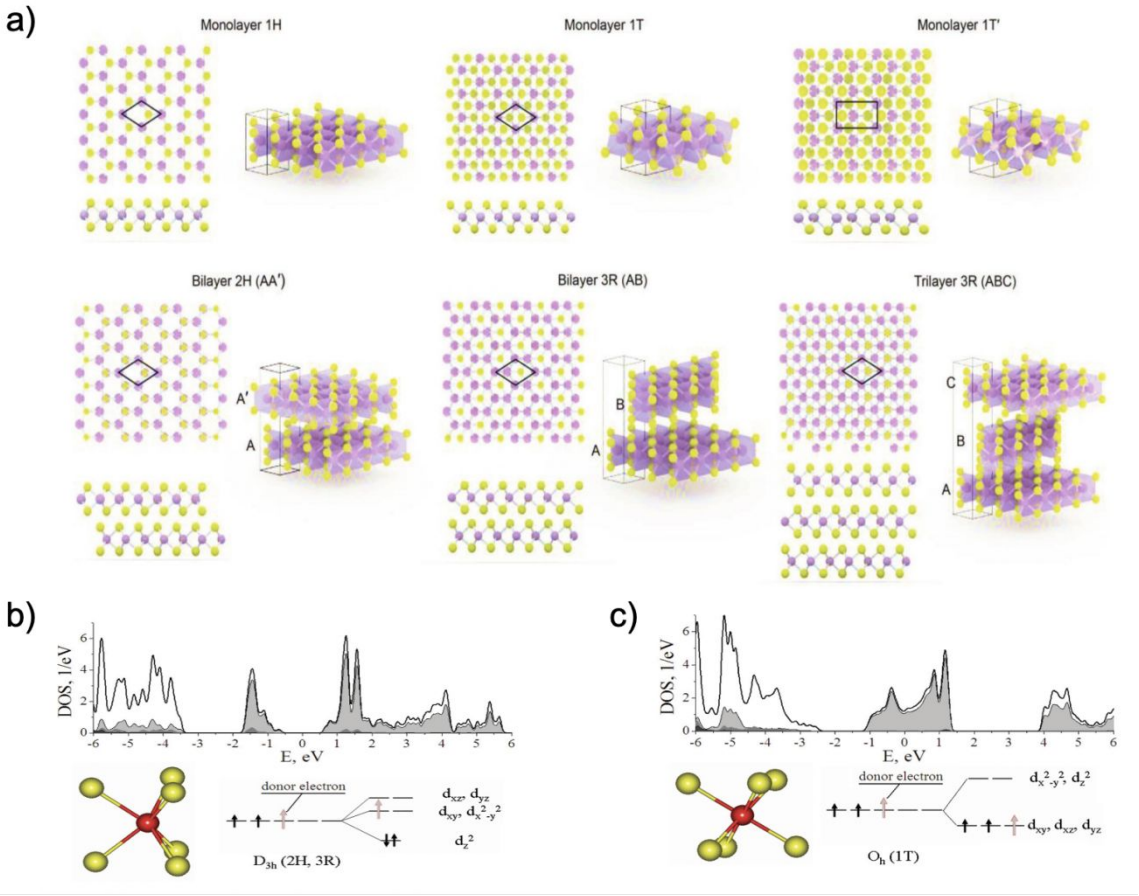

Fig. 1. a) Atomic arrangements of the polymorphic forms of MoS_2. Top row shows atomic models of monolayer 1H, 1T, and 1T', respectively, and bottom row shows the arrangement of atoms and layers in bilayer 2H and 3R as well as trilayer 3R respectively. Reprinted with permission.[63] Copyright 2011 American Chemical Society**.** The density of states (DOS) and orbital configuration with electron occupancy for the b) 2H/3R and c) 1T MoS_2 phases, the pink arrows denote the occupancy of a donor electron in each structure. Reprinted with permission.[62] Copyright 2018 John Wiley and Sons.

It has been found that in most cases the 1T structure observed in MoS_2 is not stable and distorts to the 1T' phase.[63] This distortion is a result of Mo atoms clustering in pairs in a zig-zag Mo-Mo path along the *a* lattice direction (Fig. 1a).[63] The resulting distortion is considered to be a (2x1) superlattice structure of the 1T lattice. Computation results indicate that the 1T' structure is more stable than the 1T structure by 0.30 eV per Mo atom, but 0.57 eV higher in energy than the corresponding 2H phase per Mo atom.[64] Therefore, the 1T' phase is a metastable state between the

less stable 1T phase and the stable 2H phase. Though many recent experimental studies have indicated the distorted 1T MoS_2 structure (1T') to be metallic in nature, many computation studies have calculated a small band gap of 0.1 – 0.2 eV.[64-66]

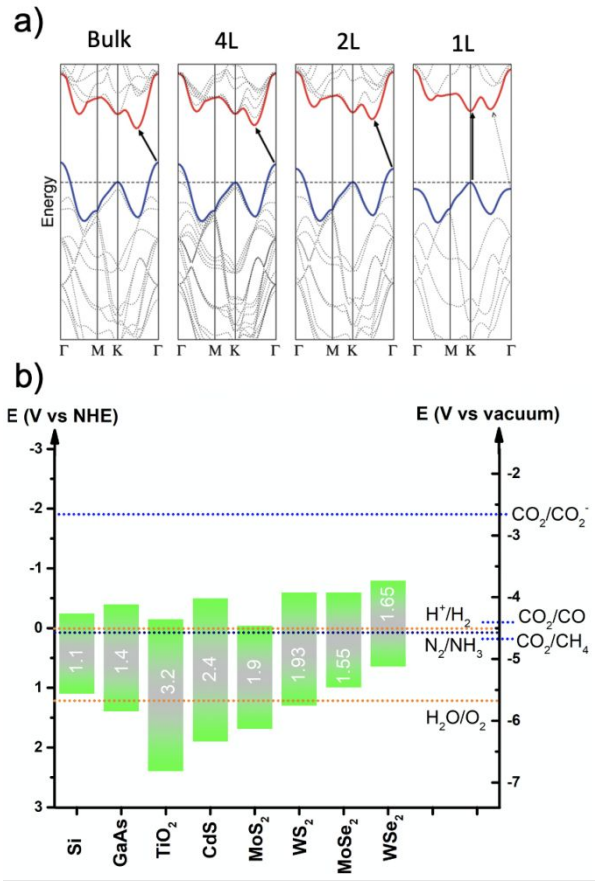

Fig. 2. a) Calculated band diagrams for MoS_2 with the change in the layer numbers, left most being the bulk material then four layers, bilayers and right most is a monolyer. Reprinted with permission.[48] Copyright 2010 American Chemical Society. b) Band gaps of common semiconductors and TMDCs with reduction potentials for nitrogen to ammonia and CO_2 to CO, CH_4, and CO_2^-.

The 2D TMDCs in the 2H phase, particularly Mo and W sulfides and selenides, have been heavily studied and employed in electronic devices as they are highly tunable 2D semiconductors. First-principles calculations and experimentally obtained results have predicted an indirect optical band gaps of 1.2 eV for bulk MoS_2 and 1.4 eV for bulk WS_2 that increases in the monolayers to

direct band gaps of 1.9 eV and 2.0 eV, respectively (Figure 2b).[48] The band structure of MoS_2 from bulk to few layers to monolayer, calculated from first principles calculations, are shown in Fig. 2a.[48]

Relevant to this review article are the band edge positions of 2D TMDCs relative to the reduction potentials for CO_2RR products and NRR to ammonia. Fig. 2b summarizes the reduction potentials for some CO_2RR products, such as CO and CH_4, as well as the NRR product NH_3 at pH = 0, which are higher than 0 V vs. RHE. The conduction band minimum (CBM) of the semiconducting 2D TMDC should have a more reducing potential (*i.e.,* closer to vacuum and more negative on the NHE scale) than the reduction potentials of CO_2RR/NRR product(s) of interest. For these reduction reactions, the counter reaction to complete the circuit would ideally be the oxidation of water to O_2, with a thermodynamic oxidation potential of 1.23 V vs NHE at pH=0. Fig. 2b shows that monolayers of Mo and W dichalcogenides have CBMs with enough reducing potential to reduce protons, CO_2, and N_2 to certain products. While the MoS_2 valence band maximum (VBM) is also positioned for driving water oxidation, the other TMDCs have VBMs with insufficient oxidizing potential for this reaction. As such, they require either band edge engineering or pairing with other semiconductor electrodes to carry out the complete reactions photocatalytically or pairing with an electrode for photoelectrochemical reactions. Tuning the band gap of TMDCs have been extensively discussed by others, and we direct interested readers to these articles for more details.[67-69]

2.2.2 MXenes

The latest additions to the 2D layered materials class are the transition metal carbides, nitrides, and carbonitrides, collectively known as MXenes. Most common MXenes that have been experimentally realized are carbides and more recently nitrides and carbonitrides have also been

synthesized.[70-72] The first MXene to be synthesized was $Ti_3C_2T_x$ in 2011 and since then more than 60 MXenes have been realized.[72, 73] MXenes are also considered to be the 2D version of transition metal carbides and nitrides with face centered cubic rock salt structures. Nevertheless, the MXene exposes (0001) basal plane surface that is analogous to the transition metal carbide (111) surface that has a large surface energy, hence the preparation of MXenes from transition metal carbides is challenging.[74]

The initial MXenes were derived from etching off the A layers of a so-called MAX phase. The MAX phase derives its name from the chemical composition $M_{n+1}AX_n$, where M and X are the same elements in the MXenes and A is usually a Group IIIA or a IVA element (*e.g.,* Al, Si).[72] The MAX phase has a layered structure with hexagonal *P63/mmc* symmetry where the metal occupies a close-packed structure with the X atoms filling octahedral interstitial sites.[75] M-X bonds have a mix of covalent/metallic/ionic nature and the M-A bonds are metallic in nature. Utilizing the differences in the MAX phase bonding strengths of the various bonds, it is possible to selectively etch the A layer.[71] After the etching process, A layers are replaced with surface termination groups: O, OH, and/or F bonded to the terminal transition metals on the surface.[71, 72] Overall, the resulting MXene is a hexagonal-close packed structure. Nevertheless, the ordering of the metal atom changes based on MXene stoichiometry. For example, M_2X has a hexagonal close-packed stacking with ABABAB repeating units, whereas the M_3X_2 and M_4X_3 type MXenes have face-centered cubic stackings with ABCABC ordering.[71] Note that the stacking of MXenes can also vary with other factors such as the number of *d* electrons in the metal M, the identity of X (i.e. a carbide, nitride or carbonitride), and the surface termination group. For example, a DFT study by Gouveia *et al*. that took into account thermodynamic and kinetic data, showed that ABABABAB stacking

is more frequent among nitrides than the corresponding carbides and also is favored by oxygen terminations.[76]

DFT calculations have predicted MXenes with both metallic and semiconducting electronic structures that depend on the composition.[77-79] Shein and coworkers used first principles calculations to probe the chemical structures, electronic properties, and stability of pristine MXenes (without surface termination groups T_x) of $Ti_{n+1}C_n$ and $Ti_{n+1}N_n$ for n = 1, 2, and 3.[79] Relative to the corresponding MAX phases (Fig. 3a), it has been calculated that the density of states (DOS) of the MXenes increases around the Fermi level (Fig. 3b). This observation was justified by the redistribution of the surface Ti 3d states in the Ti-Ti surface bonds after the breaking down of the Ti-Al bonds and the removal of the Al layers in the respective MAX phase.[79] Experimentally, such pristine MXene surfaces are hard to obtain after the etching process of the MAX "A" layers. Recent studies have revealed that certain post-etch treatments can eliminate the surface terminations to a large extent. Person and coworkers employed a post-etch annealing followed by hydrogen treatment at elevated temperatures to successfully reduce F and O terminations in the $Ti_3C_2T_x$ MXene.[80] Thermal treatment at 650 ^oC at 10^{-6} mbar inside an environmental transmission electron microscope (ETEM) resulted in the desorption of F. The resulting MXene rearranges the O to the thermodynamically favorable orientations. Then, treatment of the O-terminated MXene with H_2 gas at 8 mbar and 750 ^oC, pristine surfaces with a Ti:O ratio of 3:0.6 was obtained, a significant decrease from 3:2.1 at room temperature.[80]

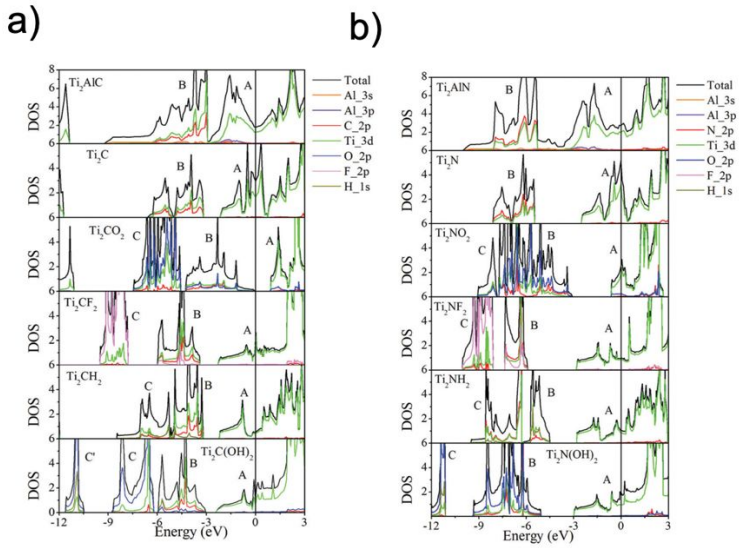

Fig. 3: Partial density of states plots (DOS) for the MAX phase a) Ti_2AlC and b) Ti_2AlN along with the corresponding MXenes with various surface functional groups. Reprinted with permission.[78] Copyright 2013 American Physical Society.

In addition to the dependence on layer composition, surface functional groups impact the metallic or semiconducting nature of MXenes. Xie *et al.* investigated the electronic properties of surface-terminated (O, OH, H, and F) $Ti_{n+1}C_n$ and $Ti_{n+1}N_n$ MXenes.[78] Fig. 3a shows the partial DOS of the Ti_2AlC and the derived MXenes with surface terminations. The DOS near E_f for the MAX phase is dominated by the Ti 3d orbitals (Fig. 3a) and removal of the Al layers from the MAX phase causes the Ti 3d orbitals to redistribute or delocalize giving rise to Ti-Ti metallic bonds. The surface terminations lead to depopulation of states near E_f. Thus, the metallic Ti_2C has a small band gap opening when adding O_2 surface termination groups, with a 0.24 eV band gap calculated with PBE functional and 0.88 eV band gap calculated by HSE06 hybrid functional.[78] All other materials retain their metallic nature but a clear decrease in the DOS near the E_f is observed. A similar result is calculated for Ti_2AlN and the corresponding MXenes (Fig. 3b).

Calculations by Sang *et al.* suggest metallic character for defect-rich monolayer $Ti_3C_2T_x$ MXene with OH terminations. Compared to the pristine $Ti_3C_2T_x$ MXene surface, the authors

observe a decrease in the DOS near E_f for the defect-rich MXene, which was expected to reduce the conductivity.[81] Nevertheless, different Ti vacancy concentrations on OH terminated Ti_3C_2 MXene showed very similar DOS; thus it was predicted to exhibit high conductivity comparable to the pristine surfaces. These theoretical results are supported by recent experimental results by Hart *et al*. They studied the effect of surface termination and intercalants on the electronic properties of $Ti_3C_2T_x$, Ti_3CNT_x, $Ti_3CNT_x(TBA^+)$ and $Mo_2TiC_2T_x$ (delaminated using tetrabutylammonium hydroxide, TBAOH).[82] Vacuum annealing partially eliminated the F, OH, and O surface terminations, and O terminations were more stable than F terminations. The removal of the surface terminations improved the electronic conductivity of all the MXenes that were probed.[82] With regard to the particular CO_2RR and NRR in this review, it is noteworthy that the bare surface of MXenes without any surface function groups are naturally quite reactive and have low energy barriers for, the typically rate-determining, dissociation of CO_2 and N_2.[83] This interesting "surface-determining" activity and selectivity property of MXenes has been explored and will be discussed in the following sections.[84, 85]

2.3 Synthesis

2.3.1 TMDC Synthesis

Two-dimensional TMDCs can be obtained from both top-down (mechanical and chemical exfoliation) and bottom-up approaches (chemical vapor deposition (CVD) and solution-based hydrothermal techniques). Bulk TMDCs are needed for top-down approaches, but these can be hard to obtain naturally. The only known naturally occurring TMDCs are MoS_2 and WS_2 in the form of molybdenite and tungstenite minerals, respectively. Bulk TMDCs are also widely synthesized with chemical vapor transport techniques.[52, 86, 87] Mechanical exfoliation to nanosheets, often using the scotch tape method, can provide high-quality monolayer sheets of TMDCs (Fig.

4a), providing the base for fundamental studies and device fabrications.[87] Nevertheless, this technique has limited scalability and the small flake sizes and poor film uniformity hinders the repeatability and widespread use of the technique. Liquid-phase exfoliation of bulk materials under sonication has been utilized to obtain single to few-layer sheets of TMDCs. This technique relies on the synergy between the solvent or a surfactant to balance the cohesive energy between the sheets.[88-90] Low yields, non-stoichiometric mixtures, and difficulty in controlling the thickness (number of layers) has prevented the widespread use of liquid-phase exfoliation. More recent liquid phase exfoliation methods involve Li intercalation and exfoliation in water, a highly scalable technique that has produced single layers of MoS_2 (Fig. 4b),[51, 91] WS_2,[91] TaS_2, $MoSe_2$,[92] TiS_2[93, 94] and $TiSe_2$.[95] However, exfoliation of some TMDCs such as MoS_2 and WS_2 through Li intercalation causes a phase transformation from the semiconducting 2H to the metallic 1T or 1T' phases,[93] limits the flake size to sub-micron sizes, and generally requires a relatively long processing time.

Recent attempts to grow high quality TMDCs with controlled thickness and wafer scale lateral dimensions have utilized techniques such as chemical vapor deposition (Fig. 4c),[96] metal-organic chemical vapor deposition (MOCVD), atomic layer deposition (ALD, Fig. 4d),[97] molecular beam epitaxy (MBE, Fig. 4e),[98] and solvothermal methods (Fig. 4f). CVD is a practical bottom-up technique where precursors react and/or decompose at elevated temperatures onto a substrate, producing mono- or few-layer TMDCs with high crystal quality, scalable size, tunable thickness, and tunable electronic properties (Fig. 4c). MOCVD, a technique that uses gas- or solid-phase metal-organic precursors in a CVD setup, [99-101] has been used to synthesize high-quality wafer scale MoS_2 and WS_2[100] and other chalcogenides of Mo and W (*e.g.,* mono/few layer WSe_2).[75]

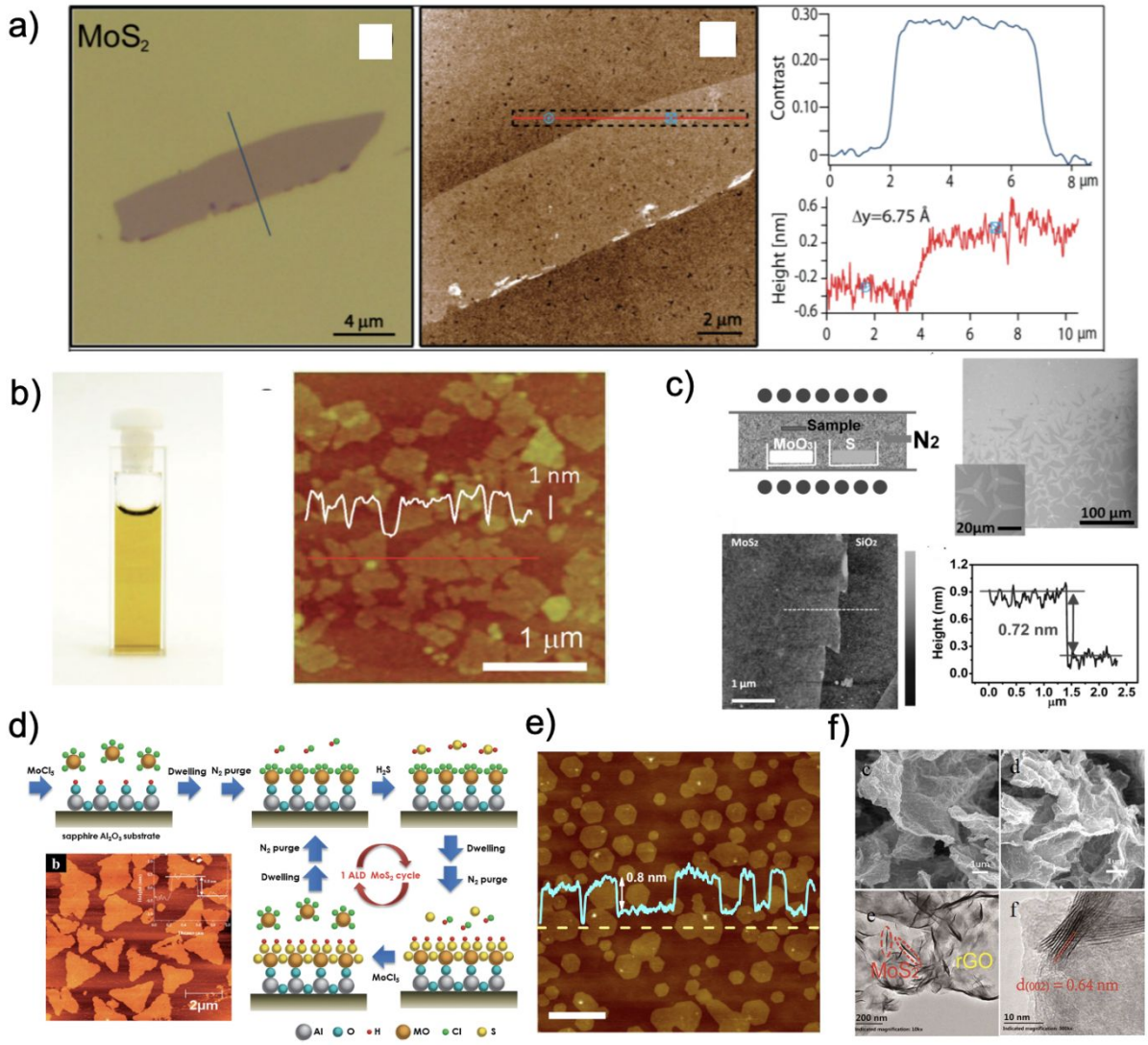

Figure 4: a) Mechanically exfoliated MoS_2 on a SiO_2 substrate. From left to right, optical image of a monolayer MoS_2 nanosheet, AC mode AFM image and the right most plots are the corresponding contrast and the height profiles. Reprinted with permission.[87] Copyright 2011 IOP Publishing Ltd. B) Left: colloidal suspension of chemically exfoliated MoS_2 using an organo-lithium salt. Right: AFM image of flakes from this dispersion, with height profile (white trace) taken along the red trace. Reprinted with permission.[51] Copyright 2011 American Chemical Society**.** C) CVD technique involving the precursors MoO_3 reduced by the chalcogen source (S) heated in a N_2 environment to obtain high quality films (MoS_2), AFM image of a MoS_2 film obtained by this CVD technique with the height profile showing a monolayer thickness. Reprinted with permission.[96] Copyright 2012 John Wiley and Sons. D) Schematic of ALD deposition of MoS_2 film with the inset showing an AFM image with triangular monolayers. Reprinted with permission.[97] Copyright 2014 The Royal Society of Chemistry**.** E) AFM image of a MoS_2 film obtained from molecular beam epitaxy (MBE). Reprinted with permission.[98] Copyright 2017 American Chemical Society. F) SEM and TEM images of MoS_2 on reduced graphene oxide support obtained *via* a hydrothermal reaction. Reprinted with permission.[102] Copyright 2017 Nature Publishing Group.

Hydrothermal synthesis of TMDCs is a versatile technique for obtaining 2D and 3D structures with large surface area for applications in energy conversion and storage applications.[103] While this technique benefits from lower temperatures and better scalability, relative to CVD, ALD or MBE, precise control over structure and layer number is challenging. Synthesis of MoS_2 in both 2H and 1T phase has been realized with this technique.[63, 65, 104-106] Vertically aligned or edge-oriented TMDCs with maximized edges obtained *via* a hydrothermal route have been studied extensively on a large number of substrates such as carbon cloth, [105, 107, 108] carbon nanotubes,[109, 110] graphene/graphene oxide (Fig. 4f),[111] reduced graphene oxide,[102, 112-114] amorphous carbon[115] and MXenes.[116-121] The versatile nature of the technique also allows easy incorporation or doping of TMDCs by mixing respective dopants in the reaction mixture during the synthesis.[65, 105, 122, 123]

2.3.2 MXene Synthesis

MXenes are typically derived by etching atomic layers from their corresponding precursors, which are usually MAX phases. There are over 60 MAX phases reported so far, and the number is much higher when solid solutions and ordered double transition metal structures are considered.[71, 72] Selective etching of the metallic M-A bond within MAX structures stems from the higher M-A bond reactivity compared to the more labile M-X bond.[72, 124] Unlike vdW bonded graphene and TMDC sheets, the relatively strong inter-layer bonds in MAX structures preclude the use of shear mechanical strain to exfoliate the corresponding MXenes.[70, 71] Non-MAX phase precursors have also been used to obtain MXenes. Mo_2CT_x MXene was the first of its kind to be synthesized from a non-MAX phase precursor Mo_2Ga_2C (Fig. 5a).[125-127] Unlike the MAX phases, this compound has two A-elemental (Ga) layers separating the M-X layers.[125, 126] Other examples of non-MAX phase derived MXenes include $Zr_3C_2T_x$[128] and U_2CT_x,[129] obtained by etching of Al_3C_3 layers from $Zr_3Al_3C_5$ and $U_2Al_3C_4$ precursors, respectively.[128, 129]

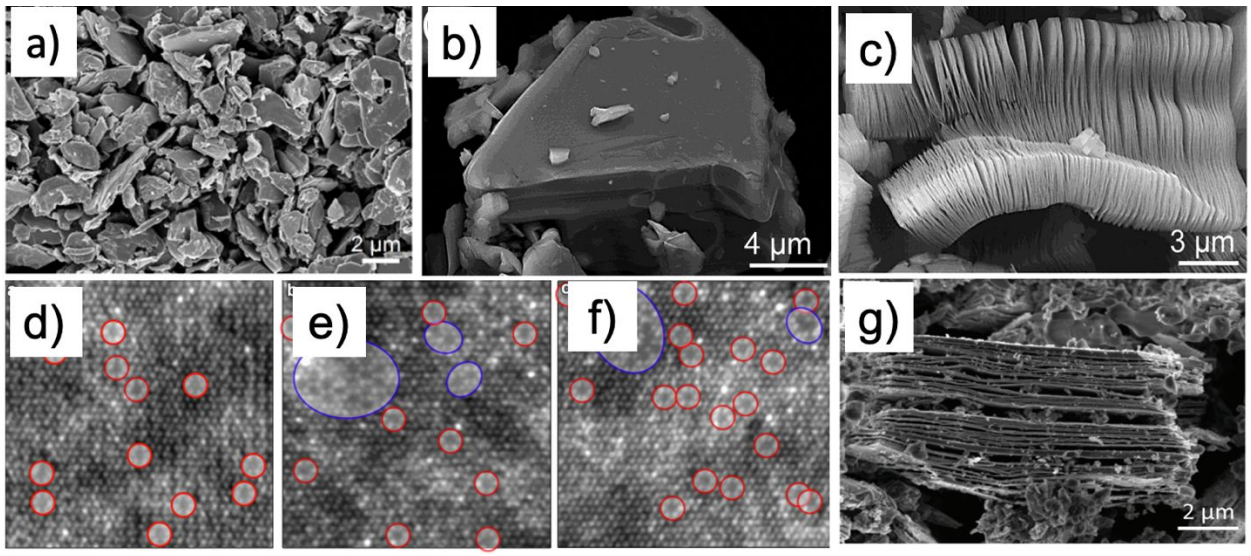

Figure 5. SEM micrographs of a) Mo_2C MXene obtained from a non-MAX phase precursor, Mo_2GaC. Reprinted with permission.[127] Copyright 2016 American Chemical Society. B) SEM micrographs of Ti_3AlC_2 MAX phase before etching to produce c) $Ti_3C_2T_x$ MXene. Reprinted with permission.[130] Copyright 2012 American Chemical Society. (d-f) HAADF-STEM images of $Ti_3C_2T_x$ MXene synthesized using varying HF concentrations 2.7 wt%, 5.3 wt%, and 7 wt%, respectively. The smaller red circles are single Ti atom vacancies and larger blue circles indicate clusters of Ti vacancies. Reprinted with permission.[81] Copyright 2016 American Chemical Society. G) SEM micrograph of the few layer $Ti_4N_3T_x$ MXene obtained from etching the Al layer in Ti_4AlN_3 MAX phase using a molten salt approach. Reprinted with permission.[77] Copyright 2016 The Royal Society of Chemistry.

Selective etching of MAX or non-MAX phases is carried out in an aqueous fluoride-containing acidic solution for both metal carbides and nitrides.[72] The HF etchant is either added directly or can be generated *in-situ* by using mixtures of HCl and fluoride-containing salts (lithium fluoride, ammonium fluoride, or ammonium hydrogen bifluoride).[72] $Ti_3C_2T_x$ was the first MXene to be synthesized by selective HF etching of the Al layer from the Ti_3AlC_2 MAX phase (Fig. 5b and c).[44, 130] A series of other MXene structures followed $Ti_3C_2T_x$ that were derived from various MAX phases (Ti_2AlC, Ta_4AlC_3, $(Ti_{0.5},Nb_{0.5})_2AlC$, $(V_{0.5},Cr_{0.5})_3AlC_2$, and Ti_3AlCN).[130] The surface termination, defect concentration, and crystalline quality of 2D MXene sheets rely heavily on both the etching and delamination conditions. For instance, Sang *et al.* studied the surface defects of monolayer $Ti_3C_2T_x$ MXene using mild conditions (HCl and LiF instead of HF) for etching the

Ti_3AlC_2 MAX phase.[81] Single titanium atoms or clusters of Ti atom vacancies were observed on the MXene sheets (Fig. 5d, e and f), depending on the HF concentration in the etching process.[81]

Nitride MXenes took a longer time than the carbide MXenes to be realized,[71] likely because of two factors. First, calculations show that the cohesive forces in $Ti_{n+1}N_n$ MXenes are lower than in $Ti_{n+1}C_n$ MXenes, whereas the formation energy (ΔE_f) of $Ti_{n+1}AlN_n$ is higher than that of $Ti_{n+1}AlC_n$.[79] Therefore, the Al in the nitride MAX phase has stronger bonding than those in carbide counterparts, making extraction harder.[70, 79] Second, nitride MXenes dissolve in strong HF acid solutions, due to their lower stability. Urbankowski *et al.* reported the first nitride MXene ($Ti_4N_3T_x$, Fig. 5g) in 2016 using a molten salt approach to etch the Al layer in the Ti_4AlN_3 MAX phase.[77] When a broader series of 486 MAX phases of M_nAN_{n-1} was considered by Dolz *et al.*, the DFT results indicated that most nitride MAX phases had a lower exfoliation energy relative to their carbide counterparts.[131] These results were in agreement with the previous calculations of Shein and coworkers, that saw a larger exfoliation energy for N-based MAX phases containing Al as the 'A' layer.[79, 131]

3. CO_2 Reduction Reactions

The growing concerns of anthropogenic fossil fuel consumption, greenhouse gas emissions, and associated climate change have motivated various CO_2RR approaches to convert CO_2 into useful C-based materials, such as C-based fuels and plastics.[132] Along with the modification of processes to reduce the CO_2 emissions, the CO_2RR could result in the highly desirable goal of "zero-carbon emission". For catalytic CO_2 conversion to become a reality, suitable catalysts are required to activate the CO_2 molecule and transform it into a wide range of chemical compounds. CO_2 activation is challenging due to the low solubility and chemical inertness of CO_2 that can lead to HER dominating over CO_2RR. Sufficient adsorption

(physisorption and/or chemisorption) of CO_2 on a catalyst surface is therefore a prerequisite for efficient dissociation/weakening of the C=O bond and further transduction of electrons to form complex C-C bonds for energy-rich molecules with high-specificity.[133, 134] Conventional homogeneous and heterogeneous catalysts (*e.g.*, metal–organic complexes, Cu, Ag, and Au) for CO_2RR have various disadvantages, such as poor chemical durability, high-cost, or photo-inactivity.[135] As such, 2D TMDCs and MXenes featuring tunable surfaces are gaining interest in the CO_2RR community.

3.1 CO_2RR Mechanism

Electrochemical CO_2RR using 2D TMDC and MXene catalysts relies on good electrical conductivity and CO_2 adsorption properties of the materials, where the sole energy driving the reaction is electricity. In contrast, photoelectrochemical and photochemical CO_2RR utilize photoexcited electrons to drive the reaction and, therefore, require the 2D TMDCs and MXenes to be semiconductors or coupled to semiconductors. For successful photo-driven CO_2RR, the energy of the conduction band minimum (CBM) needs to provide a thermodynamic driving force for the desired CO_2 reduction half-reaction. (Scheme 2c). Semiconducting MoS_2[136] and WSe_2[137] have been extensively studied for photo-driven CO_2 reactions. In contrast, MXenes are usually combined with other photoactive materials for CO_2 photoreduction since most MXenes are not photoactive (Section 2).[121] Nevertheless, the discussion of the CO_2RR mechanism by using 2D TMDC and MXene catalysts mainly relies on charge transfer, CO_2 activation, and intermediate formation for both (photo)electrochemical and photochemical catalysts.

Table 1. Summary of the possible CO_2RR pathways by 2D TMDC and MXene catalysts as well as the corresponding standard redox potential.

CO_2RR pathways	**Standard Redox Potential (E^0 vs. RHE, pH=7)**

C1	$CO_2 + 2H^+ + 2e^- \rightarrow CO + H_2O$	-0.116
	$CO_2 + 2H^+ + 2e^- \rightarrow HCOOH$	-0.196
	$CO_2 + 4H^+ + 4e^- \rightarrow HCHO + H_2O$	-0.066
	$CO_2 + 6H^+ + 6e^- \rightarrow CH_3OH + H_2O$	0.034
	$CO_2 + 8H^+ + 8e^- \rightarrow CH_4 + 2H_2O$	0.174
C2	$2CO_2 + 10H^+ + 10e^- \rightarrow C_2H_6O_2 + 2H_2O$	0.014
	$2CO_2 + 12H^+ + 12e^- \rightarrow C_2H_4 + 4H_2O$	0.065
	$2CO_2 + 14H^+ + 14e^- \rightarrow C_2H_6 + 4H_2O$	0.144
C3	$3CO_2 + 18H^+ + 18e^- \rightarrow C_3H_8O + 5H_2O$	0.103
	$3CO_2 + 20H^+ + 20e^- \rightarrow C_3H_8 + 6H_2O$	0.277
C4	$4CO_2 + 24H^+ + 24e^- \rightarrow C_4H_{10}O + 7H_2O$	0.110

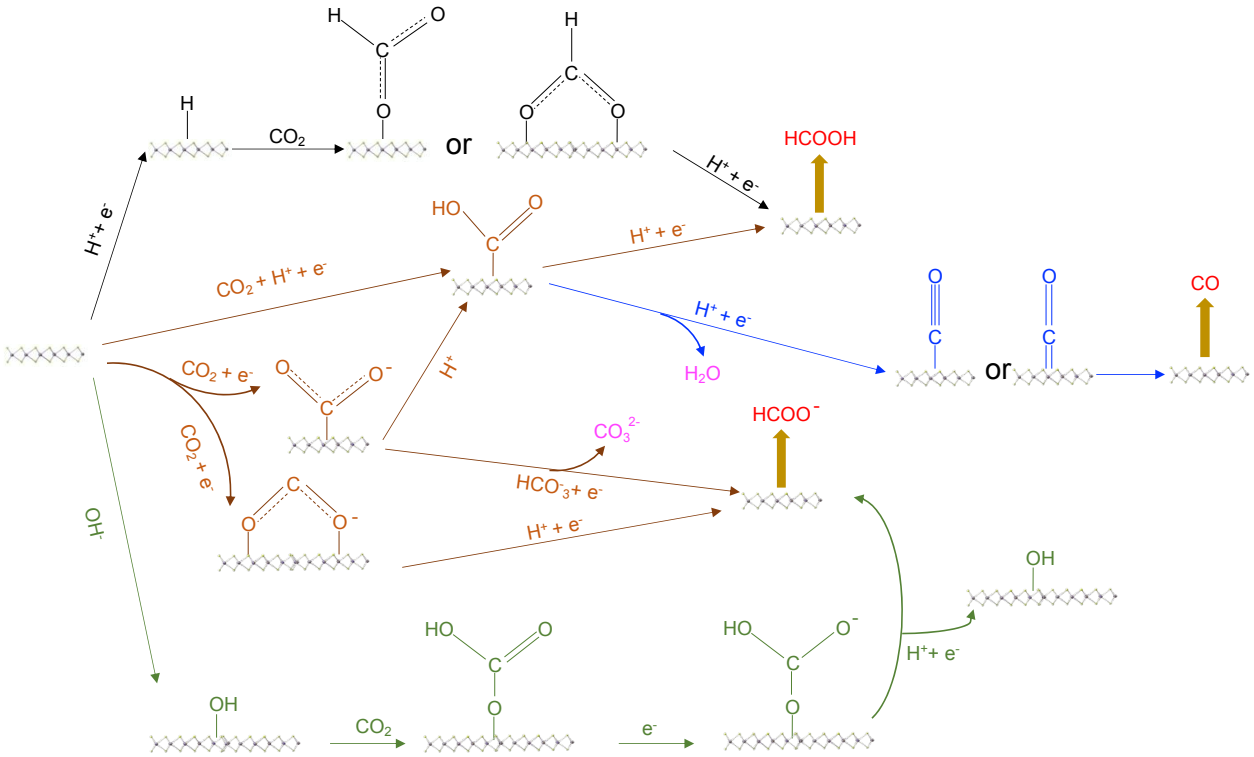

Fig. 6. Possible reaction pathways for CO_2 reduction to HCOOH or $HCOO^-$, including: a monodentate or bidentate intermediate route (black); a CO_2* radical intermediate route (orange); and a surface-bound carbonate intermediate route (green). In addition, the reaction pathways for CO_2 to CO are shown (blue). Red color highlights the CO_2 reduction products. Purple color marks the byproducts. Redeveloped based on the information from reference.[133]

To form C-based products from CO_2, the CO_2 must be first activated on the appropriate surface and then undergo proton-coupled electron transfer (PCET) reactions to generate various products. Importantly, MXenes are predicted to adsorb and activate CO_2 molecules quite strongly.[138] Depending on the number of electrons/protons transferred and surface groups available, different catalytic reactions can occur to generate intermediates and consequently different carbon products, such as C1 compounds and C2+ hydrocarbons.[133, 139-141] Thus, controlling the product distribution from CO_2RR is a critical consideration for any catalyst. The conventional CO_2RR products from 2D TMDCs and MXenes are usually C1 products, including carbon monoxide (CO), formic acid (HCOOH), methane (CH_4), methanol (CH_3OH), and formaldehyde (HCHO). Trace amounts of C2+ products can also be obtained (*e.g.*, ethylene (C_2H_4), ethane (C_2H_6), ethylene glycol($C_2H_6O_2$), propane (C_3H_8), propanol (C_3H_8O), and t-butanol ($C_4H_{10}O$)). The thermodynamic potentials of these selective CO_2RR pathways are summarized in Table 1**,** and the detailed mechanisms are discussed below.

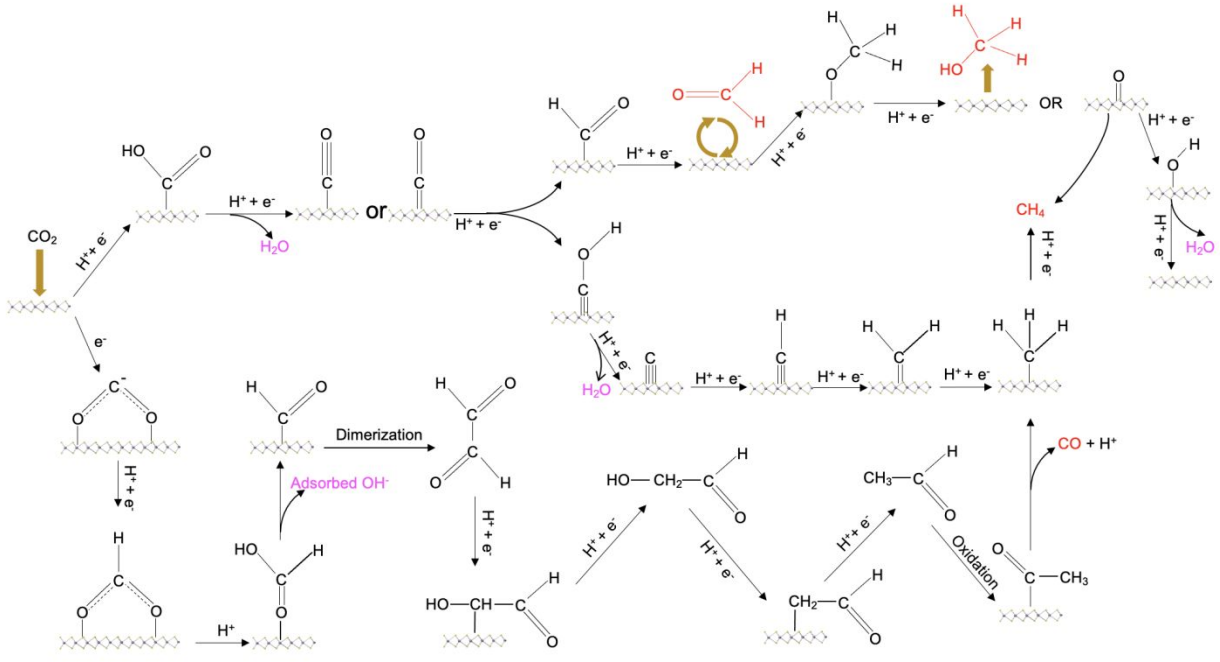

Fig. 7. Possible reaction pathways for CO_2 reduction to HCHO, CH_3OH, and CH_4. Red color marks the CO_2 reduction products. Purple color highlights the byproducts. Redeveloped based on the discussion from references.[133, 134, 142]

In general, the simplest CO_2RR involves two PCET steps, and the final products are mainly CO and HCOOH. As shown in Fig. 6, the first PCET happens when CO_2 is coupled to a metal–hydrogen bound surface or H^+ from solution, resulting in formate (*OHCO) or carboxyl (*COOH) intermediates. Further PCET reduces these species to form HCOOH and CO.[133] In addition to HCOOH and CO, three other C1 molecules can be produced from CO_2RR, including HCHO, CH_3OH, and CH_4, which are believed to be produced by the step-by-step hydrogenation of the surface intermediates (*CO, *CHO, *CH_2O, and *CH_3O)[134] or glyoxal converted from *CO_2–[142] (Fig. 7).

Higher order C products can be formed from surface intermediates. Surface CO can react to produce *CHO and *COCHO intermediates and these intermediates can then selectively generate C2 compounds — C_2H_4, C_2H_6, and $C_2H_6O_2$ — following the ethylene and ethanol pathway.[143] Alternatively, the association of CO with hydrogenation induces the *COCHOH intermediate on the catalyst surface and produces C_2H_4 (Fig. 8). Although the mechanistic pathways of C3+ chemicals have been proposed on the coupling of C1 and C2 surface intermediates with PCET, such products are typically only produced in very low yields. So far, 1-propanol, propane, and t-butanol are the only reported C3+ products from CO_2RR using 2D TMDC catalysts[144].

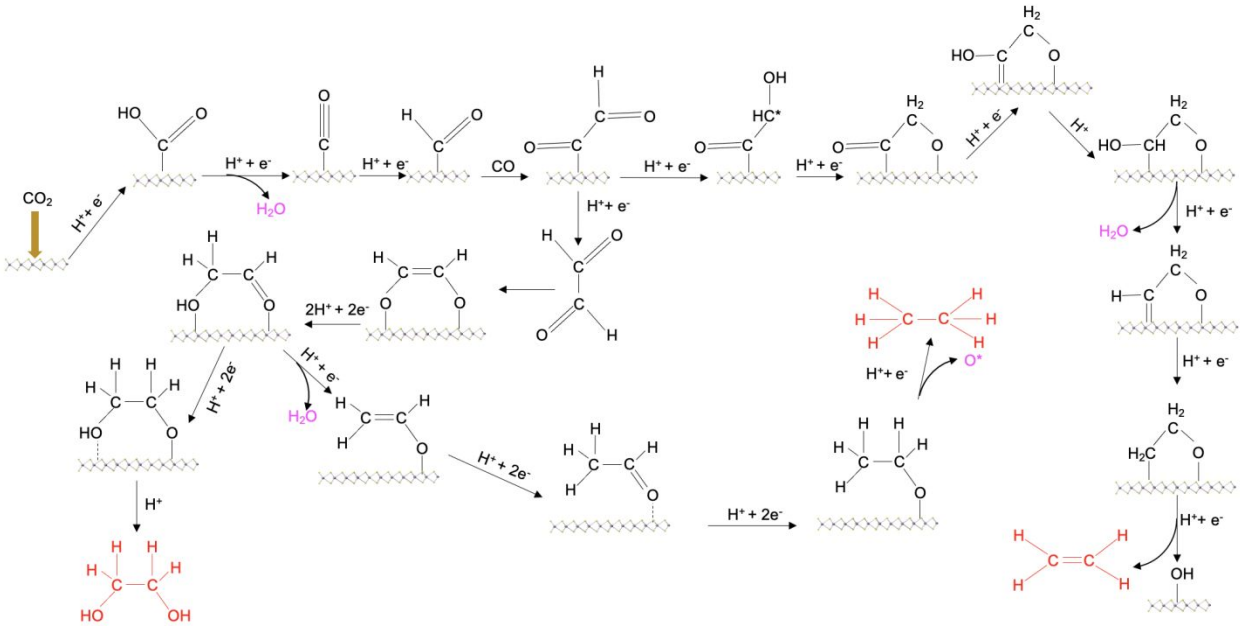

Fig. 8. Possible reaction pathways for CO_2 reduction to form C2 products: C_2H_4, C_2H_6, and $C_2H_6O_2$. Redeveloped based on the discussion from references.[133, 145]

The maximum efficiency and selectivity of a catalytic surface occurs when the adsorbate−surface interaction strength is optimal as per the Sabatier principle: strong enough to drive the reactions forward but weak enough to permit product desorption.[26] Therefore, stabilizing a reacted intermediate (more negative binding energy) but weakening the corresponding sequential intermediate in a certain CO_2RR is crucial for a high performance CO_2RR catalyst. For example, calculations by Chan *et al.* [146] found a linear scaling relationship between the reacted and sequential produced intermediates in the selective CO_2RR for CO production when evaluating different transition metals, where the binding strength linearly increased or decreased for *COOH and *CHO compared to produced intermediate *CO, which prevented tuning the reaction pathway by changing the transition metal. However, they found that the linear scaling relationship could be overcome when evaluating MoS_2 and $MoSe_2$ edge sites, where the *COOH and *CHO binding strength were constant but *CO binding strength could be reduced, which would propel the CO_2RR reaction forward (Fig. 9).[147-150]

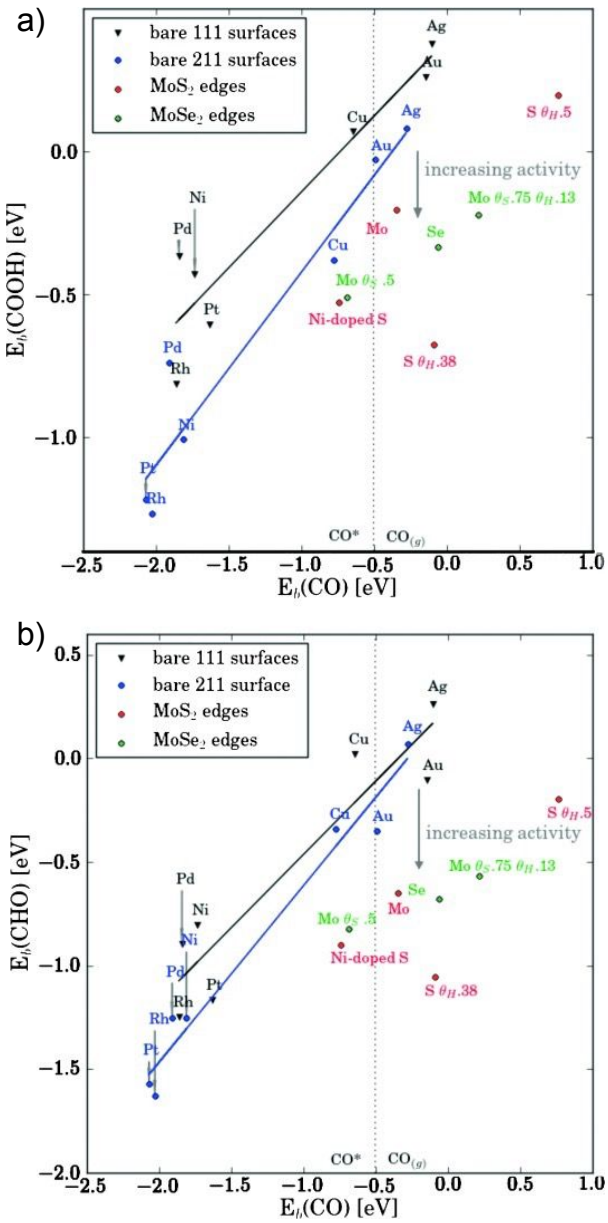

Fig. 9. Breaking of the linear scaling relations between a) *COOH and b) *CHO with *CO on MoS_2 or $MoSe_2$ edges. The vertical dotted lines indicate the E_b(CO) at which an isolated *CO is in equilibrium with 0.01 bar gaseous CO. The catalysts to the right of this line bind CO weakly and are expected to be selective for CO production. The catalysts to the left should further reduce adsorbed CO to hydrocarbons and/or alcohols. Θ was defined as the edge site coverage by different atoms (H, S, Se) and doping of edge sites was also evaluated. Reprinted with permission.[150] Copyright 2014 John Wiley and Sons.

The CO_2RR mechanism using 2D MXene catalysts follow the aforementioned pathways for possible products. MXenes are attractive as catalysts because of (1) sufficient surface metal atoms with empty d-orbitals for gas-phase molecule activation and (2) efficient electron transport, arising from the metallic electronic structure. Several theoretical simulations have been conducted

for CO_2RR using MXenes.[151, 152] Cr_3C_2 and Mo_3C_2 are predicted to selectively reduce CO_2 to CH_4 due to the three-coordinated terminal metals, which are active due to the empty d-like orbitals.[153] As an example, the surface termination -O or -OH groups on Mo_3C_2 reduced the CO_2 energy barrier significantly during the reduction process to CH_4.[153] However, the reaction pathway was influenced by the surface termination group (Fig. 10a and 10b). Additionally, selective processes for CO_2 to CH_4 have also been found to occur over hydroxyl (−OH)-terminated $Sc_2C(OH)_2$. Simulations showed the interaction and change of the intermediates on the MXene surface by exploring the migration of electrons on the carbon atoms of the different intermediates. The charge difference for the *(H)COOH → *CO potential-determining step have the smallest values on $Sc_2C(OH)_2$ and $Yc_2C(OH)_2$ among all studied $M_2C(OH)_2$ and $M_2N(OH)_2$ MXenes (M= Sc, Y, Ti, Ta, Nb, Zr, Hf), indicating less charge transfer during this elementary step with less free energy change, which ensured the exceptional CO_2RR performance (Fig. 10c shows the $Sc_2C(OH)_2$ catalyst).[152]

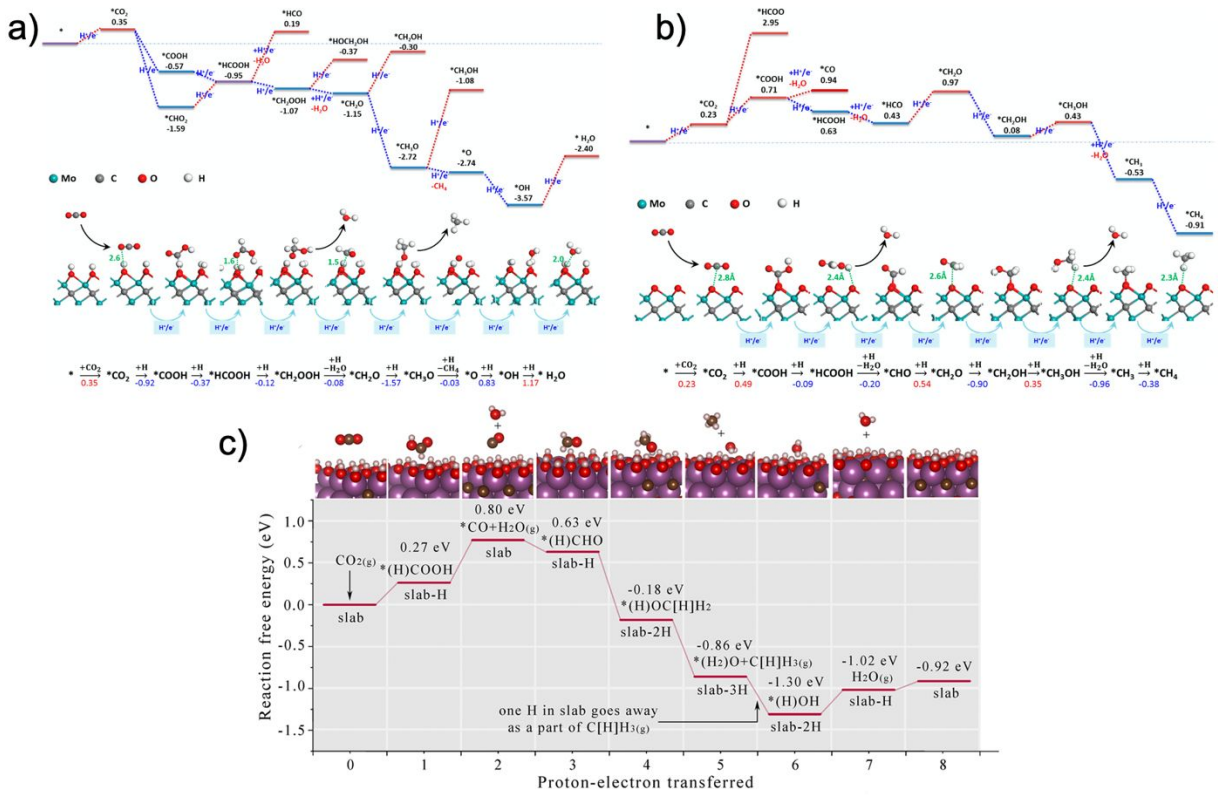

Fig. 10. Minimum energy path for the CO_2 conversion into CH_4 and H_2O catalyzed by a) $Mo_3C_2(OH)_2$ and b) $Mo_3C_2O_2$. Gibbs free energies (vs. SHE in eV) along the pathway (top). Corresponding surface chemical structures (middle) and formula distances (bottom) are shown. Blue and red texts represent spontaneous and nonspontaneous reactions (in eV), respectively. Reprinted with permission.[153] Copyright 2017 American Chemical Society. c) Calculated free energy diagrams for the lowest energy pathways to CH_4 using $Sc_2C(OH)_2$ catalyst. Reprinted with permission.[152] Copyright 2019 American Chemical Society.

3.2 2D TMDC

3.2.1 Electrochemical and Photoelectrochemical CO_2RR

Both theoretical and experimental studies have successfully demonstrated the activity for electrochemical CO_2 reduction *via* TMDC catalysts in aqueous electrolytes under cathodic polarization.[135, 154] TMDCs typically exhibit remarkably different scaling relationships of adsorption energies for key reaction intermediates on their edges versus the basal plane,[155] so that manipulating the ratio of basal sites to edge sites can manipulate the scaling relationship for CO_2 reduction.[156] Owing to the metallic character, a high *d*-electron density, and relatively low work function of ~3–4 eV, metal-terminated edges of TMDCs generally contribute to higher catalytic

activity, but this higher activity is not always directed towards the products of choice. For example, Francis *et al.* demonstrated electrochemical reduction of CO_2 to 1-propanol at single-crystal terraces (low edge density) of bulk MoS_2, while thin films (high edge density) produced more H_2 and less 1-propanol.[144] This study suggests that complex reactions (*e.g.,* CO_2 to 1-propanol is $18e^-/18H^+$) may actually proceed more efficiently on TMDC basal planes, albeit at lower overall rates.

Reducing MoS_2 thickness reduces the work function[157] and increases the available surface area, relative to bulk MoS_2, resulting in faster electron transfer and intermediate adsorption (*e.g.*, $COOH^*$, CO*) as well as higher overall CO_2RR catalytic activity. Lv *et al.* exfoliated bulk MoS_2 powders dispersed in N-vinyl pyrrolidone (NVP) by high-energy ball milling to generate 2D few-layer MoS_2 nanosheets.[158] This exfoliated catalyst could electrochemically reduce CO_2 to CO with a Faradaic efficiency (FE) of 41.2% at −0.9 V vs. RHE, which is 2-fold higher (FE = 19.8%) than bulk MoS_2 (Fig. 11a). Similar improvements for electrochemical CO_2RR were also demonstrated by Asadi and co-workers by reducing the TMDC catalyst dimensions. In their studies, 10% FE of the CO formation was achieved with CVD-grown 2D MoS_2 nanoflakes while 3% FE was reached for bulk MoS_2 at −0.164 V vs. RHE.[155, 159]

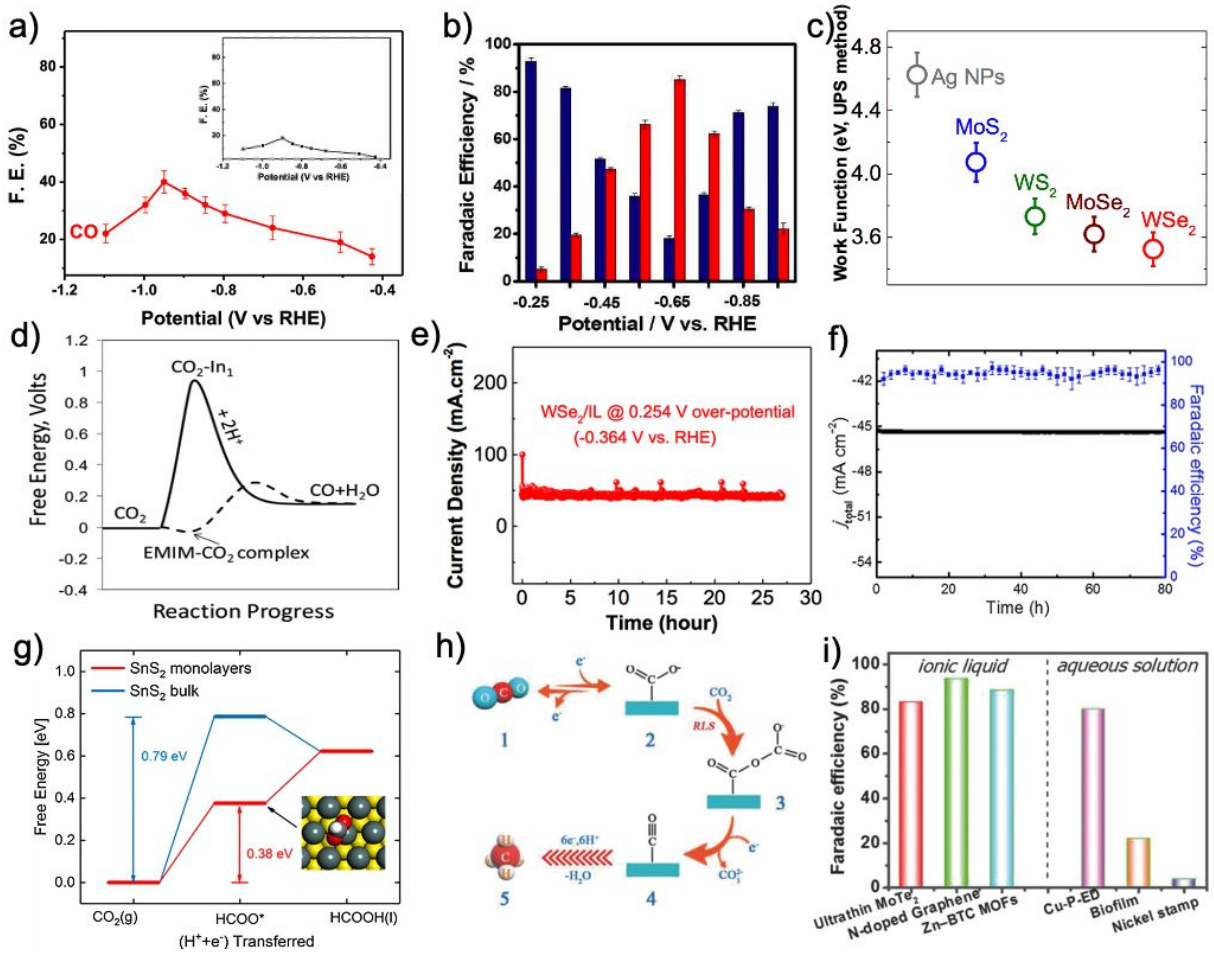

Fig. 11. a) CO Faradaic efficiency (FE) at different applied potentials for exfoliated-MoS_2 catalysts. Inset is the CO FE at different applied potentials for bulk MoS_2. Reprinted with permission.[158] Copyright 2018 John Wiley and Sons. b) Faradaic efficiency for CO (red bars) and H_2 (blue bars) as a function of potential when using amorphous MoS_2 2D flakes. Error bar associated with each value is also provided. Reprinted with permission.[159] Copyright 2016 The Royal Society of Chemistry. c) Experimental work function measurement for Ag nanoparticles (Ag nanoparticles-NPs) and TMDC nanoflakes. Reprinted with permission.[159] Copyright 2016 American Association for the Advancement of Science (AAAS). d) Scheme shows the free energy of the system decreased for the reaction $CO_2 + 2H^+ + 2\ e^- \rightarrow CO + H_2O$ over platinum catalyst surface in EMIM-BF_4 (dashed line) compared to that in water (solid line). The label CO_2–In_1 refers to the intermediate that forms when the first electron is transferred during the reaction. Reprinted with permission.[160] Copyright 2012 American Chemical Society. e) Stability test of WSe_2 nanoflakes in 50 vol% ionic liquid (IL) at potential of -0.364 V vs. RHE (254 mV overpotential). The chronoamperometry (CA) experiment indicate 10% decay after 27 h. Reprinted with permission.[159] Copyright 2016 American Association for the Advancement of Science (AAAS). f) Chronoamperometry results at a potential of −0.8 V vs. RHE and the corresponding FE of formate when using monolayer 2D SnS_2 nanosheets over 80 h. g) Atomic models of DFT-relaxed SnS_2 monolayer and the calculated free-energy profiles for CO_2 reduction to HCOOH on the SnS_2 monolayer and bulk counterpart surface at 0 V vs. RHE, in which the insets are the most stable configurations of the intermediates adsorbed on the surface. Reprinted with permission.[161] Copyright 2018 Elsevier Inc. h) Electroreduction scheme of CO_2 into methane on the ultrathin $MoTe_2$ layers. i) CH_4 FEs for ultrathin $MoTe_2$ in ionic liquid compared to other electrocatalysts. Reprinted with permission.[161] Copyright 2018 John Wiley and Sons.

Amorphous MoS_2 2D flakes have also been explored for CO_2RR catalysis. These materials have the advantage of being prepared by scalable techniques (*e.g.,* electrodeposition) at room

temperature and atmospheric pressure as well as containing a large amount of catalytically active edges. Li *et al.* introduced amorphous MoS_2 on a polyethylenimine modified reduced graphene oxide substrate as an effective CO_2RR catalyst.[154] The authors observed CO production when the overpotential reached 140 mV, and a overpotential of 290 mV catalyzed CO_2 reduction to syngas, a promising feedstock for producing ethanol and methanol through Fischer-Tropsch or microbial synthesis process.[162, 163] Further incremental increases of the overpotential to 540 mV resulted in more CO formation with 85.1% FE (Fig. 11b). The synergistic effect of polyethylenimine and MoS_2 was believed to facilitate selective CO_2 reduction, where polyethylenimine adsorbs CO_2 and intermediate molecules and MoS_2 selectively binds the intermediates for CO_2 reduction. Nevertheless, the CO_2RR performance was still limited by the intrinsic catalytic activity of MoS_2 and the inherent competition between CO_2RR and HER.

Other 2D TMDC catalysts beyond MoS_2 have begun receiving attention for electrocatalytic CO_2RR. Asadi *et al.* evaluated the CO_2RR performance of a series of nanoflakes of MoS_2, $MoSe_2$, WS_2, and WSe_2.[159] $MoSe_2$, WS_2, and WSe_2 all exhibited CO_2 reduction performance much higher than the MoS_2 nanoflakes and conventional Ag nanoparticle catalysts. CO_2 conversion efficiency to CO was anti-correlated with the TMDC work function (Fig. 11c),[159] where the most active catalyst was identified as low-work function WSe_2 nanoflakes terminated with W atoms. In the same study, the ionic liquid 1-ethyl-3-methylimidazolium tetrafluoroborate (EMIM-BF_4) was introduced in the electrolyte to form the $[EMIM–CO_2]^+$ complex. The authors proposed that the $[EMIM–CO_2]^+$ complex helps the selective reduction of CO_2 but suppressed the HER.[155, 159] As shown in Fig. 11d,[160] the $[EMIM–CO_2]^+$ complex can thermodynamically reduce the reaction barrier for electrons passing into CO_2 over the catalyst surface, such as silver, platinum, and TMDCs, inducing the high CO production. Consequently, WSe_2 nanoflakes showed exceptional

current density of 19 mA cm^{-2} and FE_{CO} of 24% at a low overpotential (54 mV), with a CO production turn over frequency (TOF) of 0.28 s^{-1} at −0.164 V vs. RHE. Good catalytic stability, exceeding 27 h, was attributed to the stable W-terminated edges (Fig. 11e).[154]

Additional studies have focused on tin disulfide (SnS_2) and molybdenum telluride ($MoTe_2$). While Sn is not a transition metal, SnS_2 shares the MX_2 composition and layered crystal structure with the well-known TMDCs. SnS_2 has emerged as a highly promising 2D semiconductor, with performance comparable to MoS_2 in a number of applications, including CO_2RR catalysis.[164] Thus, we include some advances of 2D SnS_2 in this section. Monolayer 2D SnS_2 nanosheets—obtained by Li-intercalation/exfoliation of bulk SnS_2[161] performed as a robust catalyst, achieved high FE of 94 ± 5% at -0.8 V vs. RHE, and had excellent long-term durability (over 80 h) for CO_2 electroreduction to formate in 0.1 M $KHCO_3$ (Fig. 11f). DFT results suggested this high activity results from the potential-determining-step of HCOO* intermediate formation on (001) SnS_2 surface (Fig. 11g)**.** For $MoTe_2$ catalysts in 0.1 M $KHCO_3$, adsorbed CO_2 molecules preferred to be reduced as $CO_2{}^{*-}$ intermediates and coupled with another CO_2 molecule to form the CO_2-$CO_2{}^{*-}$ adduct. This adduct then ultimately converted to CH_4 through PCET reactions (Fig. 11h). The FE of methane production from CO_2 was ~83% at -1.0 V vs. RHE, a 137% improvement over bulk $MoTe_2$ and similar to the best CO_2RR catalysts reported thus far (Fig. 11i). The activity retention lasted for more than 45 h.[161]

Energy state engineering and band structure tailoring of TMDCs have emerged as promising strategies for stimulating selective CO_2RR by facilitating CO_2 activation and product desorption. Mo-terminated edges of bulk MoS_2 have shown efficient CO_2RR to CO with low overpotential, where the available electrons for a given reaction can be also roughly described by the DOS at the Fermi level.[1, 155] Therefore, modulating the edges of 2D TMDCs could affect the

adsorption strength of intermediates with edge atoms. As such, recent studies have explored the effect of transition metal doping on MoS_2 edge electronic structure and CO_2RR. DFT calculations on Nb-doped MoS_2 have revealed low concentrations of Nb near the Mo edge atoms enhance TOF of CO formation by modifying the binding energies of intermediates to MoS_2 edge atoms.[154] Experimentally, doping of 5% Nb in vertically aligned MoS_2 enabled a small overpotential of 31 mV and a CO TOF of one order of magnitude higher than pristine MoS_2 and two orders of magnitude higher than Ag nanoparticles (Fig. 12a).

Metal sites at transition-metal terminated edges are believed to be the active sites for CO_2RR from previous studies on pure TMDCs.[155, 165] Theoretical studies by Mao *et al.*[166] found that the overall higher *d*-band center energy, relative to E_f, induced stronger CO adsorption at MoS_2 edges. This scaling relationship between the *d*-band center position and the binding energy of CO could help screen transition metal dopants. Doping V, Zr, and Hf to the active Mo site could lead to the shift of the d-band center and accordingly decreased the CO binding energy, significantly promoting CO desorption from the MoS_2 edge (Fig. 12b). Interestingly, dopant concentration did not influence catalytic activity (Fig. 12c). However, no experimental investigations confirm these results yet. In contrast, CO_2RR activity was predicted to depend on Ni dopant concentration in monolayer SnS_2 (Fig. 12d), with the FE for CO and formate increasing with Ni content up to 5%.[167] Experimentally, higher Ni doping levels induced inhomogeneous incorporation into SnS_2 nanosheets, creating NiS that promoted the HER over CO_2RR. For example, the 5% Ni-SnS_2 nanosheets exhibited the highest $FE_{CO+formate}$ of 93% at −0.9 V vs. RHE compared to 71% $FE_{CO+formate}$ for 7% Ni-SnS_2 nanosheets. CO and formate production rates for 5% Ni-SnS_2 nanosheets were 81 mmol h^{-1} g^{-1} and 587.5 mmol h^{-1} g^{-1}, respectively. The low work

function (Fig. 12e) and intraband defect states introduced by Ni doping below the SnS_2 CBM facilitated electron transfer and improved CO_2RR.

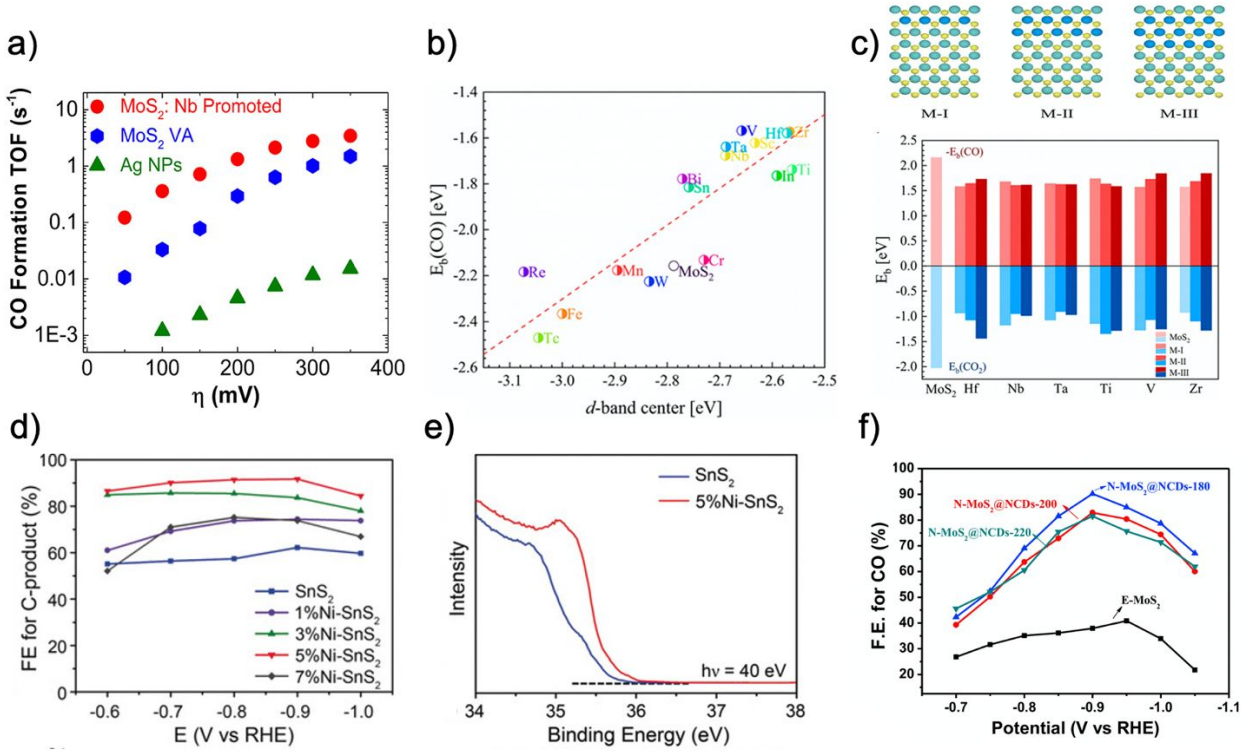

Fig. 12. a) Calculated CO formation TOF at different applied overpotentials for vertically aligned (VA)-$Mo_{0.95}Nb_{0.05}S_2$, pristine VA-MoS_2, and Ag nanoparticles. Reprinted with permission.[154] Copyright 2017 American Chemical Society. b) Relationship between the binding energies of CO and the d-band center energy positions for MoS_2 and transition metal-doped MoS_2. The transition metal atoms are all doped next to the Mo edge. c) Different transition metal-doped MoS_2 edge structures and binding energies of CO and CO_2 with different doping concentrations. Reprinted with permission.[166] Copyright 2020 American Chemical Society. d) Nickel doping in atomically thin SnS_2 nanosheets enables highly efficient CO_2 reduction. e) Secondary electron cutoff of photoelectron spectra for pristine SnS_2 and 5% Ni-SnS_2 nanosheets. Reprinted with permission.[167] Copyright 2018 John Wiley and Sons. f) The CO FE at different applied potentials for E-MoS_2 (exfoliated-MoS_2), N-MoS_2@NCDs-X (X: 180, 200, 220) electrodes in EMIM-BF4 solutions (94 mol% water), where NCD = nitrogen-doped carbon dots. Reprinted with permission.[168] Copyright Elsevier Inc.

Non-metal doping can also enhance MoS_2 catalytic activity. Nitrogen doping was found to enhance electron density on the Mo edge, decrease the energy barrier of COOH* intermediate formation, and weaken CO* adsorption strength for CO production.[168] As shown in (Fig. 12f), optimized composites of N-doped MoS_2 and N-doped carbon dots exhibited catalytic CO

production with FE_{CO} of 90.2% at −0.9 V vs. RHE and a low overpotential of 130 mV, superior to exfoliated MoS_2 (41.2%, 260 mV) and hydrothermal-synthesized MoS_2 (67%, 340 mV).

In addition to substitutional doping of TMDCs, alloying of multiple transition-metal elements in the 2D TMDC lattice has been explored for CO_2 electrocatalysis.[169] With the synergetic effects from low CO desorption energy by the presence of various transition metal sites and high electron transfer for minimum overpotential, the (MoWVNbTa)S_2 catalyst exhibited the formation of CO with a small onset potential of -0.129 V vs. RHE (19 mV overpotential). The extremely high activity was achieved with an excellent current density of 0.51 A cm^{-2} and a turnover frequency of 58.3 s^{-1} at -0.8 V vs. RHE. The FE for the formation of CO was maintained above 92 % at a potential between -0.31 V vs. RHE and -0.4 V vs. RHE, where H_2 evolution started to increase.

Engineering the metal atom on the exposed edges of TMDC could avail the CO_2RR, while ternary TMDCs with various chalcogenides also revealed the enhanced electrical conductivity and tailored *d*-band electronic structure of metal atoms. Xu *et al.* presented a theoretical calculation on ternary MoSeS alloy, confirming the faster electron transport ability by increased density of states near the conduction band edge compared to pristine MoS_2 and $MoSe_2$.[170] In addition, the asymmetry of Mo-S bond and Mo-Se bond from the different electronegativities of S and Se atoms partially deviated the charge density from the center of Mo atoms, which not only potentially benefits stabilizing the COOH* intermediate (confirmed by the most negative formation energy), but also facilitates the rate-limiting CO desorption step. Their experimental results showed the MoSeS alloy monolayers attain the highest 45.2% Faradaic efficiency for CO production, much larger than that of MoS_2 monolayers (16.6%) and $MoSe_2$ monolayers (30.5%) at −1.15 V vs. RHE.

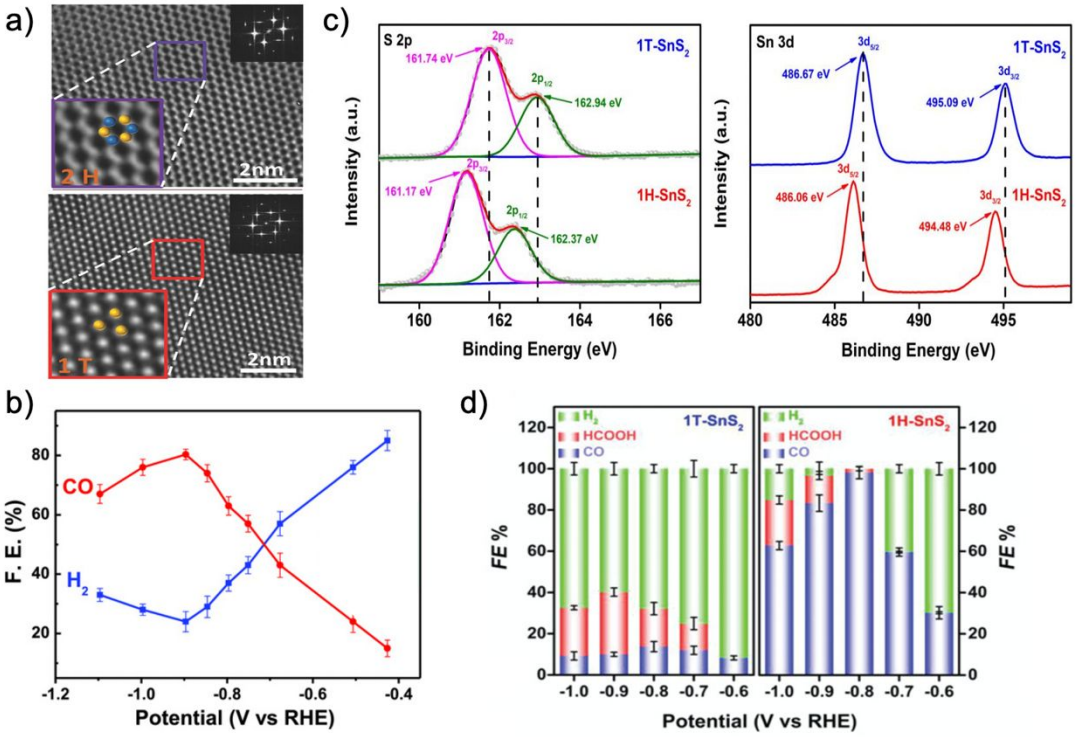

Fig. 13. a) HRTEM images of an exfoliated-MoS_2 nanosheet, showing atomic resolution structural information, and their corresponding fast Fourier transforms. (Insets show the 2H and 1T phases, top and bottom, respectively.) b) The hydrophobic exfoliated 1T MoS_2 shows the 81.2% FE of CO from CO_2 reduction. Reprinted with permission.[158] Copyright 2018 John Wiley and Sons. c) Deconvoluted S 2p and Sn 3d spectra of 1T-SnS_2 and 1H-SnS_2. d) FEs of CO, HCOOH, and H_2 at various applied potentials for 1T-SnS_2 and 1H-SnS_2. Reprinted with permission.[171] Copyright 2020 John Wiley and Sons.

The intrinsic semiconducting 2H phase of 2D MoS_2 is usually not ideal for electrochemical CO_2RR due to relatively poor charge transport. The 2H phase can be converted to the metallic 1T phase, and the 1T phase has exhibited facile kinetics, low resistance, and a high density of catalytic active sites.[172, 173] Lv *et al.* used high-resolution transmission electron microscopy (HRTEM) to show the two MoS_2 phases (Fig.13a). The metallic polymorph governed the FE of CO_2RR, which is higher than that of 2H MoS_2 as shown in Fig.13a. Further decoration with fluorosilane produced a more hydrophobic electrode surface, enhancing CO_2 transport to active sites and increasing FE_{CO} to 81.2% at (Fig. 13b).[158] Similarly, XPS results (Sn-3d and S-2p) demonstrate the conversion of the semiconducting phase (1T) of 2D SnS_2-based catalyst to the metastable semimetal phase (1H)

(Fig.13c) which enhanced CO_2RR activity, resulting in stable (> 15 h) and selective CO production.[166] Theoretical calculations showed that the *COOH intermediate was more stable on the 1H-SnS_2 surface than the 1T-SnS_2 surface. The 1H-SnS_2 catalyst exhibited a high FE of 98.2% at −0.8 V vs. RHE under ambient conditions while 1T-SnS_2 showed a maximum FE of 13.7% (Fig. 13d). This semimetal phase with excellent conductivity also has been observed for other TMDCs, displaying enhanced CO_2RR. Aljabour *et al.* showed excellent CO_2 conversion to CO and formate for semi-metallic TiS_2 with the combined Faradaic efficiency of 95% and overpotential below 0.4 mV at the current density of 5 mA cm^{-1}. The CO_2 molecules were bound to the 2D conductive sulfur planes in TiS_2 as intermediate monothiocarbonate, which conducts the reducing kinetics mainly toward CO.[174]

Another method to guide electrons to CO_2RR is forming heterostructures between TMDCs and other highly conductive CO_2RR active materials. Shi *et al*. dispersed ultrasmall Cu nanoparticles on flower-like MoS_2 for CO, C_2H_4, and CH_4 production from CO_2RR.[175] The ultrasmall Cu nanoparticles decreased HER compared to bare MoS_2, and the optimum Cu loading led to a 7-fold improvement to CH_4 production (Fig. 14a). A theoretical study by Li *et al.* showed significant electron transfer to the electron-deficient MoS_2 edge for effective CO_2RR when the MoS_2 edge was interfaced with N-doped carbon, even though the electron-rich N-doped carbon substrate was weakly bound to the MoS_2 edge.[176] The potential-determining step for MoS_2/N-doped carbon heterojunction was reduction of the *COOH intermediate to CO, whereas the potential-determining step for bare MoS_2 was formation of the *COOH intermediate from CO_2. This predicted electron donation from the N-doped carbon support to the exposed Mo edge sites could facilitate *COOH reduction to CO and recovery of the original active Mo site (Fig. 14b and c). Experimental studies of hydrothermally synthesized MoS_2/N-doped carbon electrocatalysts

found that the abundant active sites on MoS_2 exposed edges led to a low onset potential of ~40 mV and a remarkable FE_{CO} of 92.68% at -0.7 V vs. RHE (590 mV overpotential).[176] The activity remained stable for more than 24 h. He *et al.* integrated 2D SnS_2 nanosheets with Ag nanowires (NWs) for CO_2RR (Fig. 14d).[176] Owing to the similar E_f of the two materials, Ag NW free electrons participated in electron transport in the SnS_2/Ag NW heterojunction. Both defect sites and the increased carrier density in the heterojunction (5.5-fold larger than the bare SnS_2 nanosheet) enhanced the conductivity and binding strength for CO_2 and led to FE of carbon products (CO and formate) of ~84 % at -0.9 V vs. RHE. The FE of bulk SnS_2 and SnS_2 nanosheets were 77 % and 80%, respectively (Fig. 14e).

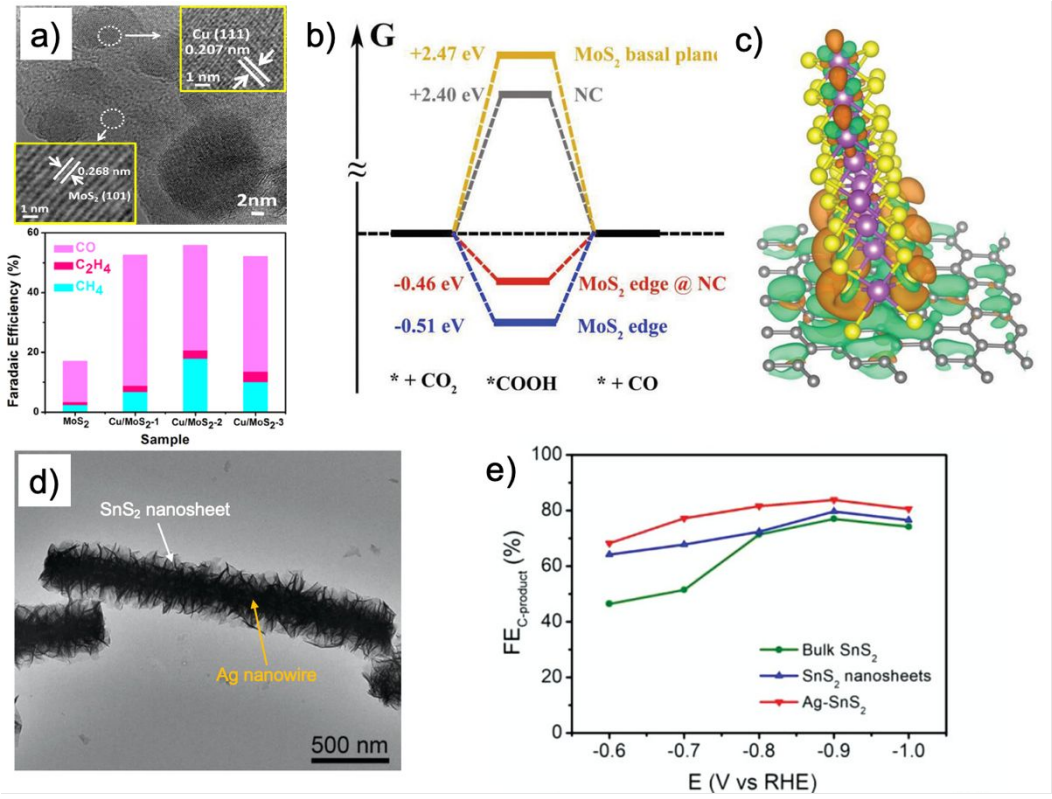

Fig. 14. a) Top panel: HRTEM of Cu/MoS_2 (the insets are the detailed image of white dashed circle); bottom panel: Faradaic efficiency of CO_2 reduction for different products over all prepared Cu/MoS_2 samples (-0.75 V vs. RHE). Samples Cu/MoS_2-1, Cu/MoS_2-2, Cu/MoS_2-3 are corresponding to the weight ratios of $Cu(NO_3)_2{\cdot}3H_2O$ to MoS_2 as 10%, 15%, and 20%. Reprinted with permission.[175] Copyright 2017 The Royal Society of Chemistry. b) The DFT calculations for demonstrating free energy profiles for CO_2RR catalyzed by different models at the equilibrium potential of −0.11 V. c) The illustration of charge density changes in the N-doped carbon (NC) and edge-exposed 2H MoS_2 model. The turquoise-colored regions represent hole density, and the brown-colored regions represent electron density, and thus it was expectable that the significant electron transfer from the NC substrate to the MoS_2 edge,

resulting in more active edges exposed. Reprinted with permission.[176] Copyright 2019 John Wiley and Sons. d) TEM image of Ag-SnS_2 hybrid nanosheets. e) Faradaic efficiencies for carbonaceous product over the three SnS_2-based catalysts. Reprinted with permission.[176] Copyright 2019 John Wiley and Sons.

Photoelectrochemical reactions use both photons and electrons to help drive the reaction. This type of reaction separates the photoinduced electron-hole pairs more efficiently *via* band bending generated by an external potential. In one example, 2D MoS_2 and $MoSe_2$ thin films were deposited on Si substrates by photoelectrochemical deposition of corresponding metal oxides, followed by thermal annealing with sulfur and selenium. Visible illumination of MoS_2/Si or $MoSe_2$/Si photocathodes increased the current density by 2.6 and 9.3 times compared to the dark electrochemical reaction, respectively, relative to bare Si. The authors argue that the narrower bandgap, and thus broader visible absorption, of $MoSe_2$ is the main reason for enhanced CO_2RR,[177] but more detailed mechanistic studies and product investigations are needed.

3.2.2 Photochemical CO_2RR

Many TMDCs are semiconducting in their few- or mono-layer forms. Strong (in many cases direct-bandgap) and tunable visible absorption[178, 179] in semiconducting TMDCs coupled with good charge transport and catalytic sites,[180] promote potential applications in *photochemical catalytic* reactions. However, only a few reports focus on the reduction of CO_2 using 2D TMDCs as photocatalysts, which makes this area promising for future exploration.

MoS_2 nanoflowers have been utilized to photoreduce CO_2 to CO in the gas phase, acting as both the photoabsorber and catalyst site (Fig. 15a).[136] The nanoflower shape increases the number of catalytically-active edge sites and the authors explored growth and post-growth conditions to manipulate flake edge morphology, lateral size, and MoS_2 thickness. A faster temperature ramp during CVD growth increased the nanoflower flake thickness and edge planes while post-synthetic H_2 treatment impacted stacking geometry and introduced more edge sites,

which decreased the band gap of MoS_2 from 1.83 eV to 1.38 eV. Simultaneously, structural strain stretched the lattice toward the unstable MoS_2 3R phase. The highest activity occurred for the small band gap material, which exhibited lower recombination and increased charge transport at thick edge sites and basal defect sites. A 30-min, post-treatment under reducing conditions (1% H_2/Ar) increased the photocatalytic CO generation rate from ~0.17 (non-treated) to ~0.35 μmol g_{cat}^{-1} h^{-1}.

2D MoS_2 sheets with the co-existence of 2H and 3R phases were also explored for CO_2 photoreduction,[181] where ultraviolet illumination generated CH_3OH and CH_3CHO (Fig. 15b). Manipulating the electrolyte cations influenced scavenging of photoinduced holes, providing a different number of accumulated electrons for selective CO_2RR product generation. Using $NaHCO_3$ medium, 27.4 μmol g_{cat}^{-1} h^{-1} CH_3OH and 2.2 μmol g_{cat}^{-1} h^{-1} CH_3CHO were produced; while Cl^- in NaCl solution acted as an efficient hole scavenger for higher-order hydrocarbon products to give a production rate of 7.8 μmol g_{cat}^{-1} h^{-1} for CH_3OH and 4.8 μmol g_{cat}^{-1} h^{-1} for CH_3CHO (Table 2).

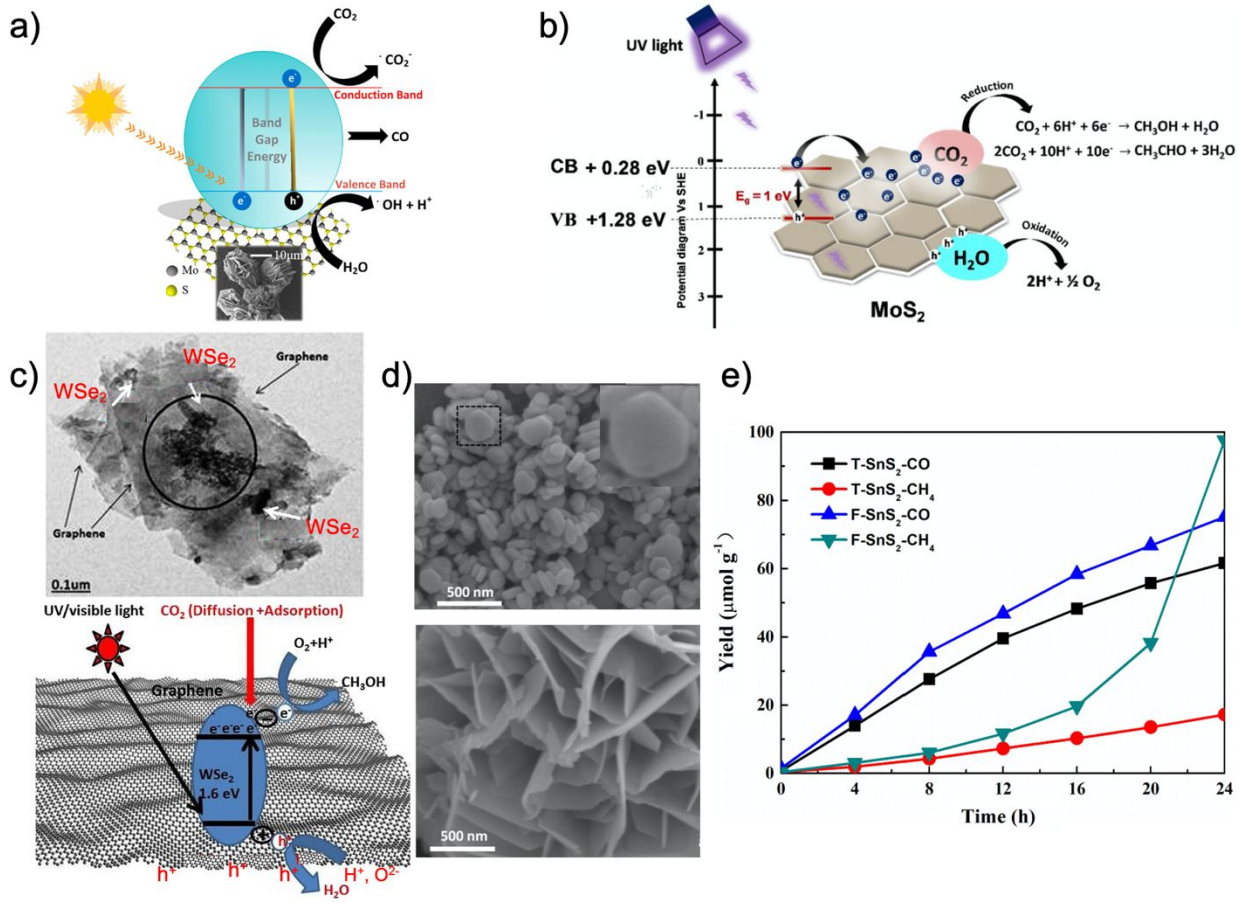

Fig. 15. a) MoS_2 nanoflowers for gas-phase CO_2 photoreduction to generate CO. Reprinted with permission.[136] Copyright 2019 American Chemical Society. b) Photocatalytic CO_2RR over MoS_2 nanosheets to produce CH_3OH and CH_3CHO. Reprinted with permission.[181] Copyright 2019 Elsevier Inc. c) TEM image of WSe_2-graphene and possible carriers transport scheme of photocatalytic reduction of CO_2. Reprinted with permission.[137] Copyright 2017 Nature Publishing Group. d) SEM images of T-SnS_2 (top) and F-SnS_2 (bottom). e) CH_4 and CO yield under visible-light irradiation for T-SnS_2 and F-SnS_2. Reprinted with permission.[182] Copyright 2020 Elsevier Inc.

Photocatalytic CO_2RR has also been achieved for 2D WSe_2. WSe_2–graphene nanocomposites were synthesized *via* ultra-sonication and measured under irradiation with UV/visible light for photocatalytic CO_2 reduction to CH_3OH (Fig. 15c)[137] The nanoscale morphology of the as-synthesized WSe_2–graphene powder included nanoparticles, nanowire, and several-layer nanosheets. The binary structure of WSe_2 and graphene promoted electron transport and suppressed electron–hole recombination compared to pure WSe_2, resulting in CH_3OH yields of ~3.55 μmol g^{-1} h^{-1} under visible light and 2.35 μmol g^{-1} h^{-1} under UV light for 48 h. Coupling

with sacrificial agent Na_2SO_3 further enhanced photocatalytic CO_2RR activity, with CH_3OH yields of 4.33 μmol g^{-1} h^{-1} and 5.03 μmol g^{-1} h^{-1}, respectively.

It is well known that catalyst morphology affects catalytic activity due to unique adsorption energies and catalytic activities of different crystal facets.[183-185] Li *et al*. confirmed this principle for photocatalytic CO_2RR in TMDCs by synthesizing and comparing tablet-like (T) and flower-like (F) SnS_2 flakes.[182] While both morphologies were in the 2T phase, they were dominated by different facets, with the [0 0 1] direction being inhibited in F-SnS_2. The smaller thickness compared to the electron mean-free-path shortened the carrier diffusion time to the catalyst surface in F-SnS_2. The flower-like morphology (Fig. 15d) also had larger specific surface area and Sn^{2+} surface defects. While F-SnS_2 produced 5.7× higher yield of CH_4 compared to the T-SnS_2, the main CO_2RR product on both catalysts was still CO (Fig. 15e), except for the very last time point (24 h).

Doping is another route to influence CO_2RR activities of 2D TMDC photocatalysts. Billo *et al.* studied selective photocatalytic CO_2 reduction to CH_4 in carbon-implanted 2D SnS_2 thin films grown by chemical vapor transport.[186] As shown in Fig. 16a, both CBM and VBM of carbon doped SnS_2 (C-SnS_2) shift downward by 0.24 and 0.13 eV compared to the as-grown SnS_2, leading to better redox potentials for multielectron CO_2 reduction and H_2O oxidation. This C–SnS_2 sample demonstrated high densities of surface electrons and CO_2 adsorption sites, discrete electronic states, enhanced charge mobility and light harvesting, and reduced electron-hole recombination. These C-SnS_2 properties resulted in over two orders of magnitude enhancement in CO_2 conversion efficiency—relative to SnS_2—and about 89% product selectivity toward CH_4 formation as shown in Fig. 16b.

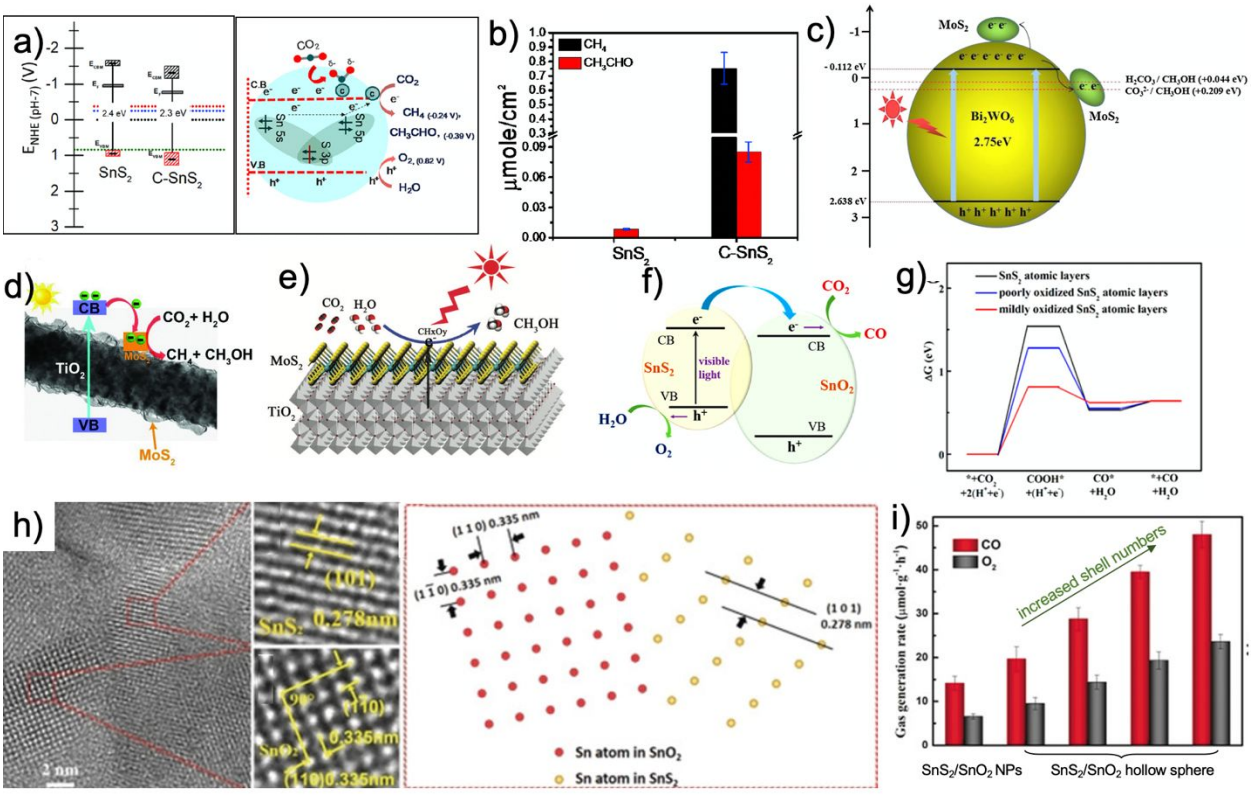

Fig. 16. Photocatalytic CO_2 reduction activity and the reaction mechanism using different 2D TMDCs. a) (Left panel) Comparative band diagram of SnS_2 and C–SnS_2 showed the band position shifting downward by C doping. Different reduction potentials are present in red (CH_3CHO), blue (CH_4), and black (H_2) horizontal dotted lines, and (right panel) schematic of the reaction mechanism and charge transfer behavior. b) Cumulative CO_2 conversion to CH_4 and CH_3CHO using SnS_2 and C–SnS_2 photocatalysts during 6 h reaction time under a visible light source (AM 1.5 solar simulator). Reprinted with permission.[186] Copyright 2020 Elsevier Inc. c) Schematic for CO_2 reduction using Bi_2WO_6/MoS_2 catalysts to generate methanol. Reprinted with permission.[187] Copyright 2017 Elsevier Inc. d) 1D/2D TiO_2/MoS_2 is used to photoreduce CO_2 to methane and methanol. Reprinted with permission.[169] Copyright 2018 John Wiley and Sons. e) Schematic illustration of the charge separation and transfer in the MoS_2/TiO_2 system for the photoreduction of CO_2 to CH_3OH, and Mo sites especially Mo-terminated edges on MoS_2 nanosheets stabilize the intermediate products (CH_xO_y). Reprinted with permission.[188] Copyright 2017 The Royal Society of Chemistry. f) Diagram of the energy band structure and electron transfer in the SnS_2/SnO_2 composite semiconductors. g) Free energy diagrams of CO_2 photoreduction to CO for the SnS_2 atomic layers, the poorly oxidized SnS_2 atomic layers, and the mildly oxidized SnS_2 atomic layers. Reprinted with permission. [189] Copyright 2017 American Chemical Society. h) HRTEM image of SnS_2/SnO_2 with schematic (right panel) showing the lattice distortion at the SnS_2/SnO_2 interface. i) Photocatalytic CO_2 reduction of SnS_2/SnO_2 nanoparticles and hollow spheres with different numbers of shells. Reprinted with permission.[190] Copyright 2020 John Wiley and Sons.

Although the strategies of phase engineering, doping, and introducing defects in pristine TMDC materials are promising avenues for CO_2RR activity enhancement, investigating other TMDC materials with unique intrinsic photochemical properties among the 40+ TMDC family members could be another essential route to achieve highly efficient CO_2RR photocatalysts. As a

narrow bandgap (~1.5 – 1.6 eV) TMDC, ReS_2 with direct band gap has significant visible and near-IR absorbance. Weak interlayer coupling in ReS_2, compared to other TMDCs, leads to more exposed active sites and lower energetic barriers for interlayer molecular diffusion. Trion formation in ReS_2 also would not necessarily depend on the precise control of layer number.[191] These advantages make ReS_2 a promising photo-catalytic candidate.[192, 193] Zhang *et al.* reported a heterojunction composed of 2D ReS_2 nanosheets and CdS nanoparticles for photocatalytic CO_2 reduction. Because of the high-efficiency interfacial photogenerated electron–hole separation and migration as well as the adsorption/activation of CO_2 intermediates from surface sulfur vacancies, the ReS_2/CdS heterostructure exhibited a high photocatalytic CO yield of 7.1 μmol g^{-1} with a high selectivity of 93.4% over 7 hours.[194]

Similar as above, integrating a 2D TMDC with another semiconductor in a Type-II (staggered band) heterostructure is a simple way to increase optical absorption and improve photocatalytic activity. In such heterojunctions, the 2D TMDC serves as surface catalyst for charge transfer and stabilizing intermediates, while another semiconductor serves as the photoactive absorber. Dai *et al.* combined Bi_2WO_6 nanoflowers with a few-layered MoS_2 co-catalysts for CO_2 photoreduction into methanol and ethanol.[187] Photoinduced charge separation at the Bi_2WO_6/MoS_2 interface yielded electron transfer to MoS_2 for reduction reactions, resulting in 36.7 μmol g_{cat}^{-1} of methanol and 36.6 μmol g_{cat}^{-1} of ethanol after 4 h of visible light excitation. The authors propose that CO_2 in aqueous solutions produces CO_3^{2-}, HCO^{3-}, and H_2CO_3, which are reduced on the few-layered MoS_2 (Fig. 16c).

Another heterostructure configuration employed for 2D TMDC CO_2RR photocatalysts was demonstrated by coupling 2D MoS_2 to TiO_2.[195, 196] Under UV-vis illumination, photoexcited electrons in 1D TiO_2 are transferred to 2D MoS_2 and used for CO_2RR (Fig. 16d). In this catalytic

reaction, methane and methanol are produced at 2.86 and 2.55 μmol g^{-1} h^{-1}, respectively. The possible mechanism for methanol production was detailed in another work;[188] where, it was proposed that photoexcited electrons in TiO_2 transfer to Mo sites, where they participate in CO_2 reduction with the CH_xO_y intermediates stabilized on Mo-terminated edges (Fig. 16e).

Efficient charge transfer across heterostructure interfaces can be achieved by low-dimensional TMDC layers that produce a depletion region with large electric fields that can be created by *in-situ* synthesis.[197, 198] Jiao *et al.* presented a facile *in-situ* oxidization of 2D SnS_2 to achieve atomically bonded SnO_2/SnS_2 heterostructures for visible light CO_2 photoreduction, where the SnO_2 layer has high electron conductivity and SnS_2 efficiently absorbs light.[189] As predicted by the band structure diagram (Fig. 16f) and simulation results (Fig. 16g), this atomically thin SnS_2/SnO_2 heterojunction supports electron-hole separation and active site exposure, while electron localization on Sn atoms lowers the CO_2 activation energy barrier through stabilizing the COOH* radical intermediate. The mildly oxidized SnS_2 atomic layers resulted in a CO formation rate of 12.28 μmol g^{-1} h^{-1}, roughly 2.3 and 2.6 times higher than those of the poorly oxidized SnS_2 atomic layers and the SnS_2 only atomic layers, respectively. By utilizing the reverse process, You and co-workers sulfurized hollow multi-shelled structured SnO_2 to create a SnS_2/SnO_2 heterostructure.[190] Sulfurization introduced a large amount of oxygen vacancies and interfacial lattice distortions (Fig. 16h) that increased the active sites for CO_2 adsorption. Additionally, reflection and scattering in the hollow spherical multi-shell structure increased light absorption, relative to the planar SnO_2/SnS_2 heterostructure. These advantages led to 100 % CO selectivity with a production rate of 47.5 μmol g^{-1} h^{-1} for over 20 h (Fig. 16i).

TMDCs have been interfaced with other nanomaterials for CO_2RR. Lu *et al.* hydrothermally synthesized 2D MoS_2-wrapped $Mn_{0.2}Cd_{0.8}S$ nanospheres with varying weight

percentages of MoS_2 to tune photocatalytic activity.[198] Photoinduced electrons are transferred from $Mn_{0.2}Cd_{0.8}S$ to MoS_2 to reduce CO_2 to CH_3OH (Fig. 17a). The heterostructure with an optimal MoS_2 loading of 3 wt% yielded 2.13 μmol h^{-1} of CH_3OH, which was 5.4 times more than bare $Mn_{0.2}Cd_{0.8}S$ nanospheres (Fig. 17b). $NiSe_2$, a high electrical conductivity TMDC was interfaced with WSe_2 for photocatalytic CO_2 reduction into methanol.[199] When $NiSe_2$ was incorporated into the hydrothermal synthesis process of WSe_2, it reduced the size of WSe_2 flakes, which maintained the rich exposed edges and active sites. The specific surface area increased to 8.52 $m^2 g^{-1}$ compared to 3.01 $m^2 g^{-1}$ of bare WSe_2 flakes sample. The $NiSe_2/WSe_2$ catalyst showed 380 μmol $g^{-1}h^{-1}$ yield of CH_3OH from CO_2RR, which is more than 3 times of bare WSe_2 catalyst.

Compared to the Type II heterostructure configuration, an all-solid-state artificial Z-scheme heterojunction has been considered as a more efficient photocatalyst by expanding the light absorption spectrum and providing long-lived, photoinduced electrons and holes. In a Z-scheme, both sides of the interface absorb photons and the lowest energy photoexcited electrons and holes recombine leaving behind high-energy electrons and holes on each side of the interface. As an example, 2D MoS_2/SiC nanoflower interfaces support oxidation on the MoS_2 side and reduction on the SiC side (Fig. 17c and d).[200] This Z-scheme interface yields CH_4 and O_2 at 323 and 621 μL g^{-1} h^{-1}, respectively, under visible light without sacrificial reagents. Another Z-scheme heterojunction for CO_2 photoreduction was constructed by fabricating MoS_2/g-C_3N_4 composites (Fig. 17e).[201] The MoS_2/g-C_3N_4 composites have strong visible light response, efficient exciton dissociation, and high specific surface area. This Z-scheme optimally generates CO (58.59 μmol g_{cat}^{-1}) with 10 wt% MoS_2/g-C_3N_4 catalyst for 7 h with visible light irradiation, which was up to three times more than bare g-C_3N_4.

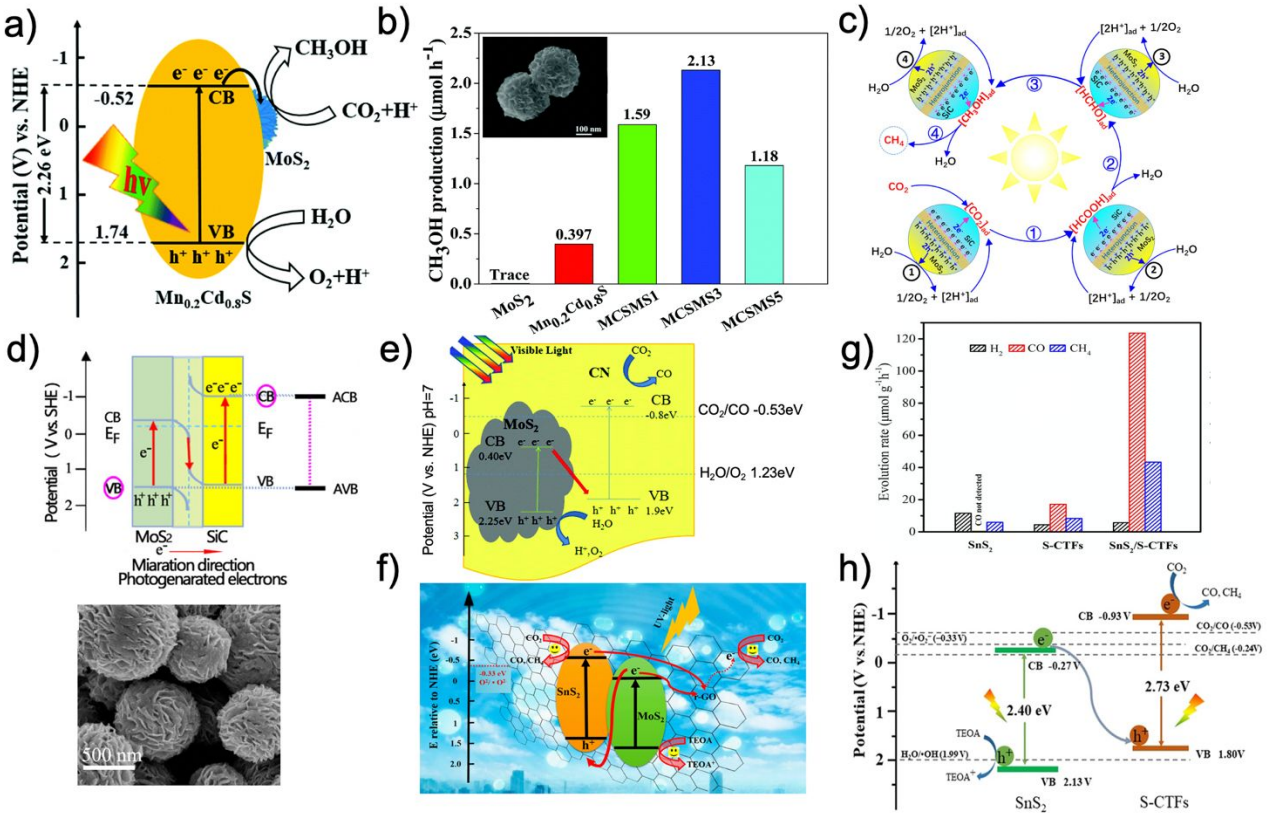

Fig. 17. a) Reaction energetics for the improved activity of $MoS_2/Mn_{0.2}Cd_{0.8}S$ nanosphere composites for CO_2 photoreduction. b) CH_3OH production rate comparison among MoS_2, $Mn_{0.2}Cd_{0.8}S$ and $MoS_2/Mn_{0.2}Cd_{0.8}S$ composites: MCSMSX, where X is the wt% of MoS_2. Inset is the SEM image of $MoS_2/Mn_{0.2}Cd_{0.8}S$ composite. Reprinted with permission.[198] Copyright 2020 The Royal Society of Chemistry. c) and d) MoS_2 interfaced with SiC undergoes a Z-scheme redox reaction to reduce CO_2 and oxidize H_2O. Bottom panel of d) is the SEM morphology of MoS_2@SiC. Reprinted with permission.[200] Copyright 2018 American Chemical Society. e) Z-scheme band energetics of the MoS_2 and g-C_3N_4 interface for CO_2 photoreduction. Reprinted with permission.[201] Copyright 2018 The Royal Society of Chemistry. f) Z-scheme band energetics of MoS_2/SnS_2/r-GO system under UV light irradiation which increases charge separation to photoreduce CO_2 to CO and CH_4. Reprinted with permission.[202] Copyright 2019 American Chemical Society. g) Comparison of average gas production rates of SnS_2, S-covalent triazine frameworks (CTFs), and SnS_2/S-CTFs. h) Schematic diagram of the photogenerated charge separation and transfer in SnS_2/S-CTFs. Reprinted with permission.[203] Copyright 2020 John Wiley and Sons.

Z-schemes can also be constructed by interfacing 2D materials together. Yin *et al.* reported 2D MoS_2/SnS_2/reduced graphene oxide (r-GO) heterostructures for ultraviolet light CO_2 reduction.[202] Reduced graphene oxide provided the high specific surface area, conductivity, and carrier mobility needed for efficient CO_2RR. Electron spin resonance spectroscopy revealed the composite of MoS_2/SnS_2/r-GO has preferred active species for production of superoxide radicals ($\bullet O_2^-$), indicating a more negative CBM potential compared to the redox potential E ($O/\bullet O_2^-$) (-

0.33 eV vs. NHE). Since the CBM of individual SnS_2 is more negative than E ($O/•O_2^-$) but that of individual MoS_2 is more positive than E ($O/•O_2^-$), the Z-scheme energetics suggest that SnS_2 electrons produce superoxide, while the MoS_2 CB electron recombines with the VB hole of SnS_2 (Fig. 17f). The yield of CO and CH_4 was 173- and 222-fold higher than bare MoS_2 photocatalyst, respectively.

Z-scheme interfaces pairing SnS_2 with other materials have been reported for CO_2RR, including g-C_3N_4/Au/SnS_2,[204] SnS_2/TiO_2,[205, 206] and $SnS_2/SrTiO_3$.[182] In these heterostructures, product selectivity and light absorption were governed by the semiconductor other than SnS_2, which enhanced CO_2 photoreduction performance. Guo *et al.* used 2D SnS_2/triazine frameworks for a Z-scheme CO_2 photocatalyst.[203] The covalent triazine framework (CTF) captured and activated CO_2 molecules.[207, 208] The addition of 2D SnS_2 to the covalent triazine framework improved electronic conductivity, carrier lifetime, and efficiency of the bare covalent triazine framework. Both CO_2 uptake and reduction yield of the SnS_2/triazine framework showed remarkable improvement of CO and CH_4 generation compared to the individual components (Fig. 17g).[203]

Table 2. Summary of Experimental CO_2RR works by 2D TMDCs-based catalyst.

Materials	Condition	Activity	Product	Reference
		Electrochemical Process		
Nb-doped MoS_2	CO_2 and EMIM−BF_4 solution	~31 mV overpotential, TOF = 0.36s^{-1} (overpotential=100 mV)	CO	154
Single-crystal MoS_2 film	N_2-purged KH_2PO_4 with Na_2CO_3 solution	$FE_{1\text{-propanol}}$=~3.5% (MoS_2 single crystals) $FE_{1\text{-propanol}}$=~1% (MoS_2 thin film)	C_3H_8O, HCOOH, $C_2H_6O_2$, $C_4H_{10}O$	144

Vertically aligned MoS_2 Nanoflakes	CO_2 with EMIM-BF_4 solution	FE_{CO}=98% (overpotential = 650 mV)	CO	155
Cu/MoS_2	CO_2-saturated $NaHCO_3$ solution	Max. FE_{CO} = 43.81% Max. FE_{CH4} =17.08% Max.FE_{C2H4}=3.45%	CO C_2H_4 CH_4	175
MoS_2, $MoSe_2$, WS_2, WSe_2 Nanoflakes	CO_2 and EMIM−BF_4 solution	FE_{CO} =24% (overpotential= 54 mV), TOF= 0.28s^{-1} (-0.164 V vs. RHE)	CO	159
Ultrathin $MoTe_2$	CO_2-sparged [Bmim]BF_4 solution	FE_{CH4} = 83 ± 3% (25.6 mA cm^{-2} at −1.0 V vs. RHE)	CH_4	161
TiS_2	NBu_4-PF_6 and EMIM-BF_4 in acetonitrile water	FE_{CO} =83% (−0.5 V vs. RHE, 390 mV overpotential, 5 mA cm^{-2})	CO HCOOH	174
MoS_2/N-Carbon	CO_2 Emim-BF_4 solution	FE_{CO} = 92.68% (34.31 mA cm^{-2}, 590 mV overpotential)	CO	176
Fluorosilane Decorated Exfoliated MoS_2	CO_2-saturated EMIM-BF4 solutions	FE_{CO} = 81.2% (−0.9 V vs. RHE)	CO	158
rGO/PEI/MoS_x	CO_2 sparged $NaHCO_3$ solution	~140 mV overpotential, FE_{CO} = 85.1 %, TOF=2.4s^{-1} (overpotential 540 mV)	CO	159
Photoelectrochemical Process				
2D MoS_2, $MoSe_2$/Si	CO_2 sparged $NaHCO_3$ electrolyte	2.2 (MoS_2/Si) and 1.2 ($MoSe_2$/Si) times higher current density (CO_2), 2.6 (MoS_2/Si) and 9.4 ($MoSe_2$/Si) times higher current density (light),	N/A	177
Photochemical Process				
MoS_2 nanoflowers	CO_2 in H_2O, ~589 Wm^{-2} illumination (400-700 nm)	0.22 to 0.35 µmol $gcat^{-1}$ h^{-1}	CO	136
WSe_2	$NaHCO_3$ solution Xe Lamp (>420 nm)	115 µmol g^{-1} h^{-1}	CH_3OH	199

ReS_2/Cds	0.5 M Na_2SO_4 aqueous solution Xe Lamp (>420 nm)	1.01 μmol g^{-1} h^{-1}	CO	194
MoS_2/SiC	CO_2 with H_2O vapor, Visible light	323 μL g^{-1} h^{-1}	CH_4	200
MoS_2/g-C_3N_4	CO_2 with H_2O vapor, Xe Lamp	8.37 μmol g^{-1} h^{-1}	CO	201
MoS_2/Bi_2WO_6	CO_2 in H_2O, Visible light	36.7 μmol $gcat^{-1}$ (Methanol) 36.6 μmol $gcat^{-1}$ (ethanol)	CH_3OH, CH_3CH_2OH	187
1D TiO_2/2D MoS_2	CO_2 with H_2O vapor, Xe Lamp	2.86 μmol g^{-1} h^{-1} (Methane) 2.55 μmol g^{-1} h^{-1} (Methanol)	CH_4, CH_3OH	196
TiO_2/MoS_2 Nanosheet	CO_2 saturated $NaHCO_3$ solution, Xe Lamp	3.1 – 10.6 μmol g^{-1} h^{-1}	CH_3OH	188
MoS_2/$Mn_{0.2}Cd_{0.8}S$	CO_2 saturated NaOH solution Xe Lamp (>420 nm)	1.18 – 2.13 μmol g^{-1} h^{-1}	CH_3OH	198
$NiSe_2$/WSe_2	$NaHCO_3$ solution Xe Lamp (>420 nm)	380 μmol g^{-1} h^{-1}	CH_3OH	199
WSe_2/graphene	$NaHCO_3$ solution Visible light and UV light	3.55 μmol g^{-1} h^{-1} (visible light) 2.35 μmol g^{-1} h^{-1} (UV light) sacrificial agent-Na_2SO_3: 4.33 μmol g^{-1} h^{-1} (visible light) 5.03 μmol g^{-1} h^{-1} (UV light)	CH_3OH	137
2H and 3R phase MoS_2	$NaHCO_3$, NaOH, and NaCl solution, UV light (254 nm)	In $NaHCO_3$: 27.4 μmol g-1 h^{-1} (CH_3OH) and 2.2 μmol g-1 h^{-1} (CH_3CHO). In NaOH: 11.2 μmol g-1 h^{-1} (CH_3OH) and 2.5 μmol g-1 h^{-1} (CH_3CHO). In NaCl: 7.8 μmol g-1 h^{-1} (CH_3OH) and 4.8 μmol g-1 h^{-1} (CH_3CHO).	CH_3OH, CH_3CHO	181

MoS_2/g-C_3N_4	CO_2 with H_2O vapor, Xe Lamp	8.37 μmol g^{-1} h^{-1}	CO	201
MoS_2/Bi_2WO_6	CO_2 in H_2O, Visible light	36.7 μmol $gcat^{-1}$ (Methanol) 36.6 μmol $gcat^{-1}$ (ethanol)	CH_3OH, CH_3CH_2OH	187
1D TiO_2/2D MoS_2	CO_2 with H_2O vapor, Xe Lamp	2.86 μmol g^{-1} h^{-1} (Methane) 2.55 μmol g^{-1} h^{-1} (Methanol)	CH_4, CH_3OH	196

3.3 MXene

3.3.1 Electrochemical CO_2RR

The viability of MXene catalysts for CO_2RR was recently investigated by computational screening.[153, 209] The activity and selectivity of CO_2 reduction over MXenes are closely related to the hydrogenation process and surface-terminated active sites. Hydrogenation of CO_2 on M_3C_2 (M = Sc, V, Mn, Zr, Nb, Hf, Hf, Mo, and W) MXene surfaces was theoretically studied by Xiao *et al.*[19] The calculation results predicted two mechanisms, distinguished by the first protonation step, for CO_2RR over M_3C_2 MXenes, with methane as the final product. The formation of bicarbonate intermediate species $*HCO_2$, from CO_2 and successive protonation ($*HCO_2$ → $*H_2CO_2$ → $*H_2CO_2$ → $*H_2COOH$ → $*H_2CO$ → $*H_3CO$ → *O (+ $*CH_4$) → *OH → $*H_2O$), is the energetically favorable pathway for most studied MXenes, whereas the mechanism of *COOH → *HCOOH → *CHO → *HCHO → $*H_2COH$ → $*H_3COH$ → $*CH_3$ → $*CH_4$ is more favorable on Ta_3C_2 and W_3C_2. Such binding features of $*HCO_2$ or *COOH were suggested to be determined by the M–O–C or M–C–O binding.

Further experimental investigation was conducted on the hydrogenation of CO_2 on pristine β-Mo_2C and β-Mo_2C modified with Cu nanoparticles in a gas-phase reactor by Posada-Pérez *et al.,*[84] which showed the surface-determining CO_2RR activity and selectivity phenomena. The results revealed the direct activation and dissociation of the CO_2 molecule to methane and CO on

clean β-Mo_2C, whereas hydrogen-assisted CO_2RR occurred on Cu/β-Mo_2C for CO and methanol production. It is believed that CO* and H_3CO* dissociation are favorable processes on bare β-Mo_2C surfaces for methane and CO. New routes involving the hydrogenation of CO_2* for the formation of HCOO* and subsequent H_2COO* at the interface of Cu/β-Mo_2C could ultimately produce CH_3O* and then CH_3OH. These observations demonstrate a critical aspect of MXenes—even the surface of pristine MXenes can dissociate highly stable molecules such as CO_2, which are normally the rate-determining steps of the studied reactions. The activity and selectivity for CO_2 hydrogenation can be controlled by basal plane modification. Such low energy barriers are also featured on clean patches of MXenes for efficient catalytic dry reforming of methane from CO_2RR.[85]

The influence of oxygen and hydroxide MXene-termination groups on CO_2RR has also been theoretically investigated. Owing to the hydrogen-bond interaction between *HCOOH and the surface groups, particularly -O, the unique CO_2RR behavior on Ti_2CT_x and Mo_2CT_x MXenes has been noticed, where the *HCOOH pathway dominates the surface CO_2RR instead of the typical *CO pathway over most transition metal catalysts. The C atoms on the MXene surface determine the type of surface groups. In general, *COOH binds to the -OT_x group on MXene surfaces through the C atom, whereas *HCOOH binds through the H atom. Such *HCOOH intermediate preferences result in non-linear scaling with *COOH in terms of their binding energies, as these two intermediates are coordinated differently on the MXene surfaces.[210] With -O and -OH surface functionalization, the energy barrier for CO_2 reduction to CH_4 over $Cr_3C_2T_x$ and $Mo_3C_2T_x$ could be reduced compared to the unfunctionalized MXenes.[211] Handoko and co-workers reported a CO_2 reduction pathway on O-terminated MXene catalysts that preferentially binds *CO to selectively generate CH_4 at low overpotentials. They concluded that

W_2CO_2 and Ti_2CO_2 are highly promising MXenes for CO_2RR to form CH_4 with theoretical overpotentials of 0.52 and 0.69 V, respectively (Fig. 18a).[212]

Chen *et al*. utilized thermodynamic and kinetic first-principle approaches to study CO_2 reduction over various (−OH)-terminated M_2C and M_2N MXenes (M = Hf, Nb, Sc, Ta, Ti, V, Y, and Zr). The simulations resulted in the potential-limiting step of *(H)COOH → *CO for most OH-terminated MXenes, where the adsorbed *CO is stabilized by capturing H atoms from the OH termination group. Due to the proximity to the peak of the volcano curve, $Sc_2C(OH)_2$ and $Y_2C(OH)_2$ (Fig. 18b) were identified as the most promising catalysts for CO_2 to CH_4 conversion with the least negative limiting potential of -0.53 V and -0.61 V, respectively, in aqueous reaction conditions.[152]

Although experimental studies on the role of MXene-termination groups for CO_2RR are still rare, a few pioneering studies have been reported. In the experimental work by Handoko *et al*., formic acid was the main CO_2 reduction product on Ti_2CT_x and Mo_2CT_x MXenes, where a maximum FE of over 56% at 0.17 V vs. RHE was observed for Ti_2CT_x. According to their DFT results, CO_2RR activity depended on the Ti_2CT_x fraction of –F and –O surface termination groups, where lower amounts of –F and higher amounts of –O led to lower potential energy steps for formic acid generation (Fig. 18c).[210] The impact of oxygen terminated MXenes on CO_2RR was further explored in detail by Attanayake *et al.*[213] The DFT results indicated that the surface-terminated oxygen vacancies performed as CO_2RR active sites. With regards to the free energy, CO_2 exhibited weak binding at the vacancy site on oxygen terminated Ti_3C_2, while it is physically adsorbed at the oxygen vacancy on the oxygen terminated Mo_2C. Following activation of $*CO_2$ to *COOH, the hydrogenation step required 0.26 eV less free energy input of Mo_2C compared to Ti_3C_2, which spontaneously dissociated and formed H_2O and *CO, promoting better CO_2RR on

Mo_2C (Fig. 18d). Adding the ionic liquid 1-ethyl-2-methylimidazolium tetrafluoroborate as an electrolyte in acetonitrile suppressed the competing HER, and Mo_2C and Ti_3C_2 exhibited Faradaic efficiencies of 90% (250 mV overpotential) and 65% (650 mV overpotential), respectively. To the best of our knowledge, there are no reports of photoelectrochemical CO_2RR; however, there are a few reports of photochemical CO_2RR with MXenes.

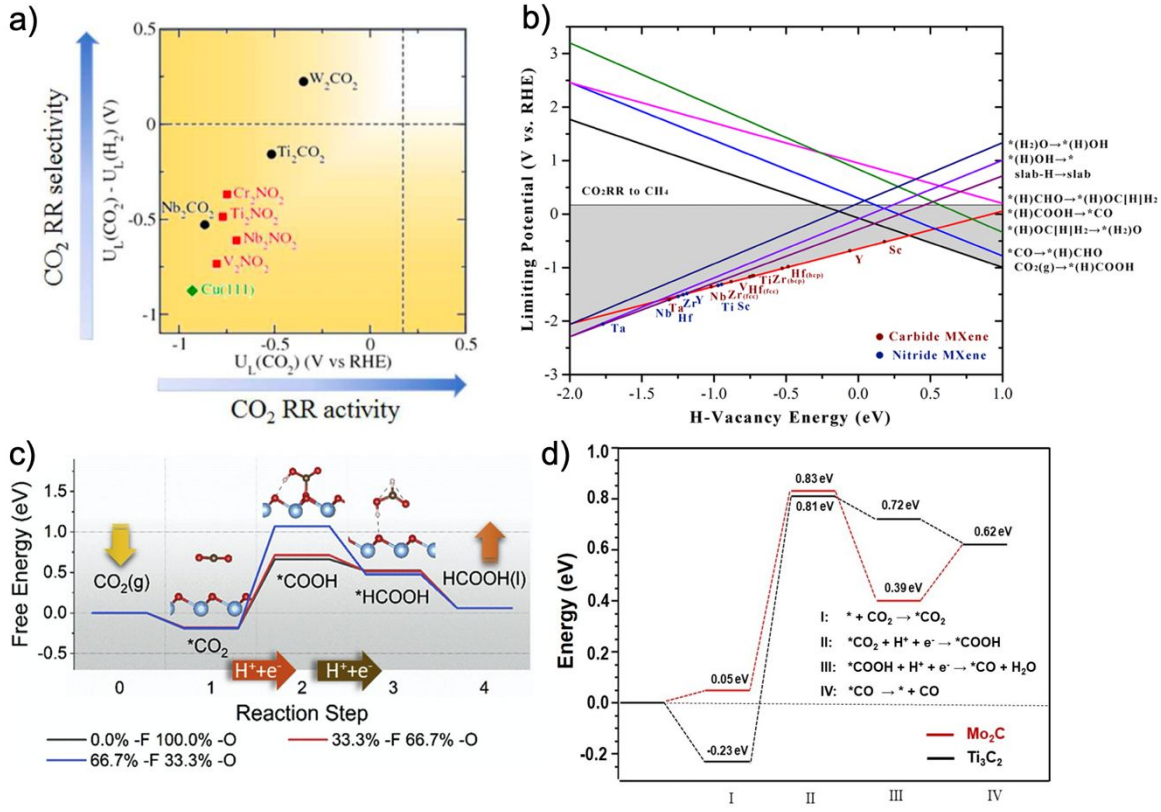

Figure 18. a) O-terminated MXenes display low theoretical overpotential for CO_2RR. Plot of $U_L(CO_2) - U_L(H_2)$ as a function of $U_L(CO_2)$ showing the selectivity of CO_2RR to generate CH_4 relative to HER for MXenes. Vertical line marks the equilibrium potential for the reduction of CO_2 to CH_4 (0.17 V vs. RHE). Reprinted with permission.[212] Copyright 2018 The Royal Society of Chemistry. b) Volcano curve of OH-terminated MXenes to generate CH_4. For most OH-terminated MXenes, the potential-limiting step is determined to be *(H)COOH → *CO. The equilibrium potential for CO_2RR to CH_4 is 0.17 V vs. RHE. Reprinted with permission.[152] Copyright 2019 American Chemical Society. c) DFT results for CO_2RR to generate formic acid on Ti_2CT_x with varying ratios of T_x. Reprinted with permission.[210] Copyright 2020 Elsevier Inc. d) The free energy diagram for CO_2RR at the oxygen vacancy on Ti_3C_2 (in black) and Mo_2C (in red) calculated using the PBE functional. Reprinted with permission.[213] Copyright 2021 The Royal Society of Chemistry.

3.3.2 Photochemical CO_2RR

Both computational and experimental results indicate that MXenes can exhibit high carrier mobilities and appropriate band gaps (when semiconducting) for photocatalytic CO_2 reduction. Zhang *et al*. theoretically investigated CO_2 photoreduction at oxygen vacancies on three MXene monolayers (Ti_2CO_2, V_2CO_2, and $Ti_3C_2O_2$) and found the best performance from monolayer Ti_2CO_2, a semiconductor with 0.91 eV band gap and large electron mobility.[151, 214] They proposed that incomplete O-termination, along with CO and H_2 introducing additional oxygen vacancies, promoted the selective reaction pathway of $CO_2 \rightarrow HCOO \rightarrow HCOOH$.[151, 214]

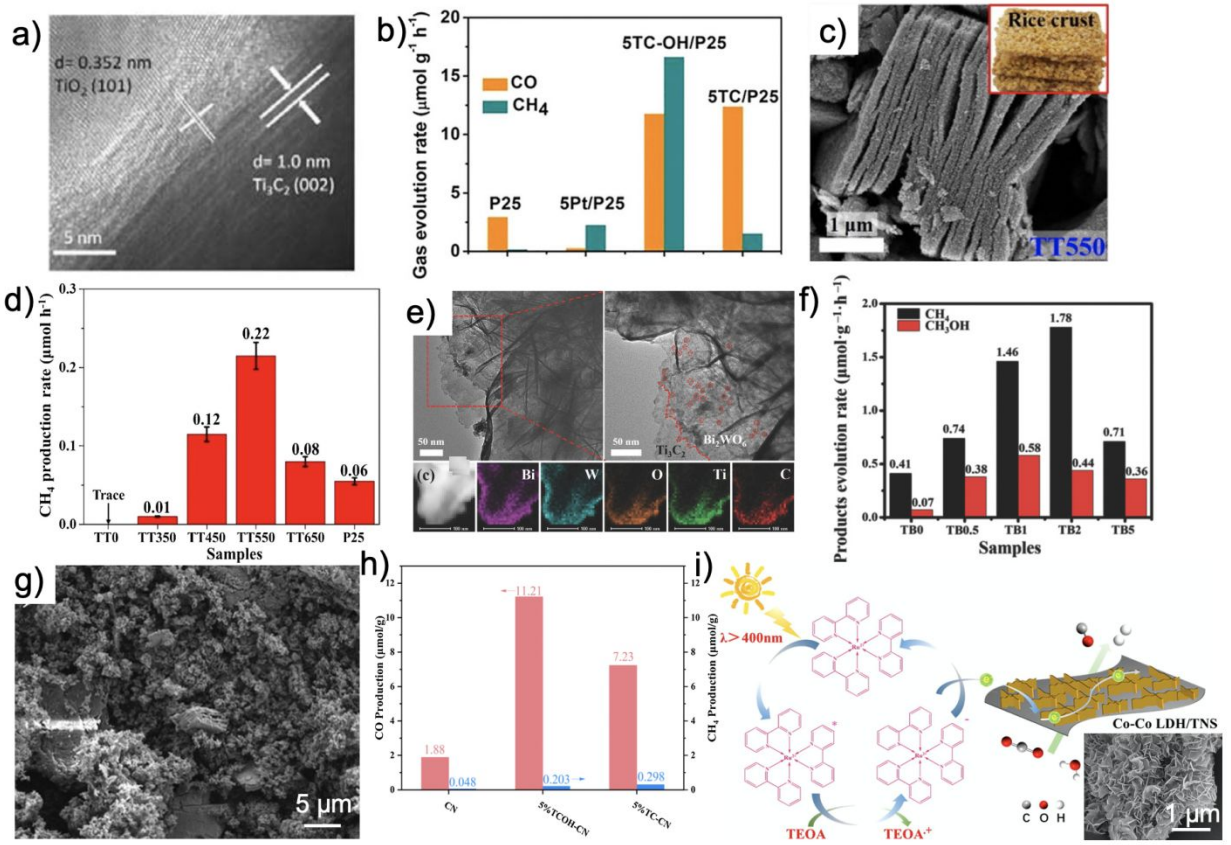

Fig. 19. a) HRTEM image of the interface structure of Ti_3C_2-OH and TiO_2 P25 NPs. b) Evolution rates of CO and CH_4 over P25, 5%Pt/P25(5Pt/P25, 5%Ti_3C_2/P25(5TC/P25), 5%Ti_3C_2-OH/P25(5TC-OH/P25) under irradiation by a 300 W Xe lamp; Reprinted with permission.[215] Copyright 2018 John Wiley and Sons. c) Field emission scanning electron microscope (FESEM) image of rice-crust like TiO_2/Ti_3C_2 composite. d) Comparison of the photocatalytic CO_2 reduction of the TiO_2/Ti_3C_2 composite samples without calcination and with calcination (TT350, TT450, TT550 and TT650 were defined as the TiO_2/Ti_3C_2 prepared under different calcination temperatures) and P25 for CH_4 production. Reprinted with permission.[216] Copyright 2018 Elsevier Inc. e) TEM image of 2% Ti_3C_2 in Ti_3C_2/Bi_2WO_6 and the element mappings of Bi, W, O, Ti, C of selected area. The red circles indicate the Bi particles derived from Bi_2WO_6 nanosheets under the high-power electron beam. f) Photocatalytic activity of TB0 to TB5, where TBX= Ti_3C_2/Bi_2WO_6 and X= the % of Ti_3C_2. Reprinted with permission.[217] Copyright 2018 John Wiley and Sons. g)

SEM image of 5% Ti_3C_2/g-C_3N_4 sample. h) 5 h accumulated production of CO and CH_4 on g-C_3N_4 (CN), 5% Ti_3C_2-CN (5%TC-CN), and 5% Ti_3C_2-OH-CN(5%TCOH-CN). Reprinted with permission.[218] Copyright 2020 Elsevier Inc. i) Co-Co layered double hydroxide/$Ti_3C_2T_X$ nanosheets (LDH/TNS) for CO_2 reduction with triethanolamine (TEOA) as sacrificial agent. Inset is the SEM image of the catalyst morphology. Reprinted with permission.[219] Copyright 2020 Elsevier Inc.

Since most MXenes exhibit metallic behavior, coupling MXenes to other photoactive materials is an important strategy for CO_2 photoreduction. For example, Ye and coworkers coupled TiO_2 nanoparticles (P25) to Ti_3C_2−OH MXenes for CO_2 photoreduction (Fig. 19a).[215] These MXene/TiO_2 heterostructures have superior electrical conductivity and charge-carrier separation ability as well as abundant CO_2 adsorption and activation sites, where the heterostructure activities for CO_2RR to generate CO (11.74 $\mu molg^{-1}h^{-1}$) and CH_4 (16.61 $\mu molg^{-1}h^{-1}$) were greater than that of bare P25 (Fig. 19b) and for P25 loaded with 5 wt % Pt (5Pt/P25). Annealing a Ti_3C_2 MXene precursor has also been used to produce TiO_2/Ti_3C_2 hybrids with a unique "rice-crust" like structure (Fig. 19c).[216] Efficient interfacial charge transfer enabled outstanding photocatalytic activity for CO_2 reduction to CH_4 with a rate of 0.22 $\mu mol\ h^{-1}$, 3.7-fold higher than a P25 TiO_2 control (Fig. 19d).

Cao *et al*. prepared ultrathin Ti_3C_2/Bi_2WO_6 nanosheets *via* hydrothermal methods (Fig. 19e).[217] The interface energetics of this heterostructure induced photoexcited electron transfer from Bi_2WO_6 nanosheets to metallic, O-terminated Ti_3C_2 and subsequent reduction of adsorbed CO_2. As shown in Fig. 19f, the optimized Ti_3C_2 loading of 2% in Ti_3C_2/Bi_2WO_6 (TB2) gave CH_4 and CH_3OH yields of 1.78 and 0.44 $\mu mol\ h^{-1}\ g^{-1}$, respectively, while significantly outperforming pristine Bi_2WO_6. Similarly, MXene fraction-dependent photocatalytic CO_2RR was also observed by Tang *et al*. for heterostructures between graphitic carbon nitride (g-C_3N_4) and Ti_3C_2-OH (Fig. 19g), with the optimal composite producing CO and CH_4 yields that were ~6x times and 4x higher than pure g-C_3N_4, respectively (Fig. 19h). [218] In addition, Liu *et al.* synthesized

the CeO_2@Ti_3C_2 composite, where a Schottky junction was realized by the built-in electric field between CeO_2 and MXene.[220] The best CO yield catalyzed by CeO_2@ Ti_3C_2 under visible illumination was 40.2 μmol m^{-2} h^{-1}, ~1.5x higher than pure CeO_2.

Another recent study demonstrated nanocomposites pairing Co-Co layered double hydroxides with $Ti_3C_2T_X$ for CO_2RR photocatalysis (Fig. 19i). The MXene enhanced conductivity and surface activity, which resulted in rapid electron transfer and adequate catalytic sites for the separation and utilization of electrons. It also exhibited good CO_2RR quantum efficiency (0.92% at 420 nm) and stability (5 cycles, 5 h/cycle) to produce CO. The CO generation yield was much higher than that of the pristine Co-Co photocatalyst, reaching 12,500 μmol g^{-1} h^{-1} under visible-light irradiation (>400 nm).[219]

Recent efforts have coupled $CsPbX_3$ perovskite nanocrystals to 2D MXenes due to the favorable bandgap, high carrier mobility, and long carrier lifetimes of perovskites. For example, Liu *et al.* found that $CsPbBr_3$@$Ti_3C_2T_x$ composites reduced CO_2 under simulated solar irradiation.[221] Ethyl acetate was used as the solvent for enhanced CO_2 solubility and $CsPbBr_3$ nanocrystal stability. The 1.5 eV conduction band offset drove electron transfer from photoexcited $CsPbBr_3$ to $Ti_3C_2T_x$, resulting in higher product yields compared to that of pure $CsPbBr_3$ and other $CsPbBr_3$-based heterostructures (*e.g.,* $CsPbBr_3$/GO, $CsPbBr_3$/g-C_3N_4, $CsPbBr_3$/TiO_2, $CsPbBr_3$/Zeolitic Imidazolate Framework). Only CO and CH_4 were detected with the yield of 26.32 and 7.25 μmol g^{-1} h^{-1}, respectively, with no H_2 being detected, indicating a highly selective CO_2 reduction.

Table 3. Summary of Experimental CO_2RR works by 2D MXene-based catalysts.

Materials	Electrolyte	Activity	Product	Reference
		Electrochemical Process		

Ti_2CT_x (KF-HCl etching)	CO_2 sparging, acetonitrile, water, and ($BEMIMBF_4$) electrolyte	$FE_{formic\ acid}$ = 56% (−1.73 V vs. SHE)	HCOOH,CO,CH_4	210
Mo_2CT_x (HF etching)	CO_2 sparging, acetonitrile, water, and ($BEMIMBF_4$) electrolyte	$FE_{formic\ acid}$ = 34% (−1.23 V vs. SHE)	HCOOH,CO,CH_4	210
Delaminated Mo_2C and Ti_3C_2	CO_2 saturated $EMIMBF_4$	FE_{CO} = 90% (−2.24 V vs. SCE,Mo_2C) FE_{CO} = 65% (−2.54 V vs. SCE, Ti_3C_2)	CO	213
		Photochemical Process		
P25/Ti_3C_2	CO_2 in de-ionized H_2O, Xe Lamp	11.74 μmol g^{-1} h^{-1} (CO) 16.61 μmol g^{-1} h^{-1}(CH_4)	CO,CH_4	215
TiO_2/Ti_3C_2	$NaHCO_3$ and HCl in H_2O, Xe Lamp	4.4 μmol g^{-1} h^{-1}	CH_4	216
Ti_3C_2/Bi_2WO_6 nanosheets	$NaHCO_3$ and H_2SO_4 in H_2O, Xe Lamp	1.78 μmol g^{-1} h^{-1} (CH_4) 0.44 μmol g^{-1} h^{-1}(CH_3OH)	CH_4,CH_3OH	217
Ti_3C_2/g-C_3N_4	CO_2 in H_2O, Xe Lamp	2.24 μmol g^{-1} h^{-1} (CO) 0.38 μmol g^{-1} h^{-1} (CH_4)	CO,CH_4	218
CeO_2/Ti_3C_2	$NaHCO_3$, HCl and H_2O vapor, Xe Lamp	40.2 μmol m^{-2} h^{-1}	CO	220
$CsPbBr_3$/ $Ti_3C_2T_x$	CO_2, ethyl acetate solvent, Xe Lamp (420 nm cut-off)	26.32 μmol $g^{-1}h^{-1}$ (CO) 7.25 μmol $g^{-1}h^{-1}$(CH_4)	CO,CH_4	221

4. N_2 Reduction Reactions

In this section, we review the performance of 2D TMDC and MXene materials used in electrochemical, photoelectrochemical, and photochemical NRR. To compare the available studies, we first discuss the NRR reaction mechanisms and underlying factors that influence each reaction before reviewing NRR results with 2D TMDC and MXene catalysts. Since these NRR occur *via* concerted PCET reactions, the mechanisms involved in these reduction reactions proceed similarly. Thus, in this section, we will introduce the pathways deciphered by DFT calculations that are

deemed the most probable. There are two basic associative reaction mechanisms that have been proposed for PCET NRR to NH_3: distal and alternating, which are distinct from the dissociative reaction mechanism that the Haber-Bosh process follows.[222]

4.1 NRR Mechanisms

The major challenges of employing NRR catalysts discussed in this review stem from a lack of selectivity and activity for (photo)electrochemical and photochemical processes. First the selective synthesis of ammonia from nitrogen has been plagued by the competition with HER, which occurs with far less kinetic barriers. Thus, there are no known reports of heterogeneous or homogeneous catalysts showing 100% Faradaic efficiencies or quantum yields for NRR to ammonia. To circumvent the selectivity issue arising from the competing binding of H^+ vs N_2, it is desirable to realize materials that preferentially bind N_2 over H^+. Although the reduction of N_2 to ammonia or NH_4^+ is thermodynamically favorable, the potential window between the HER and NRR is quite small across the entire pH scale (Fig. 20a).[223] For most electrocatalysts reported the applied potentials are more negative than 0 V vs. SHE (Fig. 20b),[224] where the potential window for NRR becomes even smaller. Second, sluggish NRR kinetics have translated to low yield rates for the reaction. The large energy (945 kJ mol^{-1} @ 298 K) required to break or weaken the inert triple bonds of N_2 molecules and the $6e^-/6H^+$ PCET steps to yield two NH_3 molecules slows down the reaction rates further. Third, the contamination of adventitious ammonia has been a clear problem for verifying the low yields observed in the experimental results presented. Most studies have yields of ammonia that are in the parts per billion concentrations (<10 μg mL^{-1}). Reports point to the presence of NH_3 or NH_4^+ contamination giving false results where the contamination could be from aqueous solutions, low purity gases, contaminated surfaces (latex gloves, lab coats,

and tubing), human breath, and Nafion membranes.[225-228] The possibility of catalyst decomposition has also been reported to produce ammonia.[229]

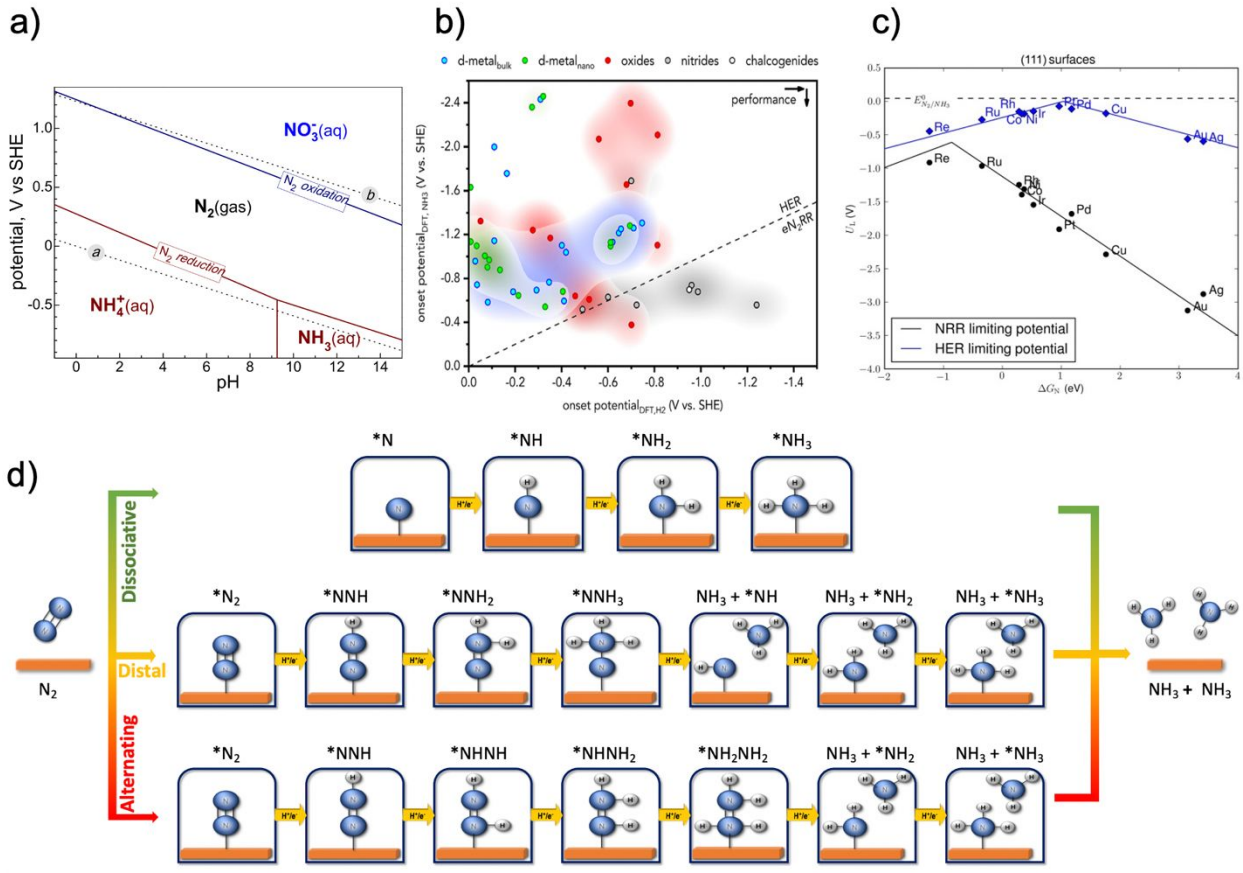

Fig. 20. a) Pourbaix diagram for the N_2/water system with dashed lines indicating the water oxidation (labeled (b) and water reduction (labeled (a)). Reprinted with permission.[223] Copyright 2018 American Association for the Advancement of Science (AAAS). b) Theoretical onset potentials for NRR and HER on different materials obtained through DFT calculations that are classified according to different families of materials. The materials that are favorable for the NRR are shown below the dashed line. Reprinted with permission.[224] Copyright 2019 Elsevier Inc. c) Volcano plots for the N binding energy on (111) surfaces of transition metals and the H binding energies versus calculated limiting potentials. Reprinted with permission.[209] Copyright 2010 John Wiley and Sons. d) Different reaction pathways on heterogenous/homogeneous catalysts for the NRR, the blue circles indicate N atoms, and the white circles indicate H atoms.

To address contamination issues, stringent protocols and control experiments are required for verifying ammonia yields in (photo)electrochemical and photochemical catalytic NRR results.[220, 228, 230] To rule out contamination of ammonia species from the catalyst or experimental setups, control experiments should be performed in an Ar gas atmosphere under identical conditions to

the NRR experiments. To rule out NH_3 contamination from the N_2 gas feed, running the experiments at open circuit potential has also been strongly encouraged. Moreover, to avoid other nitrogen containing species such as NO_x, running the N_2 gas through an absorbent such as copper has been suggested. [220, 225, 227, 228, 230] To confirm the origin of the NH_3, control experiments should employ isotopically labelled $^{15}N_2$, where ^{1}H-NMR can confirm the presence of $^{15}NH_3$, and quantitative analysis of $^{15}NH_3$ and $^{14}NH_3$ under identical conditions should provide similar concentrations of detected ammonia.[220, 230]

The 6 PCET steps for the (photo)electrochemical and photochemical NRR to NH_3 results in many intermediates and intermediate steps. Depending upon the minimum energy pathways, the reaction proceeds along a purely distal or alternating pathway, or the reaction can alternate between the two mechanisms. However, the basic mechanism of PCET remains unchanged. Skulason *et al.* first proposed a DFT model based on the associative NRR.[231] Since then other models have been explored and scaling relations predicted based on DFT calculations (Fig. 20c).[232, 233]

In these three basic pathways (Fig. 20d, many intermediates can be formed, such as N_2H_x or NH_x (where n = 0, 1, or 2), where hydrogenation occurs from H atoms adsorbed on the catalyst surface (Tafel type mechanism) or from protons in solution (Heyrovsky type mechanism). Skulason *et al.* have shown that the Tafel type mechanism has a large activation barrier for most transition metals, thus giving a relatively slow rate for NRR and suggesting that an associative or dissociative Heyrovsky-type reaction route is more likely.[231] For the dissociative pathway, the N_2 molecule dissociates on the catalyst surface and the adsorbed N atoms undergo PCET. The dissociative reaction mechanism is predicted for surfaces with exothermic N adsorption enthalpies.[231] Metals on the right hand side of the plot in Fig. 20c have weaker binding towards N atoms and are therefore predicted to follow an associative pathway (*e.g.,* Ru, Rh, Pt, Mo, Fe). The

adsorption of molecular nitrogen and the first protonation step to form $*N_2H$ is usually the potential limiting step for such metals. In these studies, the authors show that the adsorption free energy of the N adatoms scale linearly with the adsorption free energy of the N_2H_x intermediate species. [231, 232] Thus, volcano plots-based on the N adsorption free energy versus the calculated onset potential can be constructed to identify the most catalytically active metal surfaces (Fig. 20c). From the volcano plot constructed, it is clear none of the metals would have an ideal binding free energy. In aqueous solution, HER competes with NRR, and according to Montoya *et al.*, HER will always prevail over NRR on metal surfaces, which limits the selectivity for NRR.[232] Hence, the necessity arises to probe materials that are alloys, have defects, or contain compounds with hetero single-atoms[234] that can be tuned to break the scaling relations and selectively bind N_2 over H^+.

2D TMDCs and MXenes have been explored as potential catalysts for (photo)electrochemical and photochemical NRR. Zhang *et al.* performed DFT calculations on 2D MoS_2 to map out NRR pathways.[235] They identified that the most active site was the Mo edge (Fig. 21a), owing to the partial positive charge on undercoordinated Mo atoms. This partial positive charge polarizes the N_2 molecules to activate N_2 on the surface. They also showed that the NRR potential determining step to be PCET of the first hydrogenation (Fig. 21a) along a distal pathway. The DFT results indicated that the N–N bond length significantly increased upon adsorption and the first protonation step (*NNH), which implied that a charge transfer occurred between the adsorbed N_2 and the Mo-edge atoms, thus weakening the N_2 triple bond.[235] A similar distal mechanism has been predicted by X. Li *et al.* on defect rich MoS_2.[235] They showed that the bond lengths of the adsorbed N_2 significantly increase on defect sites, which lowers the barrier for the first protonation step (Fig. 21b).[235] In contrast to Zhang *et al.*'s findings, the potential determining step for MoS_2 defect sites

was the last PCET step (*NH_2 to *NH_3). Nevertheless, both studies revealed that the most favorable reaction pathway to be a Heyrovsky type distal pathway for 2D MoS_2.[235]

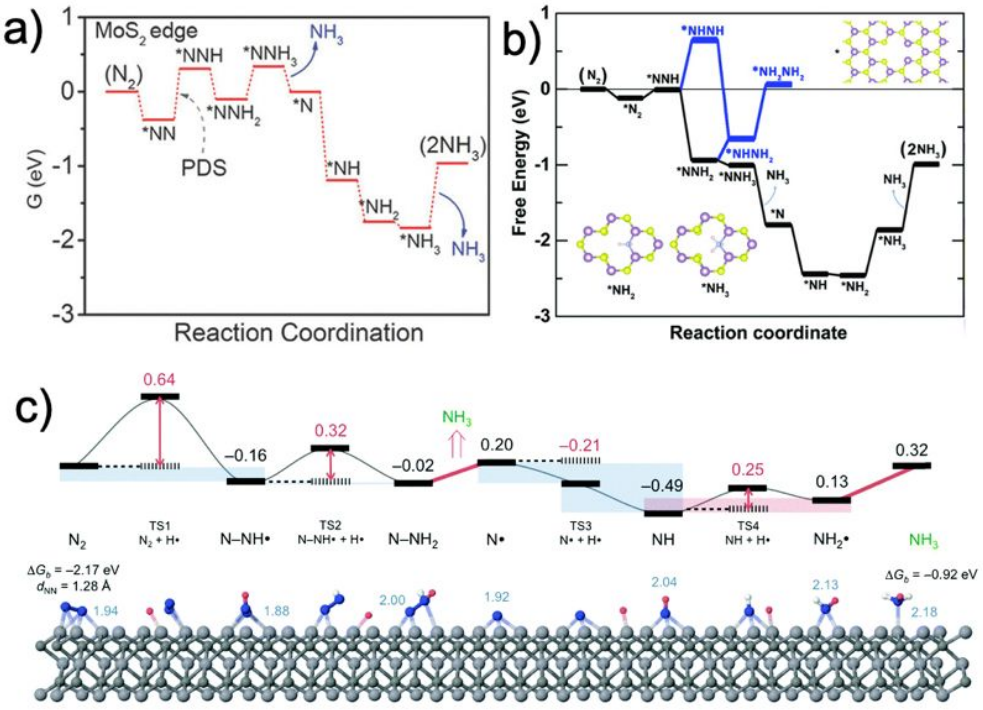

Fig. 21. a) Minimum energy pathway for NRR on edge sites of MoS_2, Reprinted with permission.[235] Copyright 2018 John Wiley and Sons. b) Vacancy sites of MoS_2 influence the minimum energy pathway. Reprinted with permission.[235] Copyright 2018 John Wiley and Sons. c) Minimum energy pathway for NRR on edge sites of V_3C_2 MXene. Schematic in panel c) shows bound reaction intermediates and N–N triple bond lengths (blue labels) for V_3C_2 reaction pathway. Reprinted with permission.[222] Copyright 2016 The Royal Society of Chemistry.

Li and coworkers systematically explored the 2H phases of MS_2 (M = Mo, W, V, Nb, Ti and Ta) using first principles calculations towards electrochemical NRR.[221] Similar to studies by X. Li *et al.* and Zhang *et al.*, F. Li *et al.* investigated zig-zag edges of the metal-terminated TMDCs as the most probable reaction sites.[221, 235] F. Li and coworkers initially probed the adsorption configuration of the N_2 molecules on the edge sites of the six TMDCs and showed that a bridge-on chemisorption is preferred over the end-on and side-on configurations. Comparing alternating and distal pathways, the authors showed that the distal pathway is more thermodynamically favorable. Thus, a comparison of the distal pathways on these TMDC systems showed that the

edge sites of VS_2 to have the most favorable NRR energetics, with catalytic activity of 2D nanoribbons following the trend: VS_2>NbS_2>TiS_2>MoS_2>WS_2>TaS_2.[221]

Fewer theoretical reports exist for MXenes and NRR; however, there are similarities with the 2D TMDCs, such as favoring Heyrovsky type distal mechanisms. Azofra and coworkers evaluated metal carbide MXenes for N_2 capture and conversion to NH_3 using DFT.[222] They looked at pristine MXene surfaces—without surface termination groups—to reveal that M_3C_2 MXenes, such as V_3C_2 and Nb_3C_2, exhibited promising results for NRR (Fig. 21c). They showed that N_2 adsorption free energy is exergonic (thus spontaneous) on MXenes having d^2, d^3, and d^4 configurations on the transition metals, such as Ti, V, and Mo, respectively. Due to the strong adsorption energy, the N–N bonds are activated, making the first hydrogenation step (*N–N to N–NH) more feasible. The minimum energy pathway observed in these DFT studies was the Heyrovsky type distal pathway, with the potential determining step being the last hydrogenation step (NH_2 to $*NH_3$). Zhao *et al.* made similar observations for $Ti_3C_2T_x$ MXene, T_x = F or OH,[236] where the surface functional groups did not change the mechanism outlined by Azofra and coworkers.[222] Side-on adsorption of the N_2 molecule was slightly preferred over the end-on adsorption (Fig. 21c).[236] Since thermodynamics simulations typically assume only a small kinetic contribution to the activation barrier for electrochemical reactions, this assumption can lead to contradictions with both experimental results and kinetics studies. Recent simulation advances for electrocatalytic processes attempt to accurately capture these kinetic contributions,[237, 238] and would be more realistic for better understanding 2D TMDC and MXene catalysts.

4.2 2D TMDCs

4.2.1 Electrochemical and Photoelectrochemical NRR

Undercoordinated sites of 2D MoS_2 have primarily been shown to be active towards electrochemical NRR. Edge and vacant sites on 2H-MoS_2 and phase-engineered MoS_2 polarize the adsorbed N_2 atoms, a necessary but insufficient parameter.[221, 235, 239] N_2 polarization is identified as a key step to activate N_2 for NRR, without which a large energy penalty (1 – 1.5 eV for metal surfaces) exists for the first PCET step.[235] As a proof of concept, Zhang *et al.* synthesized MoS_2 on a carbon cloth support (Fig. 22a) for NRR.[235] The MoS_2 catalyst achieved 1.7% FE and an ammonia yield of $2.8x10^{-11}$ mol s^{-1} cm^{-2} at an applied potential of -0.5 V vs. RHE (Fig. 22b). As discussed in the previous section, DFT calculations on this system suggested that the partial positive charge on the Mo edge atoms were catalytically active towards NRR (Fig. 21a).[235] 2D MoS_2 defect sites have also resulted in enhanced NRR activity. Li *et al.* investigated the influence of defects on NRR for hydrothermally synthesized MoS_2 nanoflowers,[240] where defects were introduced by changing the sulfur source and reactant molar ratios. Defect-rich MoS_2 outperformed defect-poor MoS_2 nanoflowers for NRR (Fig. 22c). The optimized defect rich-catalyst had a FE of 8.34% and a yield rate of 29.28 μg h^{-1} mg^{-1} at -0.40 V vs. RHE, while the defect poor catalyst had a FE of 2.18% and 13.41 μg h^{-1} mg^{-1} ammonia yield rate (Fig. 22d). First principles calculations suggested that nitrogen adsorption and activation occurred at the rim sites of sulfur vacancies. The distal pathway was favored over the alternating pathway, and the potential-determining step was identified as the conversion of $*NH_2$ to $*NH_3$.[240]

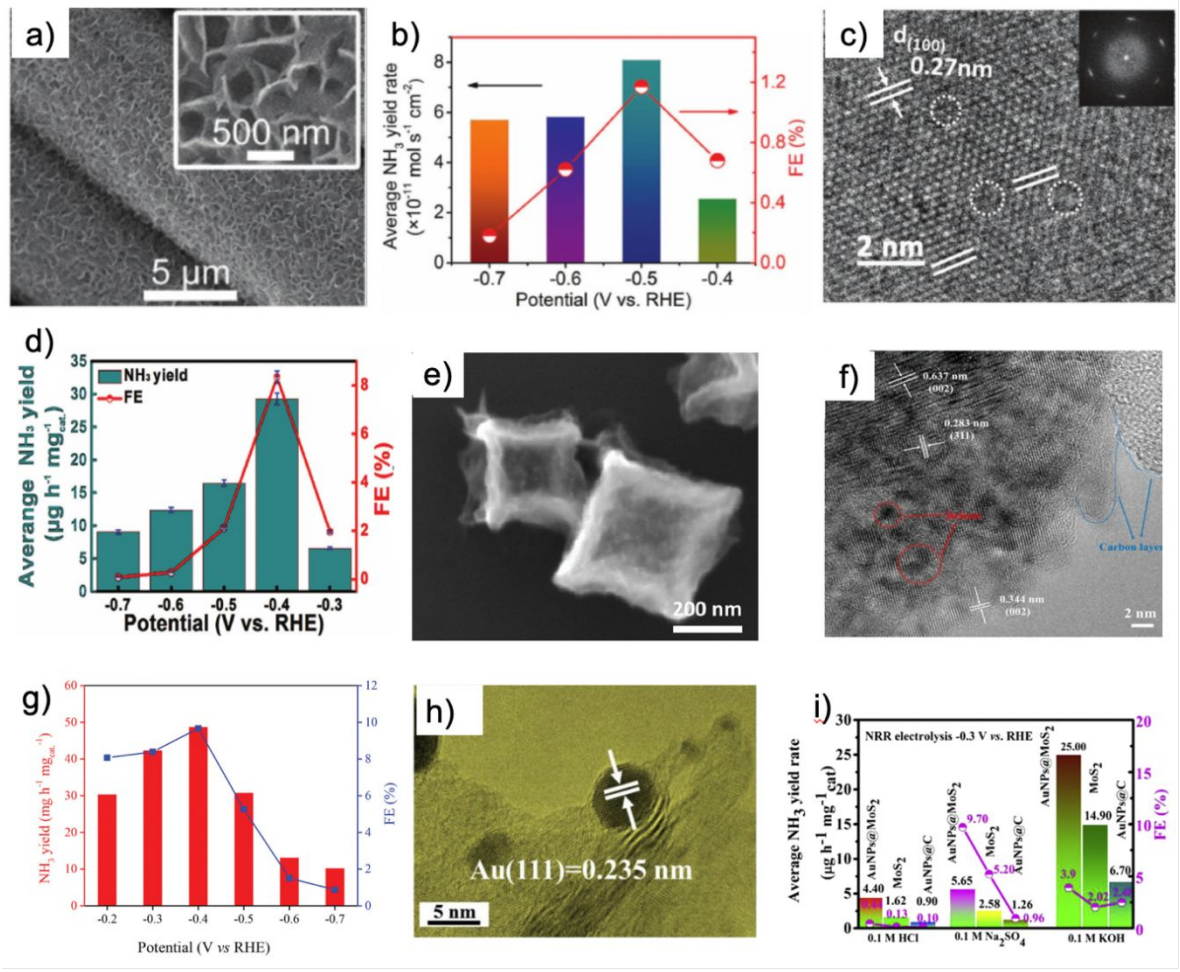

Fig. 22. a) SEM images of MoS_2 on a carbon cloth. b) Ammonia yield rate and FE for the NRR to ammonia from MoS_2 on carbon cloth. Reprinted with permission.[235] Copyright 2018 John Wiley and Sons. c) HRTEM of basal plane (100) of defect rich MoS_2 showing dislocations and distortions, and d) average yield and Faradaic efficiency of ammonia production at different applied potentials. Reprinted with permission.[240] Copyright 2018 John Wiley and Sons. e) SEM image of Co-MoS_2 for (20:1) of Co:Mo, f) HRTEM image showing the carbon support and the Co-MoS_2 and g) plot of ammonia production rate for Co-MoS_2 at various potentials vs. RHE. Reprinted with permission.[241] Copyright 2020 The Royal Society of Chemistry. h) TEM image of Au incorporated MoS_2 showing the (111) facet of Au. i) Comparison of the yield rate and the FE of AuNP@MoS_2 with MoS_2 and AuNP@C in different electrolytes. Reprinted with permission.[242] Copyright 2019 Elsevier Inc.

Incorporating transition metals into 2H MoS_2 structures has been evaluated as a strategy to improve NRR. Zeng *et al*. synthesized 3D hollow nanostructures of MoS_2 incorporated with cobalt, and nickel-iron (NiFe) in two separate studies.[241] With Co-MoS_2 NCs (Fig. 22e and 22f), Zeng *et al.* achieved an NH_3 yield rate of 129.93 μg h^{-1} mg^{-1} with a FE of 11.21% at -0.4 V vs. RHE (Fig. 22g). The unique cube-like structure of Co-MoS_2 allowed more accessibility to active sites, and

the cell design promoted mass transfer of N_2 molecules, which contributed to the improved catalyst performance. Moreover, interfacing Co-MoS_2 with nitrogenated (pyrrolic, pyridinic, graphitic and oxidized) amorphous carbon increased charge transfer (lowering charge transfer resistance) and performance.[241] NiFe-incorporated MoS_2 nano cubes showed similar activity for NRR, with NH_3 production rate of 128.17 μg h^{-1} mg^{-1} and FE of 11.34% at -0.3 V.[243] DFT calculations revealed that the extensive surface area and unsaturated NiFe sites act as centers for adsorbing and activating N_2 molecules. Using evidence from in-situ electrochemical FTIR and DFT calculations, an alternating associative pathway was suggested for the NiFe-MoS_2 catalyst.[243]

Other groups have evaluated 2D MoS_2 incorporated with transition metals for NRR with the goal of reducing HER. Zhou *et al.* investigated NRR on MoS_2 nanosheets interfaced with gold (Au) particles (AuNPs@MoS_2) at varying pH (Fig. 22h).[242] MoS_2 nanosheets prepared under hydrothermal conditions were reacted with $HAuCl_4$ (gold source) and $C_6H_5Na_3O_7$•$2H_2O$ (reducing agent) to produce AuNPs@MoS_2. The highest FE of 9.7% was observed for neutral pH (0.1 M Na_2SO_4) at -0.3 V vs. RHE with a modest ammonia yield rate of 5.65μg h^{-1} mg^{-1} (Fig. 22i). However, the ammonia yield rate was greatest when electrocatalysis occurred under basic (0.1 M KOH) conditions: 25 μg h^{-1} mg^{-1} at -0.3 V vs. RHE, but with a much lower FE: 3.9%. Under both acidic and basic conditions, the FE suffers due to competition with HER.[242]

Suryanto and coworkers synthesized Ru-decorated MoS_2 for selective NRR.[244] They hypothesized that the MoS_2 phase (*i.e.,* 1T or 2H) controls the extent of parasitic HER. To make the various phases, lithiated MoS_2 (Li_xMoS_2) was reacted with a Ru precursor at 80 °C for 72 h to obtain the 1T phase, and the 2H phase was obtained by hydrothermal treatment of Ru/1T-MoS_2 at 150 °C for 12 h. Comparison of the HER and NRR activities showed that pure 2H MoS_2 and Ru/2H-MoS_2 were better for NRR than pure 1T MoS_2 and Ru/1T-MoS_2. Ru/2H-MoS_2 was the best

NRR catalyst in the series, with ammonia yield rate of 6.98 μg $h^{-1}mg^{-1}$ and a FE of 17.6% at 50 °C and -0.15 V vs. RHE. Notably, a dissociative reaction mechanism for NH_3 formation was predicted by DFT calculations for these Ru based system.[244]

1T-MoS_2 offers higher conductivity of electrons and more active basal plane sites than the semiconducting phase, but few reports have studied 1T-MoS_2 for NRR. Patil and coworkers explored the electrochemical NRR activity of 1T-MoS_2 grown on a Ni foil (Fig. 23a), employing $LiClO_4$ as the electrolyte.[245] In the presence of the Li, the 1T-MoS_2-Ni showed a FE of 27.66% at -0.3 V vs. RHE (Fig. 23b), yielding NH_3 at a rate of 1.05 μg min^{-1} cm^{-2} (63 μg h^{-1} cm^{-2}). DFT calculations on this system predicted that a pseudo-six-membered ring with N_2 (Fig. 23c) forms in the presence of Li^+. This pseudo-ring formation reduced the energy barrier towards NRR and was also believed to suppress HER through the formation of strong Li-S interactions. Comparison of the adsorption free energies of NRR intermediates for the 1T phase, the 2H phase, and the 1T phase in the presence of Li^+, suggested the most favorable pathway to be the 1T phase in the presence of Li^+ (Fig. 23d).[245]

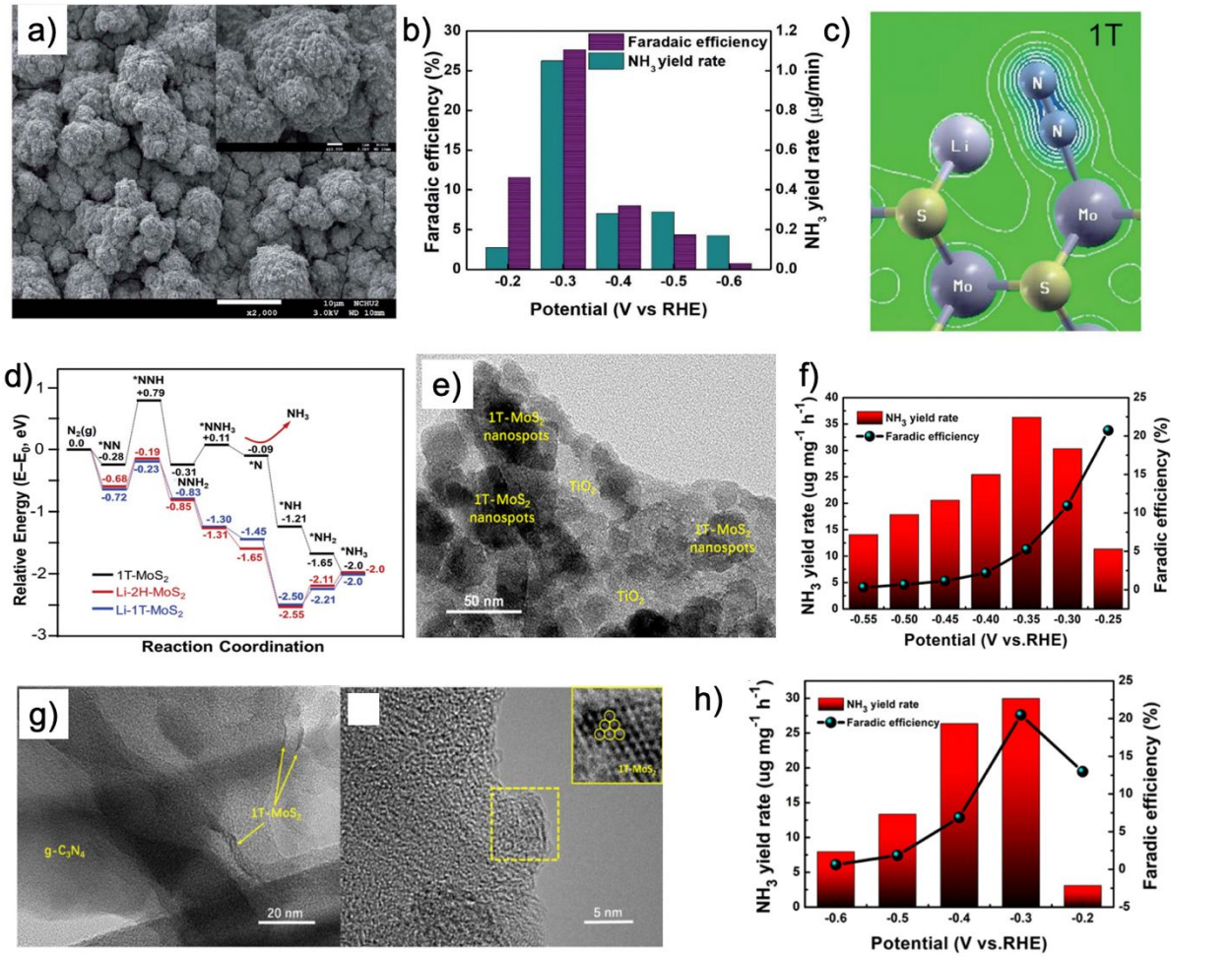

Fig. 23. a) SEM image of 1T MoS_2 on Ni foil and b) plot of NH_3 yield rate and FE at different potentials vs. RHE in 0.25 M $LiClO_4$ electrolyte. c) Representative electron contour map of adsorbed N_2 intermediate on a Mo atom of Li-MoS_2, and d) energy landscape of different MoS_2 catalysts. Reprinted with permission.[245] Copyright 2021 The Royal Society of Chemistry. e) TEM images of 1T-MoS_2 heterostructure on $Ti_3C_2T_x$ MXene. f) Ammonia yield rate and Faradaic efficiency of 1T-MoS_2 grown on Ti_3C_2 MXene. Reprinted with permission.[13] Copyright 2020 American Chemical Society. g) TEM image of 1T-MoS_2 on g-C_3N_4, and h) ammonia production rate and Faradaic efficiency for 1T-MoS_2 on g-C_3N_4. Reprinted with permission.[239] Copyright 2020 Elsevier Inc.

In addition to 1T MoS_2 nanostructures, 1T MoS_2 heterostructures have been reported for NRR. Xu *et al.* grew 1T MoS_2 nanoparticles on exfoliated $Ti_3C_2T_x$ using a hydrothermal method (Fig. 23e).[13] The optimized NRR results had an NH_3 yield rate of 36.28 μg h^{-1} mg^{-1} at -0.35 V vs. RHE with a FE of 5.26%. FE increased at lower applied voltages, albeit at the expense of lower ammonia production rates (Fig. 23f). In a separate study, Xu *et al*. constructed 1T-MoS_2 nanodot (ND) catalysts anchored on g-C_3N_4 (Fig. 23g), where the 1T-MoS_2 was obtained *via* a hydrothermal

reaction and interfaced with the g-C_3N_4 *via* ultrasonic mixing.[239] Optimized N_2 electrolysis had an NH_3 yield rate of 29.97 μg h^{-1} mg^{-1} at -0.3 V, with a FE of 20.48% (Fig. 23h). At higher applied potentials the rate decreased significantly to 7.9 μg h^{-1} mg^{-1} and the FE dropped to 0.62%. This large drop in FE was attributed to increased competition with HER.[239] DFT calculations performed to explore the NRR mechanism on the 1T-MoS_2 NDs indicated favorable N_2 adsorption. The alternating pathway was found to be more favorable (*NNH to *NHNH), where the potential determining step was the fourth PCET step (*$NHNH_2$ to *NH_2 + NH_3).[239] In analyzing the results presented in Table 4, the 1T-MoS_2 catalysts does not show a clear advantage in comparison to the 2H phase. With an increase in both conductivity and active sites one would expect a higher yield rate on these 1T materials. Nonetheless, the increase in conductivity and the active basal plane sites provide more sites for the parasitic HER, which could in turn reduce the sites available for N binding and NRR.

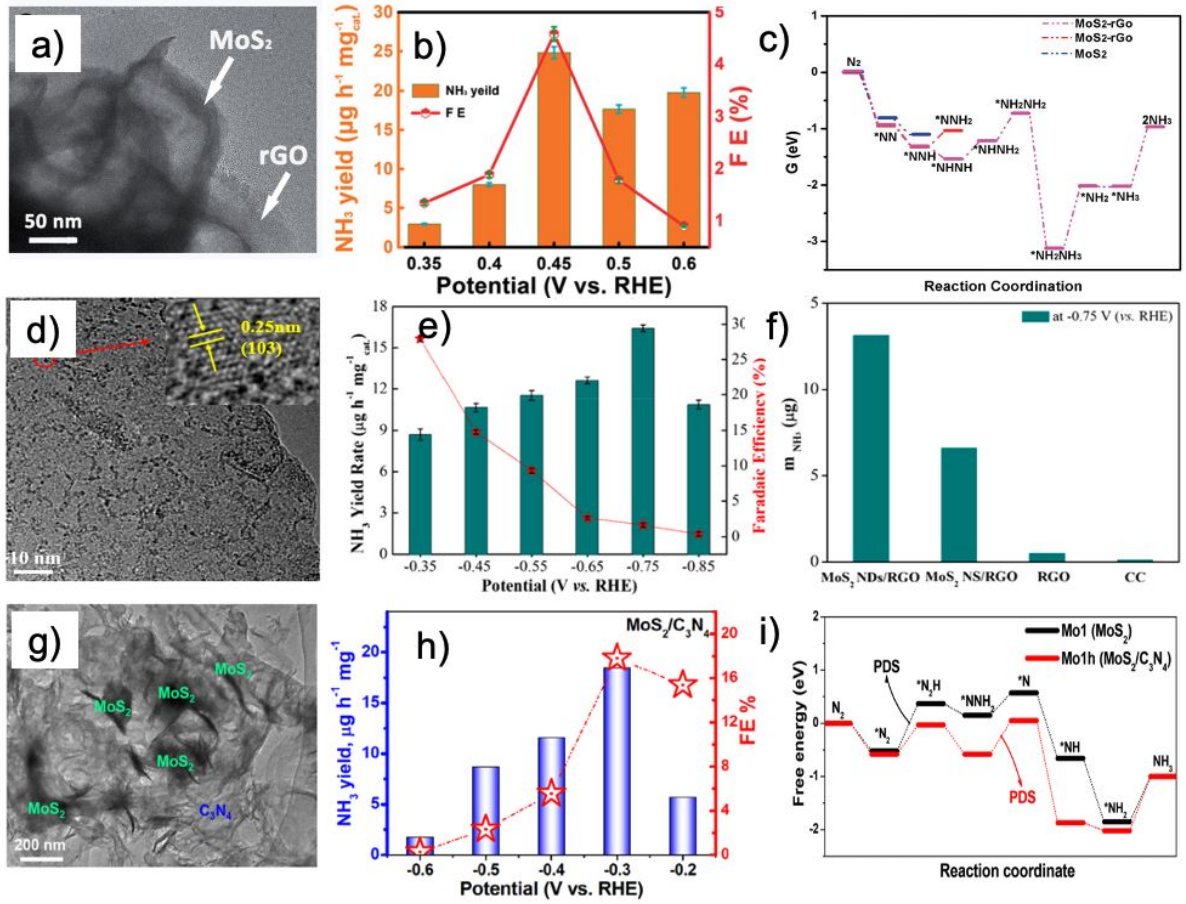

Fig. 24. a) TEM image of MoS_2 heterostructure grown on rGO, b) the yield and FE% for ammonia generation on MoS_2/rGO, and c) comparison of the free energy pathways for MoS_2 edge sites with and without the rGO. Reprinted with permission.[246] Copyright 2019 The Royal Society of Chemistry. d) TEM showing MoS_2 nanodots anchored on a rGO (MoS_2 NDs/rGO) support, e) ammonia yield rates and FE% for the MoS_2 NDs/rGO heterostructure, and f) comparison of the yields of ammonia at -0.75 V vs. RHE for MoS_2 catalyst with and without the rGO support. Reprinted with permission.[247] Copyright 2020 American Chemical Society. g) TEM image for MoS_2 catalyst on graphitic C_3N_4 support (MoS_2/C_3N_4), h) the yield and FE% for ammonia generation for the corresponding catalyst, and i) free energy diagram of the distal pathway for NRR on Mo edge sites of MoS_2 in the presence (Mo1h) and absence of the graphitic C_3N_4 (Mo1). Reprinted with permission.[248] Copyright 2020 American Chemical Society.

Heterostructures of C-based materials, such as reduced graphene oxide and g-C_3N_4, with 2H MoS_2 also generate NH_3. Li *et. al.* found that a reduced graphene oxide (rGO)/MoS_2 (Fig. 24a) heterostructure generated an ammonia yield rate of 24.82 μg $h^{-1}mg^{-1}$ and FE of 4.56% at -0.45 V vs. RHE (Fig. 24b).[246] DFT calculations predicted that the PCET step $^*NH_2NH_2$ to $^*NH_2NH_3$ is the potential-determining step (Fig. 24c).[246] Liu Y. *et al.* studied MoS_2 nanodots anchored on rGO (Fig. 24d) as catalysts and achieved an NH_3 yield rate of 16.41 μg $h^{-1}mg^{-1}$ with a FE of 27.9% at -

0.75 V vs. RHE (Fig. 24e).[247] The authors note that strong bridging between the C-S-C bridging bonds enhanced electron transfer, thus improving electrocatalytic NRR on this hybrid structure (Fig. 24f).[247] A study by Chu and coworkers found that 2D/2D MoS_2/g-C_3N_4 heterostructures (Fig. 24g) produced NH_3 at a yield rate of 18.5 μg h^{-1} mg^{-1} and 17.8% FE at -0.3 V vs. RHE (Fig. 24h).[248] DFT calculations revealed that interfacial charge transfer from g-C_3N_4 to MoS_2 stabilized a key intermediate $^*NH_2$ on Mo edge sites, concurrently decreasing the reaction energy barrier in the consequent step (Fig. 24i). Moreover, their DFT results showed that S edge sites favorably bind H atoms, thereby protecting the Mo edge sites that are active for NRR.[248] In another study of a MoS_2/g-C_3N_4 heterostructure catalyst,[249] Zhao *et al.* found an NH_3 yield rate of 19.86 μg h^{-1} mg^{-1} and 6.87% FE at -0.5 V vs. RHE. The authors suggested that interfacial Mo-N coordination and associated charge redistribution aided N adsorption and activation.[249]

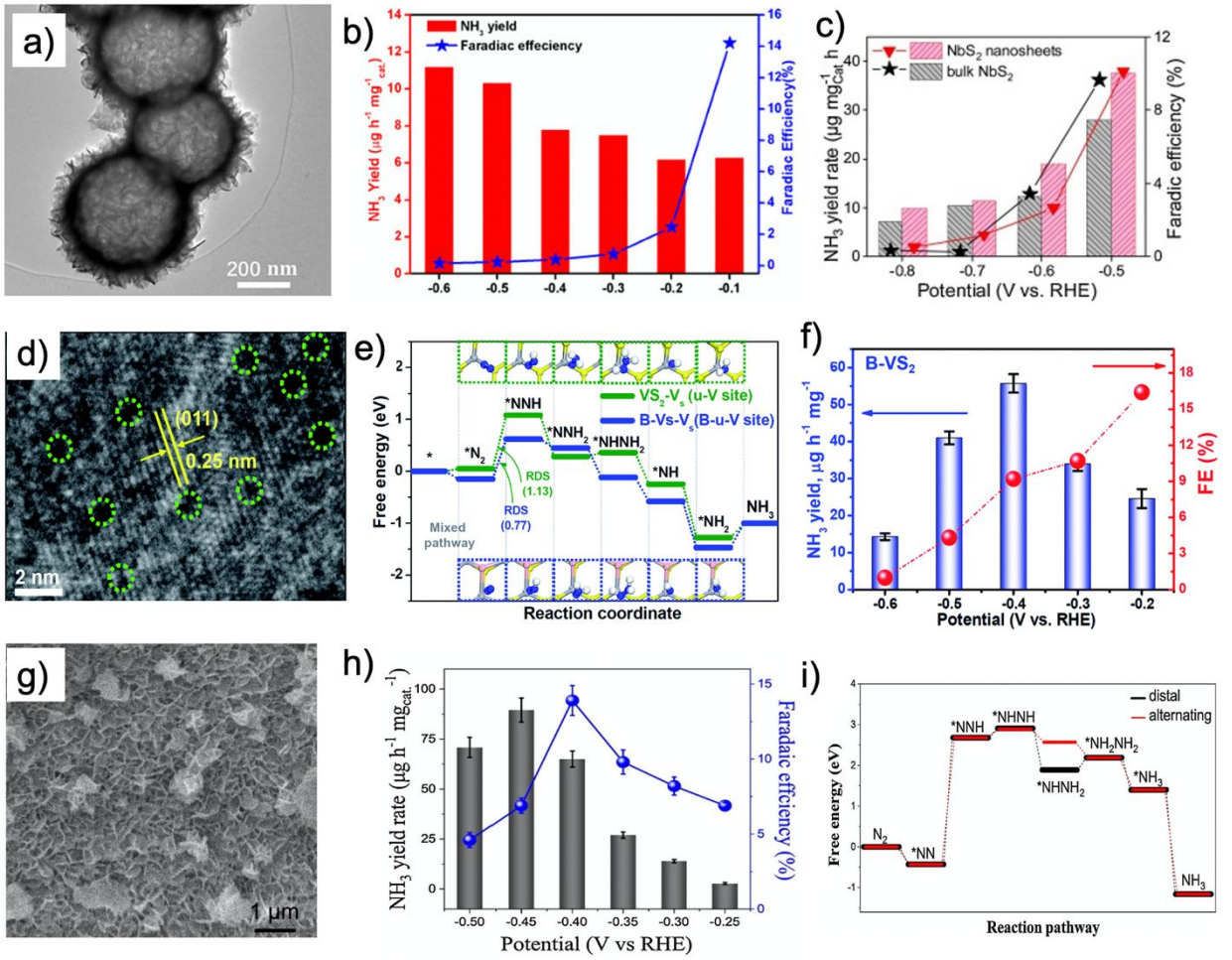

Fig. 25. a) TEM image of hollow $MoSe_2$ (H-$MoSe_2$) with a flower like morphology, and b) the yield and FE% for ammonia generation on (H-$MoSe_2$) in 0.1 M $LiClO_4$. Reprinted with permission.[250] Copyright 2020 American Chemical Society. c) Comparison of the NH_3 yield rates and FE% of exfoliated and bulk NbS_2 catalysts for the NRR. Reprinted with permission.[251] Copyright 2020 Elsevier Inc. d) HRTEM of boron doped VS_2 with sulfur vacancies circled, e) comparison of free energy pathways for NRR on VS_2 with S vacancies (VS_2-V_s), and boron doped VS_2 with S vacancies (B-Vs-VS_2) along a mixed pathway, and f) NH_3 yield rates and FE% for B-VS_2 in a $LiClO_4$ electrolyte. Reprinted with permission.[252] Copyright 2020 Royal Society of Chemistry. g) SEM images of self-supported $NbSe_2$ nanosheet arrays ($NbSe_2$ NSA) on a Ni foam, h) FE and yield rate plot for $NbSe_2$ NSA in a Na_2SO_4 electrolyte, and i) free energy pathways (distal and alternating) for NRR on $NbSe_2$ catalyst. Reprinted with permission.[253] Copyright 2020 Elsevier Inc.

Most of the TMDCs employed for electrochemical NRR are MoS_2 based. There are a few reports of $MoSe_2$ based catalysts, and we did not find any NRR studies on $MoTe_2$ being employed as catalysts for the electrochemical NRR. Yang *et al.* employed a hydrothermal technique to

synthesize hollow $MoSe_2$ (H-$MoSe_2$) for NRR (Fig. 25a).[250] The study reports a FE of 14.2% at -0.1 V, and the highest yield rate reported was 11.2 μg h^{-1} mg^{-1} at an applied voltage of -0.6 V vs. RHE. The FE was low (0.2%) at -0.6 V, which the authors claim to be the NRR threshold voltage (Fig. 25b). DFT calculations were used to identify the probable reaction pathways and revealed that H-$MoSe_2$ edge sites were the probable reaction sites. The calculations also show that the alternating path is preferred over the distal, with the rate-determining step being the protonation of *$NHNH_2$ to *NH_2NH_2.[250]

Wu *et al.* studied multiphasic (1T/2H) $MoSe_2$ for electrochemical NRR.[254] 1T@2H $MoSe_2$ was synthesized using a hydrothermal technique that formed aggregates of sheets, and the ammonia yield rate reached 19.91 μg h^{-1} mg^{-1} at an applied potential of -0.6 V vs. RHE. The authors also examined different solvents (0.1 M KOH, 0.1 M $LiClO_4$, and 0.1 M HCl), where the highest ammonia FE and yield rates were in neutral solvents $LiClO_4$ and Na_2SO_4. For all solvents the highest FE was observed at -0.5 V vs. RHE and the highest yield rate occurred at -0.6 V vs. RHE. The decrease of the FE at higher potentials was attributed to increased HER.[254] Since the results from these $MoSe_2$ studies are on par with the FEs and yield rates of MoS_2 catalysts, it is not yet clear if changing the chalcogen atom can lead to considerable differences in NRR.

Studies have also explored different transition metals in TMDCs other than Mo. DFT studies performed by Li and coworkers, described earlier in this chapter, predicted that among six transition metal sulfides (V, Nb, Ti, Mo, W and Ta) the activity for the NRR to follow VS_2>NbS_2>TiS_2>MoS_2>WS_2>TaS_2.[221] Among the series of 2D TMDCs studied, independent studies led by various groups have explored V, Nb, Mo, and Ti disulfides (Table 4) for

electrochemical NRR, and we did not find NRR studies on W or Ta disulfides. [251, 255] Interestingly, the disulfides of vanadium and niobium show superior ammonia yield rates to most of the molybdenum disulfide-based catalysts. Wang et al. synthesized NbS_2 nanosheets via a liquid exfoliation method using N-Methyl-2-pyrrolidone (NMP) and reported a maximum NRR FE of 10.12% and a NH_3 yield rate of 37.58 μg h^{-1} mg^{-1} (-0.5 V vs. RHE in 0.1 M HCl electrolyte, Fig. 25c).[251] Li *et al.* investigated VS_2 as a potential NRR catalyst by activating the basal plane using a synergistic effect of creating S vacancies and boron doping (Fig. 25d).[252] The results indicate a relatively high yield rate for NH_3 generation (55.7 μg h^{-1} mg^{-1} at -0.4 V) in a $LiClO_4$ electrolyte. The highest FE of 16.4% was recorded at -0.2 V vs. RHE (Fig. 25e). In comparison to pure VS_2, which produced NH_3 at a rate of ~18 μg h^{-1} mg^{-1}, the B doping and sulfur vacancies improved the activity at least three-fold. DFT calculations on the basal plane of VS_2 did not show favorable binding towards nitrogen, nevertheless the sulfur vacancy sites on the basal plane showed sufficient binding of N_2 molecules in an end-on orientation. Relative to VS_2 with S vacancies, B-doped VS_2 showed stronger binding of N_2; moreover, the binding free energy for H (ΔG_H) becomes > 0 eV, implying a lower binding for H and preferential binding of N_2 over H.[252] The electron deficient site due to boron doping creates a partial positive charge on the site, which has been shown to enhanceN_2 activation.[235, 252] More importantly, the potential-determining step (*N_2 to *NNH) has a lower reaction barrier on the B doped surface, thus improving NRR catalytic activity (Fig 25f). Jia *et al.* probed the catalytic activity of TiS_2 nanosheets (TiS_2 NSs) in electrochemical NRR, where electrolysis of N_2 in 0.1 M Na_2SO_4 for 2 h produced ammonia at a yield rate of 16.02

μg h^{-1} mg^{-1} at -0.6 V with a FE of 5.50%.[255] Overall, it is not possible at this time to provide a direct comparison of each system due to the use of various experimental conditions and fabrication techniques of the catalysts and electrodes. Nevertheless, theory-led predictions on TMDCs can be utilized to identify reaction sites and improve the catalytic activity of TMDC based electrocatalysts for NRR.

Wang et al. has reported the use of a self-supported $NbSe_2$ nanosheet array ($NbSe_2$-NSA) on a Ni foam as a NRR catalyst (Fig. 25g).[253] The use of the Ni foam led to a 3D nanoarchitecture that increased the exposure of active $NbSe_2$ active sites and reduced mass diffusion limitations. The catalyst achieved a highest FE of 13.9% at -0.4 V vs. RHE and a highest yield rate of 89.5 μg h^{-1} mg^{-1} at -0.45 V vs. RHE in a Na_2SO_4 electrolyte (Fig. 25h). DFT calculations revealed that Nb edge sites favorably bind nitrogen molecules and activate the N_2 molecule for NRR (Fig. 25i). Charge transfer from Nb atoms helps in the activation of the N-N triple bond. The calculations also revealed that the most favorable pathway for the reaction is the alternating pathway, owing to the potential determining step of the first hydrogenation step (*NN_2 to *NNH).

In addition to electrochemical nitrogen reduction, 2H MoS_2 has also been successfully interfaced with TiO_2 to form ammonia in photoelectrochemical studies. Ye *et al.* proposed NRR on a MoS_2/TiO_2 heterostructure catalyst [256] The authors show coupling to MoS_2 reduces the optical band gap of TiO_2 from 3.15 eV to 2.98 eV, allowing the catalyst to utilize a wider range of the solar spectrum (Fig. 26a). The transient photocurrent response is shown in Fig. 26b. The presence of the heterostructure provided good charge separation (electrons and holes) minimizing charge recombination. The catalyst recorded a yield rate of 1.42 μmol h^{-1} cm^{-2} with FE of 65.52% at -0.2

V vs. RHE (100 mW cm^{-2}, AM 1.5 G) (Fig. 26c**)**. In this heterostructure, MoS_2 accepts photogenerated electrons from TiO_2 and acts as NRR cocatalyst (Fig. 26a).[256]

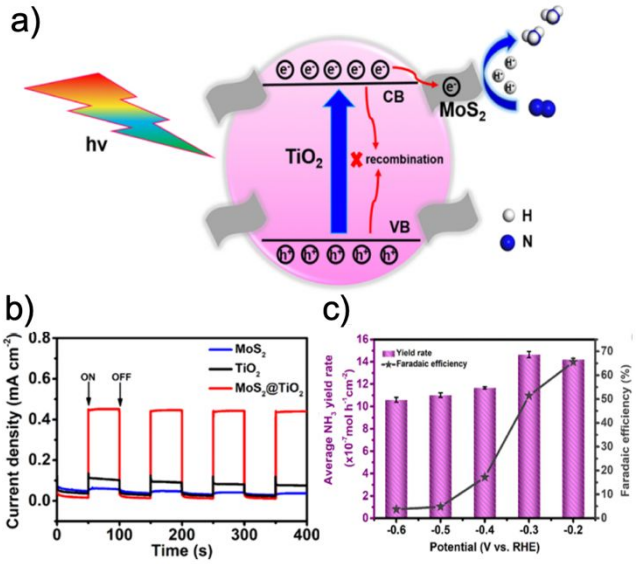

Fig. 26. a) Schematic of the N_2 reduction mechanism on MoS_2@TiO_2 under PEC conditions. b) Transient photocurrent response for the MoS_2@TiO_2 (100 mWcm^{-2}, AM 1.5 G) with repeated ON-OFF cycles and c) ammonia yield rates under PEC. Reprinted with permission.[256] Copyright 2019 American Chemical Society.

4.2.2 Photochemical NRR

The use of TMDCs as NRR photochemical catalysts has only been reported in a few studies. Although most of these photochemical studies have focused on TMDCs coupled to metal cocatalysts or heterostructures, one report used ultrathin MoS_2 alone in photocatalytic NRR.[114] Ultrathin MoS_2 sheets were obtained by sonication of hydrothermally synthesized MoS_2 bulk particles. The authors suggest that photogenerated excitons (electron-hole pairs) and negative trions (two electrons and a hole) allow multiple electrons to transfer to nitrogen adsorbed at S vacancies (Fig. 27a). These multi-electron transfers reduce the number of intermediates towards NH_3 production, thus reducing the kinetic and the thermodynamic barriers associated with multiple intermediates. The authors show that a simultaneous six-electron reduction on these ultrathin

sheets of MoS_2 yields ammonia at a rate of 325 μmol g^{-1} h^{-1} (5.525 μg h^{-1} mg^{-1}) (Fig. 27b) using a 500 W Xenon lamp as the illumination source.[114]

Most 2D MoS_2 photocatalysts require a metal cocatalyst or heterostructure to undergo N_2 photoreduction to generate NH_3. Zhu and coworkers synthesized a Pt loaded, N-doped MoS_2 (Pt/N-MoS_2) (Fig. 27c) microsphere for nitrogen fixation.[257] In this study, the authors showed that Pt/N-MoS_2 microspheres generate NH_3 at a yield rate of 121.2 μmol g^{-1} h^{-1} (300 W Xenon lamp), and the NH_3 yield rate was improved by performing photochemical NRR under ultrasonication (sonophotofixation): 133.8 μmol g^{-1} h^{-1} (2.275 μg h^{-1} mg^{-1}) (Fig. 27d). N doping is believed to introduce an impurity energy level above the VBM of MoS_2, which reduces the band gap (Fig. 27c). The presence of the Pt nanoparticles creates a Schottky barrier, such that conduction band electrons become centralized on surface Pt and have a higher chance of reducing N_2.[257]

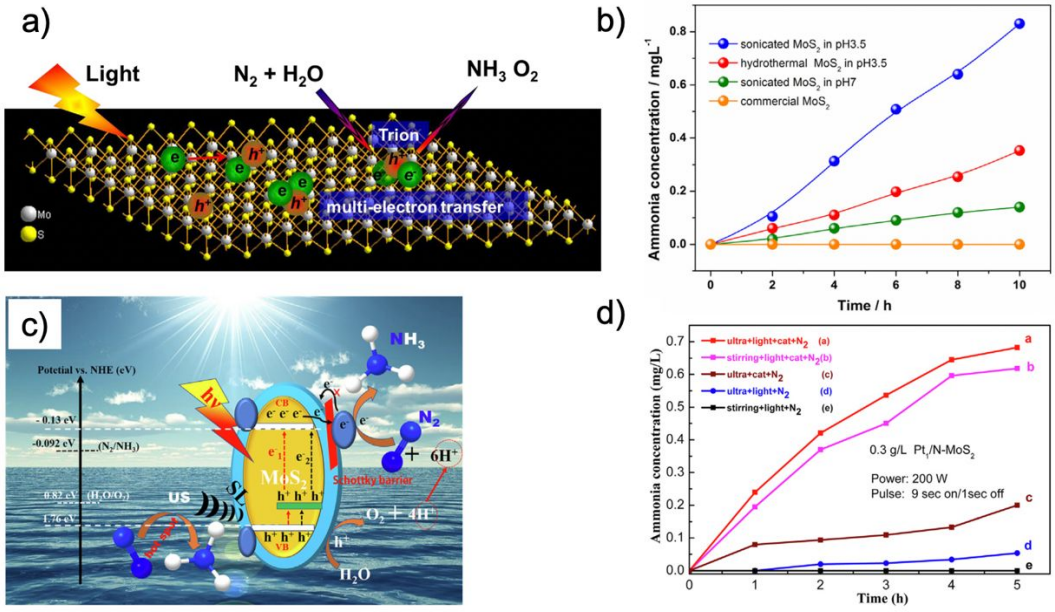

Fig. 27. a) Schematic representation of trion formation and nitrogen fixation on ultra-thin MoS_2. b) Plot of ammonia yield of ultra-thin MoS_2 samples under illumination from a 500 W Xenon lamp with a 420-nm cutoff filter. Reprinted with permission.[114] Copyright 2017 Elsevier Inc. c) Band diagram with schematic representation of the NRR on Pt/N-MoS_2 under sonophotofixation conditions. d) Plot of NH_3 yield rate and FE for Pt/N-MoS_2 under irradiation (300 W Xenon lamp). Reprinted with permission.[257] Copyright 2020 Elsevier Inc.

Sun *et al.* employed an oxygen doped 1T-MoS_2/CdS heterostructure rich in sulfur vacancies (SV-1T-MoS_2/CdS) for photochemical NRR.[258] The 30 wt% SV-1T-MoS_2/CdS (30wt% refers to the percentage of SV-1T-MoS_2 relative to CdS) outperformed a 0.1 wt% Pt/CdS catalyst under similar reaction conditions (simulated solar AM 1.5 G). The 30 wt% SV-1T-MoS_2/CdS showed an NH_3 yield rate of 8220.83 μmol L^{-1} h^{-1} g^{-1} (0.1398 mg L^{-1} h^{-1} mg^{-1}_{cat}) in a 20 vol% methanol solution, where methanol acts as a hole scavenger. The sulfur vacancies introduce defect sites that act as electron capture sites for the photoexcited electrons to reduce N_2. According to their DFT results, the reaction mechanism contains mixed alternating and distal pathways, where the potential determining step is *$NHNH_2$ to *NH_2 + *NH_3.[171] The 2D TMDCs as NRR catalysts are showing promising results; however, there are still areas of opportunity within the structure, composition, and phase engineering to overcome the NRR challenges.

Table 4. Comparison of the NRR activity of 2D TMDCs.

Materials	Electrolyte	Activity	FE	Potential V vs. RHE	Reference
		Electrochemical Process			
MoS_2/CC	0.1 M Na_2SO_4	4.94 mg h^{-1} cm^{-2}	1.17	-0.5 V	235
DR MoS_2	0.1 M Na_2SO_4	29.28 mg h^{-1} mg^{-1}	8.34	-0.4 V	240
MoS_2 with Li interaction	0.1 M Li_2SO_4	43.4 mg h^{-1} mg^{-1}	9.81	-0.2 V	259
MoS_2-rGO	0.1 M $LiClO_4$	24.82 mg h^{-1} mg^{-1}	4.58	-0.45 V	260
3D hollow Co-MoS_2	0.1 M Na_2SO_4	129.93mg h^{-1} mg^{-1}	11.21	-0.4 V	241
NiFe@MoS_2 NCs	0.1 M Na_2SO_4	128.17mg h^{-1} mg^{-1}	11.34	-0.3 V	243
AuNP@MoS_2	0.1 M HCl 0.1 M KOH 0.1 M Na_2SO_4	4.40 mg h^{-1} mg^{-1} 25.0 mg h^{-1} mg^{-1} 5.65 mg h^{-1} mg^{-1}	<1% 3.9 9.70	-0.3 V	242

Ru/2H-MoS_2	0.1 M Na_2SO_4	6.98 mg h^{-1} mg^{-1}	17.6	-0.15 V	244
1T-MoS_2 NDs/g-C_3N_4	0.1 M HCl	29.97 mg h^{-1} mg^{-1}	20.48	-0.3 V	239
1T-MoS_2-Ni	0.25 M $LiCLO_4$	63 mg h^{-1} cm^{-2}	27.66	-0.3 V	245
F-MoS_2	0.05 M H_2SO_4	35.7 mg h^{-1} mg^{-1}	20.6	-0.2 V	261
N-doped MoS_2	0.1 M Na_2SO_4	69.82 mg h^{-1} mg^{-1}	9.14	-0.3 V	260
1T-MoS_2@Ti_3C_4	0.1 M HCl	30.33 mg h^{-1} mg^{-1}	10.94	-0.3 V	13
MoS_2/C_3N_4	0.1 M $LiClO_4$	18.5 mg h^{-1} mg^{-1}	17.8	-0.3 V	248
MoS_2/C_3N_4	0.1 M Na_2SO_4	19.86 mg h^{-1} mg^{-1}	6.87	-0.5 V	249
MoS_2 NDs/RGO	0.1 M Na_2SO_4	16.41mg h^{-1} mg^{-1} @-0.75 V vs. RHE	27.93	-0.35 V	247
Hollow $MoSe_2$	0.1 M Na_2SO_4	11.2 mg h^{-1} mg^{-1}	0.2	-0.6 V	250
1T@2H $MoSe_2$	0.1 M Na_2SO_4	19.91 mg h^{-1} mg^{-1}	2.82	-0.6 V	254
$NbSe_2$	0.1 M Na_2SO_4	89.5 mg h^{-1} mg^{-1} at -0.45 V vs. RHE	13.9	-0.4 V	253
NbS_2	0.1 M HCl	37.58 mg h^{-1} mg^{-1}	10.12	-0.5 V	251
Fe-ReS_2@N-CNF	0.1 M Na_2SO_4	80.4 mg h^{-1} mg^{-1}	12.3	-0.2 V	262
TiS_2	0.1 M Na_2SO_4	16.02 mg h^{-1} mg^{-1}	5.50	-0.6 V	255
B-doped VS_2 /CC	0.5 M $LiClO_4$	55.7 mg h^{-1} mg^{-1}	~9	-0.4 V	252
Photoelectrochemical Process					

MoS_2@TiO_2	0.1 M Na_2SO_4 100 mW cm^{-2}, AM 1.5 G	1.42 μmol h^{-1} cm^{-2}	65.52	-0.2 V	256
Photochemical Process					
Ultra-thin MoS_2	500 W Xenon lamp in pH 3.5	5.525 μg h^{-1} mg^{-1}	N/A		114
Pt/N-MoS_2	300 W Xenon lamp	2.060 μg h^{-1} mg^{-1}			257
	300 W Xenon lamp, Ultrasonication	2.275 μg h^{-1} mg^{-1}			
SV-1T-MoS_2/CdS	Simulated solar AM 1.5 G in 20 vol% methanol	0.1398 mg L^{-1} h^{-1} mg^{-1}_{cat}			171
Fe-$MoTe_2$	300 W Xenon lamp in Milli-Q water	129.08 μmol g^{-1} h^{-1}			263

*CC-carbon cloth, DR-defect rich, rGO-reduced graphene oxide, NC-nanocube, ND-nano dots, the rates indicated are the amount of ammonia in μg produced per hour of electrolysis on a unit mass of catalyst in mg. N/A- not applicable

4.3 2D MXenes

4.3.1 Electrochemical and Photoelectrochemical NRR

In 2016, Azofra and coworkers predicted the 2D d^2-d^4 M_3C_2 transition metal carbides (MXenes) to be prospective NRR catalysts.[222] Since then, a handful of studies have looked at electrochemical NRR with MXenes (Table 5). Zhao *et al.* found that $Ti_3C_2T_x$, T_x=F, OH (Fig. 28a) could achieve an NH_3 yield rate of 20.4 μg $h^{-1}mg^{-1}$ with FE of 9.3% at -0.4 V vs. RHE (Fig. 28b).[236] DFT calculations revealed that the most favorable orientation for N_2 adsorption was side-on, where the N–N bond elongates to 1.268 Å. In contrast, end-on adsorption showed bond elongation to 1.194 Å. First-principles calculations showed that a distal pathway is preferred over the alternating pathway (labeled as mixed in Fig. 28c). [236] Xia and coworkers engineered $Ti_3C_2T_x$ surfaces to obtain OH, F, and O surface-terminated MXenes as shown in Fig. 28d, e, and f, respectively.[264] They found that the best performance was with OH surface termination at 60 °C (reaction

temperature) to give an ammonia yield rate of ~12 μg $h^{-1}cm^{-2}$ (0.8 μg h^{-1} mg^{-1}) with FE of 9.03% at -0.2V vs. RHE (Fig. 28g). DFT results suggested that OH terminations, compared to the F and O surface terminations, increase the DOS around the Fermi level and thus lower the charge transfer resistance to the adsorbed N_2.[264]

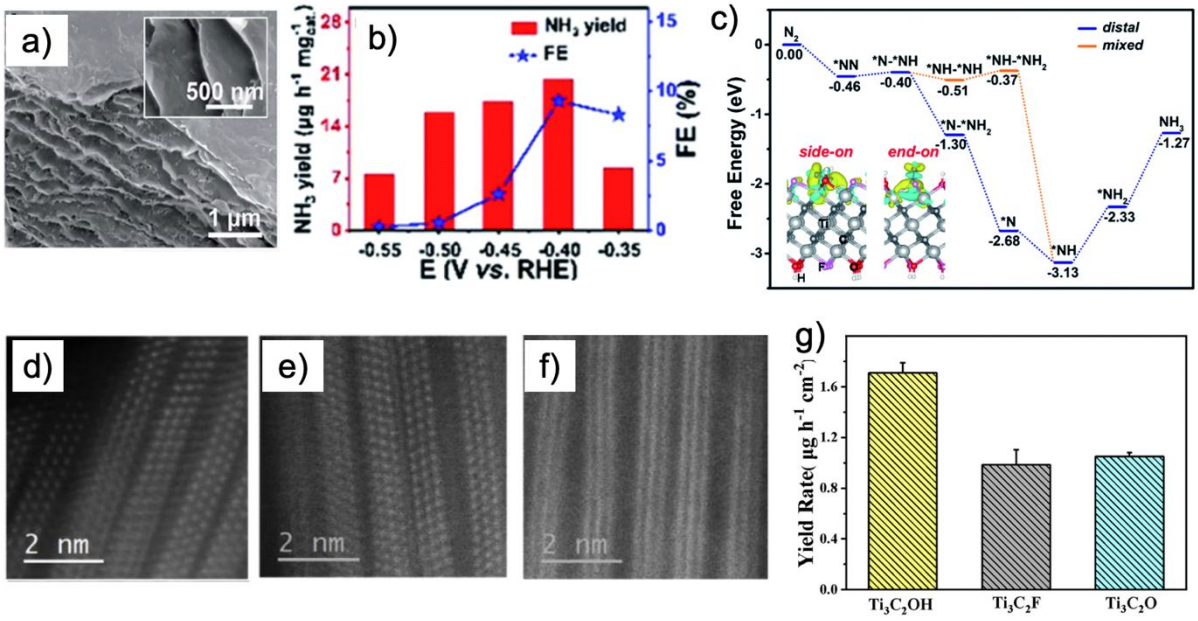

Fig. 28. a) SEM image of $Ti_3C_2T_x$ (T_x=F, OH) MXene. (b) Ammonia yield rate plots for the $Ti_3C_2T_x$ MXenes at different applied potentials and c) reaction scheme for the nitrogen fixation for Ti_3C_2 MXene for distal and mixed mechanisms. Reprinted with permission.[236] Copyright 2018 The Royal Society of Chemistry. d), e) and f) are HR-TEM images of the $Ti_3C_2T_x$ MXene with varying functional groups OH, F and O, respectively. g) Plot of ammonia yield for different surface functional groups on $Ti_3C_2T_x$ MXene and for different surface terminations. Reprinted with permission.[264] Copyright 2020 Elsevier Inc.

Other reports have increased NRR performance with MXenes by using heterostructures, defects, and metal cocatalysts. Luo *et al.* explored $Ti_3C_2T_x$ MXenes attached to a vertically (perpendicular) and horizontally (parallel) aligned metal host electrode (FeOOH nanosheets) for NRR (Fig. 29a and b).[265] The vertically configured $Ti_3C_2T_x$ assembly had better NRR electrochemical activity yielding 5.78% FE at -0.2 V vs. RHE (Fig. 29c) but with a low yield rate of 0.148 μg h^{-1} mg^{-1}. DFT results revealed that $Ti_3C_2O_2$ edge sites have optimal N_2 binding energies, with exposed Ti atoms being particularly active towards NRR. Thus, the vertical

orientation with more exposed Ti edges (confirmed with HRTEM and FFT patterns) had better NRR activity.[265]

The etching process used in MXene synthesis is thought to reduce the density of surface metal sites that are predicted to be most active for NRR, since O, F, and OH surface terminations are unavoidable.[266] Guo *et al.* modified the surface terminations by introducing iron (Fe) in the etching step to replace F*/OH* surface terminations with Fe atoms (Fig. 29d).[266] The Fe surface modification reduced the $Ti_3C_2T_x$ surface work function, which increased the DOS near E_F and lowered the energy barrier for efficient electron transfer from the catalyst to the adsorbed N_2 molecules and reaction intermediates. This Fe-modified $Ti_3C_2T_x$ (Fig. 29e) catalyst generated ammonia at a rate of 21.9 μg h^{-1} mg^{-1} with FE of 25.44% at -0.2 V vs. RHE (Fig. 29f).[266] Fang *et al.* coupled oxygen-vacancy-rich TiO_2 to $Ti_3C_2T_x$ by reacting $Ti_3C_2T_x$ in ethanol under hydrothermal conditions, where TiO_2 nanoparticles attached to exposed edge Ti sites.[267] The $Ti_3C_2T_x$ support prevents TiO_2 nanoparticle aggregation and also provides a conductive backbone to give an ammonia yield rate of 32.17 μg $h^{-1}mg^{-1}$ with FE of 16.07% at -0.55 V vs. RHE. DFT results identified oxygen vacancies as the active sites, where the adsorbed N_2 had an increased bond length from 1.109 Å to 1.136 Å, and then the activated N_2 proceeds *via* a distal pathway with an end-on orientation. The potential-determining step was identified as the second PCET step (NNH* to NNH_2*), whereas the potential-determining steps for pure TiO_2 and $Ti_3C_2T_x$ surfaces were identified as the first PCET step (*i.e.,* NN* to NNH*).[267]

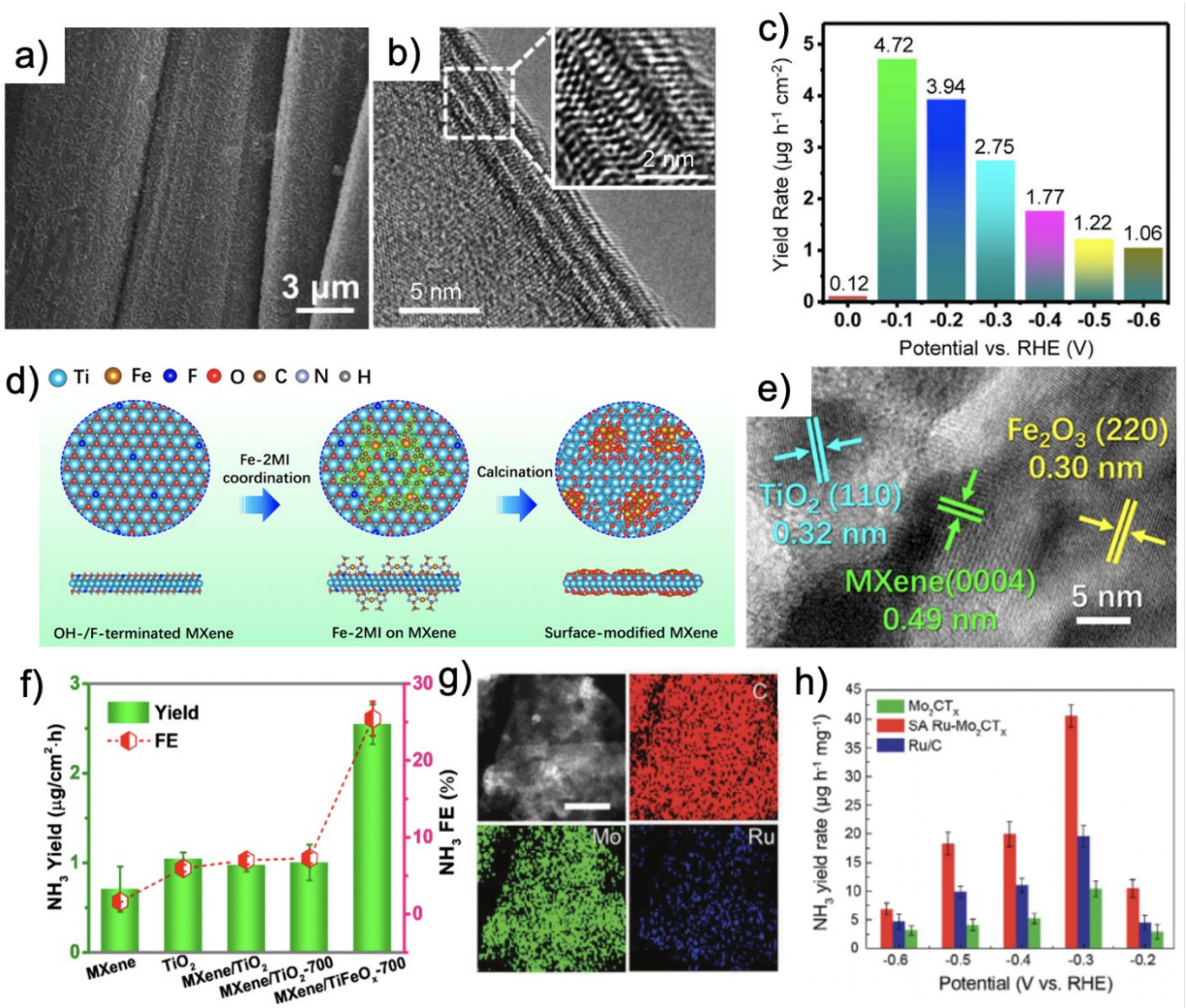

Fig. 29. a) SEM images of vertical configured $Ti_3C_2T_x$ on FeOOH and b) HRTEM image of MXene nanosheets with exposed Ti. c)Yield rate for the formation of ammonia on the $Ti_3C_2T_x$ grown on vertically aligned FeOOH. Reprinted with permission.[265] Copyright 2019 Elsevier Inc. d) Schematic of surface functional groups being replaced with Fe calcination on the $Ti_3C_2T_x$ surface. e) HRTEM showing the TiO_2/Fe_2O_3 on the MXene surface. f) Comparison of the NH_3 yield rates and FE of pristine MXenes with $TiFeO_x$ heterostructures. Reprinted with permission.[266] Copyright 2020 American Chemical Society. g) STEM-EDS mapping of single atom (SA) Ru on Mo_2CT_x MXene, and h) ammonia yield rate comparison on the pure MXene, Ru/C, and SA Ru-Mo_2CT_x. Reprinted with permission.[268] Copyright 2020 John Wiley and Sons.

MXenes have also been coupled with metal cocatalysts for NRR. Liu and coworkers interfaced gold nanoparticles with a $Ti_3C_2T_x$ (T_x=OH) MXene.[269] The interface between the Au and Ti_3C_2 weakened (activated) N_2 molecules by increasing the N–N triple bond length. The Au@Ti_3C_2

showed an ammonia yield rate of 30.06 μg $h^{-1}mg^{-1}$ reaching a FE of 18.34% at -0.2 V. DFT calculations identified an alternating pathway as the most probable route for NH_3 production with the potential-determining step being $*NH_2NH_2$ to $*NH_2$ + NH_3.[269] Ru decorated Ti_3C_2 MXene (Ru@Ti_3C_2) was studied as an ambient NRR catalysis by Liu et al, where they achieved an ammonia yield rate of 2.3 μmol $h^{-1}cm^{-2}$ with a FE of 13.13% at -0.4 V vs. RHE.[270] Peng *et al.* demonstrated Ru-decorated Mo_2CT_x MXenes (Fig. 29g) that produce NH_3 at a yield rate of 40.57 μg $h^{-1}mg^{-1}$ and 25.77% FE of at -0.3 V vs. RHE (Fig. 29h).[268] X-ray absorption studies revealed a positive valence state (+3.27) of Ru in the heterostructure, which under operando electrochemical conditions increased up to +3.56. This increase is due to a delocalization of the unpaired electrons in the Ru 3d orbital and charge transfer from Ru atoms to the N_2 antibonding π* orbitals activating N_2 for NRR.[268] To the best of our knowledge, photoelectrochemical NRR with MXenes is very rare or do not exist; therefore, this is an area ripe with opportunity.

4.3.2 Photochemical NRR

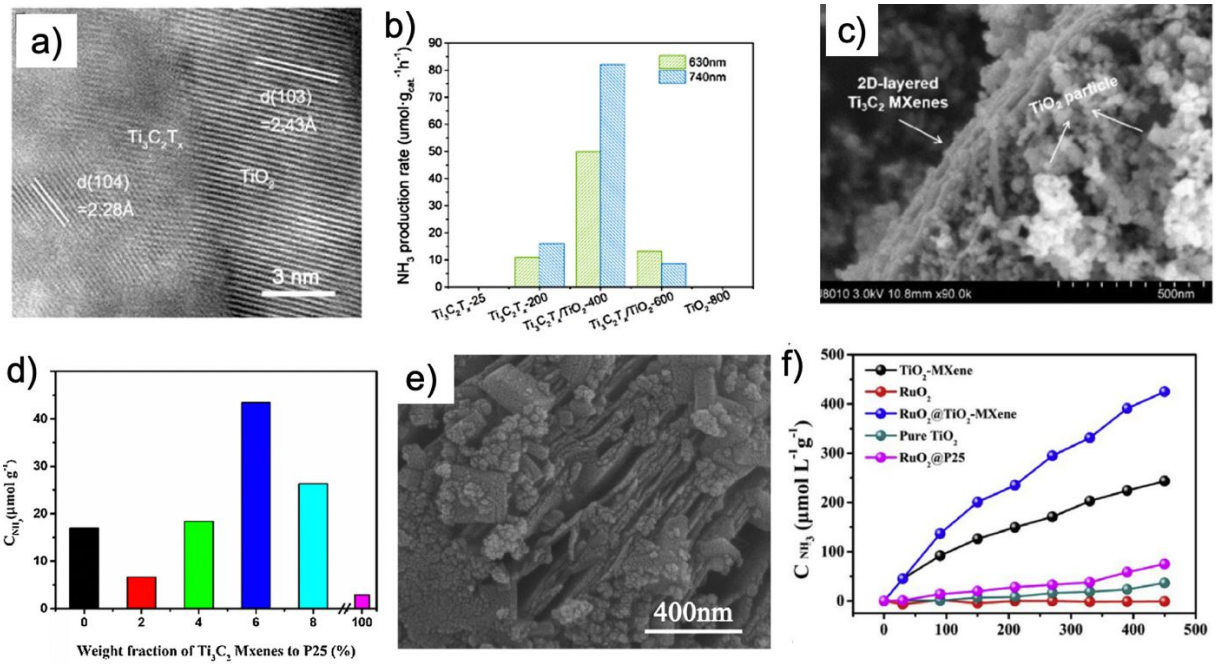

Fig. 30. a) HAADF-STEM image of TiO_2 grown on $Ti_3C_2T_x$ MXene ($Ti_3C_2T_x/TiO_2$-400). b) Plots of ammonia yield rates for ($Ti_3C_2T_x/TiO_2$-400) with full spectrum irradiation using a Xe lamp. Reprinted with permission.[271] Copyright 2020 Elsevier Inc. c) SEM micrograph of 6% $Ti_3C_2T_x$ MXene-P25, and d) corresponding ammonia yield rates for samples with varying weight fraction of Ti_3C_2 (full spectrum irradiation with a 300 W Xe lamp) carried out in methanol. Reprinted with permission.[272] Copyright 2020 Elsevier Inc. e) SEM image of as-prepared $RuO_2@TiO_2$-MXene, and f) ammonia yield rate comparison for $RuO_2@TiO_2$-MXene with TiO_2-MXene and RuO_2 samples irradiated with a Xe lamp (100 $mWcm^{-2}$). Reprinted with permission.[273] Copyright 2020 Elsevier Inc.

Since most MXenes are metallic, photochemical catalytic reactions primarily use MXenes as NRR cocatalysts with a second semiconducting photoabsorber, which is similar to CO_2RR in the previous section. As an example, several studies have successfully converted some of the surface Ti atoms in $Ti_3C_2T_x$ to TiO_2 to act as a photoabsorber. Hou and coworkers synthesized a $Ti_3C_2T_x/TiO_2$ hybrid structure by heating $Ti_3C_2T_x$ (T_x=OH, O, F) at 400 °C under ambient conditions (Fig. 30a).[271] The $Ti_3C_2T_x/TiO_2$ hybrid structure produced NH_3 at a yield rate of 7.174 μg $h^{-1}mg^{-1}$ under full spectrum irradiation of a xenon lamp. The hybrid catalyst also exhibited a considerable yield rate of ammonia (~80 μmol $h^{-1}mg^{-1}$) with near infrared (NIR) illumination only (Fig. 30b). The $Ti_3C_2T_x/TiO_2$ hybrid showed a broad plasmonic absorption band at ~550 nm, which resulted in visible and NIR light generating hot electrons. The presence of defect states (oxygen vacancies) on the TiO_2 enabled charge separation, efficiently trapping electrons at these oxygen vacancies for NRR, and DFT results supported this conclucusion.[271]

Liao *et al.* constructed a $Ti_3C_2T_x$/P25 heterostructure (P25 = 80% anatase and 20% rutile phases of TiO_2) by mixing P25 with different MXene weight ratios followed by calcination at 300 °C in a N_2 atmosphere (Fig. 30c).[272] NRR in water showed an optimal NH_3 yield rate of 10.74 μmol h^{-1} g^{-1} with 6% MXene loading. The same reaction carried out in methanol produced a 4-fold improvement (43.44 μmol h^{-1} g^{-1}), where the improved activity was attributed to methanol being a better hole scavenger than water (Fig. 30d). The authors claim the MXene loading generated oxygen vacancies (due to partial migration of oxygen from P25 to the interface between

the P25 and the MXene during the calcination) that slowed electron-hole pair recombination and promoted N_2 adsorption and activation.[272] Hao *et al.* used a TiO_2-$Ti_3C_2T_x$ loaded with RuO_2 (Fig. 30e), where photoexcited TiO_2 can transfer electrons to $Ti_3C_2T_x$ for NRR catalysis.[273] Under irradiation with a xenon lamp, the RuO_2@TiO_2-MXene catalyst yielded 425 μmol L^{-1} g^{-1} of NH_3 after 450 min (Fig. 30f). The authors claim the large adsorption energies on the $Ti_3C_2T_x$ captured and activated the N_2 molecules for NRR and that RuO_2 nanoparticles with significant amounts of Ru(0) reduced the energy barrier for the first PCET step, thus increasing the NRR activity.[273] With 2D MXenes still being realized, there is a lot of opportunity for overcoming the current NRR challenges with these emerging 2D catalysts.

Table 5. Comparison of the NRR activity of 2D MXenes

Materials	Electrolyte	Activity	FE	Potential V vs. RHE	Reference
Electrochemical Process					
$Ti_3C_2T_x$	0.1 M HCl	20.4 mg h^{-1} mg^{-1}	9.3	-0.4 V	236
Ti_3C_2OH	0.1 M KOH	1.17 mg h^{-1} cm^{-2} 12 mg h^{-1} cm^{-2}	7.01 9.03	-0.2 V @20 °C -0.2 V @60 °C	264
$Ti_3C_2T_x$-SSM* $Ti_3C_2T_x$-FeOOH	0.5 M Li_2SO_4	2.68 mg h^{-1} mg^{-1} 0.33 mg h^{-1} mg^{-1}	4.62 0.09	-0.1 V -0.5 V	265
$Ti_3C_2T_x$ ironed	0.05 M H_2SO_4	21.9 mg h^{-1} mg^{-1}	25.44	-0.2 V	266
TiO_2/$Ti_3C_2T_x$	0.1 M HCl	32.17 mg h^{-1} mg^{-1}	16.07	-0.55 V	267
Au@Ti_3C_2	0.05 M HCl	30.06 mg h^{-1} mg^{-1}	18.34	-0.2 V	269
Ru@Ti_3C_2	0.1 M KOH	2.3 mmol $h^{-1}cm^{-2}$	13.13	-0.4 V	270
Ru-Mo_2CT_x	0.5 M K_2SO_4	40.57 mg $h^{-1}mg^{-1}$	25.77	-0.3 V	268
Photochemical Process					

$Ti_3C_2T_x/TiO_2$ hybrid	Full spectrum Xenon	7.174 mg $h^{-1}mg^{-1}$	271
$Ti_3C_2T_x$/P25	300 W Xenon lamp	10.74 mmol h^{-1} g^{-1}	272
	Methanol	43.44 mmol h^{-1} g^{-1}	
RuO_2@TiO_2-MXene	xenon lamp	425 mmol L^{-1} g^{-1}	273

*SSM-Stainless steel mesh, the rates indicated are the amount of ammonia in μg produced per hour of electrolysis on a unit mass of catalyst in mg

5. Conclusion and Perspective

Environmental concerns related to greenhouse gas emissions and energy-intensive chemical manufacturing processes have instigated a large push for fuels, fertilizers, and feedstocks to come from renewable materials and chemicals in an energy efficient manner. One emerging strategy involves 2D TMDCs and MXene catalysts for CO_2RR and NRR that we have highlighted in this review to be a potential environmentally friendly and low-cost option. To realize commercially viable 2D catalysts, innovative strategies seek to use the tunable structures, energetics, and mechanical properties of 2D TMDCs and MXenes to lower activation energy barriers for chemisorption and hydrogenation of CO_2 and N_2 and improve reaction kinetics and selectivity.

In this Review, we introduced the recent progress on developing 2D TMDC and MXene catalysts through (photo)electrochemical and photochemical processes for CO_2RR and NRR. We discuss the relevant electronic and physical structures along with the various synthesis methods, possible reaction mechanisms including key intermediates and final products, and the current achievements in theoretical and experimental studies for CO_2RR and NRR. Despite recent efforts on 2D materials and their heterostructures for enhanced intrinsic catalytic activity, it is important to note that CO_2RR and NRR continue to face challenges on the slow reaction kinetics and poor

product selectivity. In practice, there are still several uncultivated 'lands' for rational design of CO_2RR and NRR catalysts based on 2D TMDCs and MXenes, which remain to be 'ploughed' for reaching the efficiency, stability, and cost needed for industrial applications.

First, the active sites of most intrinsic 2D TMDCs and MXenes are usually limited to the edges. Developing strategies for activating the inert basal planes (*e.g.,* strain, phase change, defects, and functionalization) and increase edge densities through different morphologies (*e.g.,* vertically oriented 2D materials and flower shape) are promising avenues for efficient CO_2RR and NRR. Second, the recent development of single-atom catalysts opens additional avenues for 2D materials as host materials. Coupling single atom catalysts (SAC) with 2D host materials has the opportunity for dense decoration of single atoms, due to the large surface/volume ratio. The single atom catalyst also has the potential to locally perturb the electronic states of 2D TMDC/MXene and could impact the activation/intermediate steps, as has been previously suggested.[31] The roles of catalytic control and regulation by each component within these SAC-TMDC/MXene catalysts are still poorly understood and represent areas of opportunity. The engineering of the single atom/2D material is suitable for both theoretical and experimental studies for CO_2RR and NRR, where controllable synthesis methods need to be developed for the desired configurations.

Third, the current synthesis procedures of 2D TMDCs and MXenes are complex and are typically performed on the microscale. Therefore, industrial-scale production and manufacturing of these 2D materials with low-cost, repeatability, and high stability is urgently needed before commercialization of these catalysts can be realized. Some potential scalable synthesis routes would be liquid exfoliation, chemical exfoliation, hydrothermal growth, etc.[274, 275] Fourth, the catalysts (composition, size, shape, oxidation state, and crystallographic structure), electrolytes (cation, anion, concentration, and pH), temperature, pressure, and applied potentials are all critical

to the CO_2RR and NRR scheme and still need to optimized.[134] For example, the most studied compositions of TMDCs in the literatures revolve around Mo or W for the transition metal and S or Se for the chalcogenide. Further composition explorations are necessary to develop other TMDCs and MXenes for CO_2RR and NRR.

Overall, such 2D TMDC and MXene catalysts are not industrially viable yet for CO_2RR and NRR due to low yields and conversion efficiencies. Though the recent lab-scale electrocatalysts can transform CO_2 into C_1 products (CO or formate) with over 95% FE with high production rates (>20 mA cm^{-2} for H-type cell and >100 mA cm^{-2} for flow cell), the large intrinsic energy barrier of CO_2 capture and selective production of long-chain (C_{2+}) feedstocks in high efficiencies are still far away from the magnitude of industrial catalysts (>100s mA cm^{-2}).[245] As a goal for electrochemical NH_3 generation, DOE ARPA-E has targeted NH_3 yield rates at 10^{-6} $mols^{-1}cm^{-2}$, FE at 90%, and energy efficiencies at 60% with minimal catalyst degradation over 1000 h, which are also much greater than the current state of the art.[246,276] Therefore, the immediate challenge of 2D TMDCs and MXenes for CO_2RR and NRR is understanding how to enhance and control the catalytic activities and then scaling up the appropriate catalysts.

Besides the mechanistic understanding and catalyst development, future research efforts also need to go beyond the catalyst to focus on the surrounding microenvironment to understand how the catalytic site is affected by these other reaction conditions. For example, trace impurities in the electrolyte can deactivate catalytic sites and affect catalyst performance, while nonaqueous and ionic-liquid electrolyte could increase the CO_2 and N_2 solubility and product selectivity. Also, to increase the N_2 and CO_2 solubility at the catalyst surface and improve prodcut seperation, the reactors and electrodes could be designed to have better seperation of cathodic/anodic products as well as control the reaction kinetics at the three-phase boundary. For

example, gas diffusion electrodes (GDE) have been widely studied as critical components in gas-phase electrolyzers for overcoming diffusion limitations of gas molecules from the bulk solution to the electrode surface[277]. This exploration is still limited within the 2D TMDC and MXene catalyst community and could be an area of opportunity to increase the FE and yield rates. 2D TMDCs and MXenes offer great opportunities to repurpose emitted CO_2 into C-based fuels and provide lower energy routes to NH_3 production *via* (photo)electrochemical and photochemical routes and, therefore, should continue to be studied and investigated.

Acknowledgement: This work was authored by the National Renewable Energy Laboratory, operated by Alliance for Sustainable Energy, LLC, for the U.S. Department of Energy (DOE) under Contract No. DE-AC36-08GO28308. Funding provided by the Solar Photochemistry Program, Division of Chemical Sciences, Geosciences, and Biosciences, Office of Basic Energy Sciences, U.S. Department of Energy (DOE). The views expressed in the article do not necessarily represent the views of the DOE or the U.S. Government. The U.S. Government retains and the publisher, by accepting the article for publication, acknowledges that the U.S. Government retains a nonexclusive, paid-up, irrevocable, worldwide license to publish or reproduce the published form of this work, or allow others to do so, for U.S. Government purposes.

Reference

1. X. Zhu and Y. Li, *Wiley Interdisciplinary Reviews: Computational Molecular Science*, 2019, **9**.
2. X. Guo, H. Du, F. Qu and J. Li, *Journal of Materials Chemistry A*, 2019, **7**, 3531-3543.
3. C. Smith, A. K. Hill and L. Torrente-Murciano, *Energy & Environmental Science*, 2020, **13**, 331-344.

4. S. Lukman, L. Ding, L. Xu, Y. Tao, A. C. Riis-Jensen, G. Zhang, Q. Y. S. Wu, M. Yang, S. Luo, C. Hsu, L. Yao, G. Liang, H. Lin, Y. W. Zhang, K. S. Thygesen, Q. J. Wang, Y. Feng and J. Teng, *Nat Nanotechnol*, 2020, **15**, 675-682.
5. H. Zhou, H. Polshyn, T. Taniguchi, K. Watanabe and A. F. Young, *Nature Physics*, 2019, **16**, 154-158.
6. H. Jiang, L. Zheng, Z. Liu and X. Wang, *InfoMat*, 2019, **2**, 1077-1094.
7. D. Akinwande, C. Huyghebaert, C. H. Wang, M. I. Serna, S. Goossens, L. J. Li, H. P. Wong and F. H. L. Koppens, *Nature*, 2019, **573**, 507-518.
8. X. Chia and M. Pumera, *Nature Catalysis*, 2018, **1**, 909-921.
9. H. Zhang, *ACS Nano*, 2015, **9**, 9451-9469.
10. K. W. Nam, S. S. Park, R. Dos Reis, V. P. Dravid, H. Kim, C. A. Mirkin and J. F. Stoddart, *Nat Commun*, 2019, **10**, 4948.
11. M. Naguib, V. N. Mochalin, M. W. Barsoum and Y. Gogotsi, *Adv Mater*, 2014, **26**, 992-1005.
12. J. Kang, J. Li, F. Wu, S.-S. Li and J.-B. Xia, *The Journal of Physical Chemistry C*, 2011, **115**, 20466-20470.
13. N. Zhang, J. Wu, T. Yu, J. Lv, H. Liu and X. Xu, *Frontiers of Physics*, 2020, **16**, 23201.
14. A. Molle, J. Goldberger, M. Houssa, Y. Xu, S.-C. Zhang and D. Akinwande, *Nature Materials*, 2017, **16**, 163-169.
15. A. P. Côté, H. M. El-Kaderi, H. Furukawa, J. R. Hunt and O. M. Yaghi, *Journal of the American Chemical Society*, 2007, **129**, 12914-12915.
16. J. W. Colson, A. R. Woll, A. Mukherjee, M. P. Levendorf, E. L. Spitler, V. B. Shields, M. G. Spencer, J. Park and W. R. Dichtel, *Science*, 2011, **332**, 228-231.
17. B. Anasori, M. R. Lukatskaya and Y. Gogotsi, *Nature Reviews Materials*, 2017, **2**.
18. S. Zhao, J. Xue and W. Kang, *Chemical Physics Letters*, 2014, **595-596**, 35-42.
19. Y. Xiao and W. Zhang, *Nanoscale*, 2020, **12**, 7660-7673.
20. Z. Fu, N. Wang, D. Legut, C. Si, Q. Zhang, S. Du, T. C. Germann, J. S. Francisco and R. Zhang, *Chem Rev*, 2019, **119**, 11980-12031.
21. W. Choi, N. Choudhary, G. H. Han, J. Park, D. Akinwande and Y. H. Lee, *Materials Today*, 2017, **20**, 116-130.
22. D. L. Anderson, *Theory of the Earth*, Blackwell Scientific Publications, 1989.
23. M. Asadi, B. Sayahpour, P. Abbasi, A. T. Ngo, K. Karis, J. R. Jokisaari, C. Liu, B. Narayanan, M. Gerard, P. Yasaei, X. Hu, A. Mukherjee, K. C. Lau, R. S. Assary, F. Khalili-Araghi, R. F. Klie, L. A. Curtiss and A. Salehi-Khojin, *Nature*, 2018, **555**, 502-506.
24. D. Voiry, J. Yang and M. Chhowalla, *Adv Mater*, 2016, **28**, 6197-6206.
25. X. Jiang, A. V. Kuklin, A. Baev, Y. Ge, H. Ågren, H. Zhang and P. N. Prasad, *Physics Reports*, 2020, **848**, 1-58.
26. A. Kakekhani and S. Ismail-Beigi, *ACS Catalysis*, 2015, **5**, 4537-4545.
27. D. Voiry, A. Mohite and M. Chhowalla, *Chem Soc Rev*, 2015, **44**, 2702-2712.
28. W. Yuan, L. Cheng, Y. An, H. Wu, N. Yao, X. Fan and X. Guo, *ACS Sustainable Chemistry & Engineering*, 2018, **6**, 8976-8982.
29. L. Lin, P. Sherrell, Y. Liu, W. Lei, S. Zhang, H. Zhang, G. G. Wallace and J. Chen, *Advanced Energy Materials*, 2020, **10**.

30. D. Vikraman, S. Hussain, K. Akbar, K. Karuppasamy, S.-H. Chun, J. Jung and H.-S. Kim, *ACS Sustainable Chemistry & Engineering*, 2018, **7**, 458-469.
31. Y. Wang, J. Mao, X. Meng, L. Yu, D. Deng and X. Bao, *Chem Rev*, 2019, **119**, 1806-1854.
32. S. Li, P. Tuo, J. Xie, X. Zhang, J. Xu, J. Bao, B. Pan and Y. Xie, *Nano Energy*, 2018, **47**, 512-518.
33. J. L. Hart, K. Hantanasirisakul, A. C. Lang, B. Anasori, D. Pinto, Y. Pivak, J. T. van Omme, S. J. May, Y. Gogotsi and M. L. Taheri, *Nat Commun*, 2019, **10**, 522.
34. X. Yang, N. Gao, S. Zhou and J. Zhao, *Phys Chem Chem Phys*, 2018, **20**, 19390-19397.
35. A. Hasani, M. A. Teklagne, H. H. Do, S. H. Hong, Q. Van Le, S. H. Ahn and S. Y. Kim, *Carbon Energy*, 2020, **2**, 158-175.
36. X. Jiao, K. Zheng, L. Liang, X. Li, Y. Sun and Y. Xie, *Chem Soc Rev*, 2020, **49**, 6592-6604.
37. G. Zhang, Y. Li, C. He, X. Ren, P. Zhang and H. Mi, *Advanced Energy Materials*, 2021, **11**.
38. Y. Huan, J. Shi, G. Zhao, X. Yan and Y. Zhang, *Energy Technology*, 2019, DOI: 10.1002/ente.201801025.
39. Y. Wei, R. A. Soomro, X. Xie and B. Xu, *Journal of Energy Chemistry*, 2021, **55**, 244-255.
40. J. Chen, Q. Huang, H. Huang, L. Mao, M. Liu, X. Zhang and Y. Wei, *Nanoscale*, 2020, **12**, 3574-3592.
41. Y. Yuan, R.-t. Guo, L.-f. Hong, X.-y. Ji, Z.-s. Li, Z.-d. Lin and W.-g. Pan, *Colloids and Surfaces A: Physicochemical and Engineering Aspects*, 2021, **611**.
42. Y. Huang, Y. H. Pan, R. Yang, L. H. Bao, L. Meng, H. L. Luo, Y. Q. Cai, G. D. Liu, W. J. Zhao, Z. Zhou, L. M. Wu, Z. L. Zhu, M. Huang, L. W. Liu, L. Liu, P. Cheng, K. H. Wu, S. B. Tian, C. Z. Gu, Y. G. Shi, Y. F. Guo, Z. G. Cheng, J. P. Hu, L. Zhao, G. H. Yang, E. Sutter, P. Sutter, Y. L. Wang, W. Ji, X. J. Zhou and H. J. Gao, *Nat Commun*, 2020, **11**, 2453.
43. V. Nicolosi, M. Chhowalla, M. G. Kanatzidis, M. S. Strano and J. N. Coleman, *Science*, 2013, **340**, 1226419-1226419.
44. M. Naguib, M. Kurtoglu, V. Presser, J. Lu, J. Niu, M. Heon, L. Hultman, Y. Gogotsi and M. W. Barsoum, *Advanced Materials*, 2011, **23**, 4248-4253.
45. N. H. Attanayake, A. C. Thenuwara, A. Patra, Y. V. Aulin, T. M. Tran, H. Chakraborty, E. Borguet, M. L. Klein, J. P. Perdew and D. R. Strongin, *ACS Energy Letters*, 2018, **3**, 7-13.
46. J. P. Motter, K. J. Koski and Y. Cui, *Chemistry of Materials*, 2014, **26**, 2313-2317.
47. Z. Chen, K. Leng, X. Zhao, S. Malkhandi, W. Tang, B. Tian, L. Dong, L. Zheng, M. Lin, B. S. Yeo and K. P. Loh, *Nature Communications*, 2017, **8**, 14548.
48. A. Splendiani, L. Sun, Y. Zhang, T. Li, J. Kim, C.-Y. Chim, G. Galli and F. Wang, *Nano Letters*, 2010, **10**, 1271-1275.
49. K. F. Mak, C. Lee, J. Hone, J. Shan and T. F. Heinz, *Physical Review Letters*, 2010, **105**, 136805.
50. Q. H. Wang, K. Kalantar-Zadeh, A. Kis, J. N. Coleman and M. S. Strano, *Nature Nanotechnology*, 2012, **7**, 699-712.
51. G. Eda, H. Yamaguchi, D. Voiry, T. Fujita, M. Chen and M. Chhowalla, *Nano Letters*, 2011, **11**, 5111-5116.
52. K. S. Novoselov, D. Jiang, F. Schedin, T. J. Booth, V. V. Khotkevich, S. V. Morozov and A. K. Geim, *Proceedings of the National Academy of Sciences of the United States of America*, 2005, **102**, 10451-10453.

53. A. Ayari, E. Cobas, O. Ogundadegbe and M. S. Fuhrer, *Journal of Applied Physics*, 2007, **101**, 014507.
54. B. Radisavljevic, A. Radenovic, J. Brivio, V. Giacometti and A. Kis, *Nature Nanotechnology*, 2011, **6**, 147-150.
55. Y. Yoon, K. Ganapathi and S. Salahuddin, *Nano Letters*, 2011, **11**, 3768-3773.
56. C. Anichini, W. Czepa, D. Pakulski, A. Aliprandi, A. Ciesielski and P. Samori, *Chem Soc Rev*, 2018, **47**, 4860-4908.
57. Y. F. Lin, Y. Xu, S. T. Wang, S. L. Li, M. Yamamoto, A. Aparecido-Ferreira, W. Li, H. Sun, S. Nakaharai, W. B. Jian, K. Ueno and K. Tsukagoshi, *Adv Mater*, 2014, **26**, 3263-3269.
58. M. Acerce, D. Voiry and M. Chhowalla, *Nature Nanotechnology*, 2015, **10**, 313-318.
59. N. Thi Xuyen and J.-M. Ting, *Chemistry – A European Journal*, 2017, **23**, 17348-17355.
60. D. Wang, Y. Xiao, X. Luo, Z. Wu, Y.-J. Wang and B. Fang, *ACS Sustainable Chemistry & Engineering*, 2017, **5**, 2509-2515.
61. J. M. Soon and K. P. Loh, *Electrochemical and Solid-State Letters*, 2007, **10**, A250.
62. A. N. Enyashin, L. Yadgarov, L. Houben, I. Popov, M. Weidenbach, R. Tenne, M. Bar-Sadan and G. Seifert, *The Journal of Physical Chemistry C*, 2011, **115**, 24586-24591.
63. X. Geng, W. Sun, W. Wu, B. Chen, A. Al-Hilo, M. Benamara, H. Zhu, F. Watanabe, J. Cui and T.-p. Chen, *Nature Communications*, 2016, **7**, 10672.
64. M. Calandra, *Physical Review B*, 2013, **88**, 245428.
65. N. H. Attanayake, L. Dheer, A. C. Thenuwara, S. C. Abeyweera, C. Collins, U. V. Waghmare and D. R. Strongin, *ChemElectroChem*, 2020, **7**, 3606-3615.
66. D. B. Putungan, S.-H. Lin and J.-L. Kuo, *Physical Chemistry Chemical Physics*, 2015, **17**, 21702-21708.
67. D. B. Sulas-Kern, E. M. Miller and J. L. Blackburn, *Energy & Environmental Science*, 2020, **13**, 2684-2740.
68. S. Manzeli, D. Ovchinnikov, D. Pasquier, O. V. Yazyev and A. Kis, *Nature Reviews Materials*, 2017, **2**, 17033.
69. H. Li, M. E. Pam, Y. Shi and H. Y. Yang, *FlatChem*, 2017, **4**, 48-53.
70. K. Hantanasirisakul and Y. Gogotsi, *Advanced Materials*, 2018, **30**, 1804779.
71. B. Anasori, M. R. Lukatskaya and Y. Gogotsi, *Nature Reviews Materials*, 2017, **2**, 16098.
72. M. Naguib, V. N. Mochalin, M. W. Barsoum and Y. Gogotsi, *Advanced Materials*, 2014, **26**, 992-1005.
73. W. Hong, B. C. Wyatt, S. K. Nemani and B. Anasori, *MRS Bulletin*, 2020, **45**, 850-861.
74. Á. Morales-García, M. Mayans-Llorach, F. Viñes and F. Illas, *Physical Chemistry Chemical Physics*, 2019, **21**, 23136-23142.
75. S. M. Eichfeld, L. Hossain, Y.-C. Lin, A. F. Piasecki, B. Kupp, A. G. Birdwell, R. A. Burke, N. Lu, X. Peng, J. Li, A. Azcatl, S. McDonnell, R. M. Wallace, M. J. Kim, T. S. Mayer, J. M. Redwing and J. A. Robinson, *ACS Nano*, 2015, **9**, 2080-2087.
76. J. D. Gouveia, F. Viñes, F. Illas and J. R. B. Gomes, *Physical Review Materials*, 2020, **4**, 054003.
77. P. Urbankowski, B. Anasori, T. Makaryan, D. Er, S. Kota, P. L. Walsh, M. Zhao, V. B. Shenoy, M. W. Barsoum and Y. Gogotsi, *Nanoscale*, 2016, **8**, 11385-11391.
78. Y. Xie and P. R. C. Kent, *Physical Review B*, 2013, **87**, 235441.
79. I. R. Shein and A. L. Ivanovskii, *Computational Materials Science*, 2012, **65**, 104-114.

80. I. Persson, J. Halim, H. Lind, T. W. Hansen, J. B. Wagner, L.-Å. Näslund, V. Darakchieva, J. Palisaitis, J. Rosen and P. O. Å. Persson, *Advanced Materials*, 2019, **31**, 1805472.
81. X. Sang, Y. Xie, M.-W. Lin, M. Alhabeb, K. L. Van Aken, Y. Gogotsi, P. R. C. Kent, K. Xiao and R. R. Unocic, *ACS Nano*, 2016, **10**, 9193-9200.
82. J. L. Hart, K. Hantanasirisakul, A. C. Lang, B. Anasori, D. Pinto, Y. Pivak, J. T. van Omme, S. J. May, Y. Gogotsi and M. L. Taheri, *Nature Communications*, 2019, **10**, 522.
83. J. D. Gouveia, Á. Morales-García, F. Viñes, J. R. B. Gomes and F. Illas, *ACS Catalysis*, 2020, **10**, 5049-5056.
84. S. Posada-Pérez, P. J. Ramírez, R. A. Gutiérrez, D. J. Stacchiola, F. Viñes, P. Liu, F. Illas and J. A. Rodriguez, *Catalysis Science & Technology*, 2016, **6**, 6766-6777.
85. A. Kurlov, E. B. Deeva, P. M. Abdala, D. Lebedev, A. Tsoukalou, A. Comas-Vives, A. Fedorov and C. R. Muller, *Nat Commun*, 2020, **11**, 4920.
86. J. A. Wilson and A. D. Yoffe, *Advances in Physics*, 1969, **18**, 193-335.
87. M. M. Benameur, B. Radisavljevic, J. S. Héron, S. Sahoo, H. Berger and A. Kis, *Nanotechnology*, 2011, **22**, 125706.
88. E. D. Grayfer, M. N. Kozlova and V. E. Fedorov, *Advances in Colloid and Interface Science*, 2017, **245**, 40-61.
89. G. Cunningham, M. Lotya, C. S. Cucinotta, S. Sanvito, S. D. Bergin, R. Menzel, M. S. P. Shaffer and J. N. Coleman, *ACS Nano*, 2012, **6**, 3468-3480.
90. R. J. Smith, P. J. King, M. Lotya, C. Wirtz, U. Khan, S. De, A. O'Neill, G. S. Duesberg, J. C. Grunlan, G. Moriarty, J. Chen, J. Wang, A. I. Minett, V. Nicolosi and J. N. Coleman, *Advanced Materials*, 2011, **23**, 3944-3948.
91. H. S. S. Ramakrishna Matte, A. Gomathi, A. K. Manna, D. J. Late, R. Datta, S. K. Pati and C. N. R. Rao, *Angewandte Chemie International Edition*, 2010, **49**, 4059-4062.
92. U. Gupta, B. S. Naidu, U. Maitra, A. Singh, S. N. Shirodkar, U. V. Waghmare and C. N. R. Rao, *APL Materials*, 2014, **2**, 092802.
93. M. A. Py and R. R. Haering, *Canadian Journal of Physics*, 1983, **61**, 76-84.
94. C. Lin, X. Zhu, J. Feng, C. Wu, S. Hu, J. Peng, Y. Guo, L. Peng, J. Zhao, J. Huang, J. Yang and Y. Xie, *Journal of the American Chemical Society*, 2013, **135**, 5144-5151.
95. S. N. Patel and A. A. Balchin, *Journal of Materials Science*, 1985, **20**, 917-921.
96. Y.-H. Lee, X.-Q. Zhang, W. Zhang, M.-T. Chang, C.-T. Lin, K.-D. Chang, Y.-C. Yu, J. T.-W. Wang, C.-S. Chang, L.-J. Li and T.-W. Lin, *Advanced Materials*, 2012, **24**, 2320-2325.
97. L. K. Tan, B. Liu, J. H. Teng, S. Guo, H. Y. Low and K. P. Loh, *Nanoscale*, 2014, **6**, 10584-10588.
98. D. Fu, X. Zhao, Y.-Y. Zhang, L. Li, H. Xu, A. R. Jang, S. I. Yoon, P. Song, S. M. Poh, T. Ren, Z. Ding, W. Fu, T. J. Shin, H. S. Shin, S. T. Pantelides, W. Zhou and K. P. Loh, *Journal of the American Chemical Society*, 2017, **139**, 9392-9400.
99. J. Cheon, J. E. Gozum and G. S. Girolami, *Chemistry of Materials*, 1997, **9**, 1847-1853.
100. K. Kang, S. Xie, L. Huang, Y. Han, P. Y. Huang, K. F. Mak, C.-J. Kim, D. Muller and J. Park, *Nature*, 2015, **520**, 656-660.
101. W. K. Hofmann, *Journal of Materials Science*, 1988, **23**, 3981-3986.
102. R. Wang, S. Gao, K. Wang, M. Zhou, S. Cheng and K. Jiang, *Scientific Reports*, 2017, **7**, 7963.

103. Y. Peng, Z. Meng, C. Zhong, J. Lu, W. Yu, Z. Yang and Y. Qian, *Journal of Solid State Chemistry*, 2001, **159**, 170-173.
104. L. Ye, H. Xu, D. Zhang and S. Chen, *Materials Research Bulletin*, 2014, **55**, 221-228.
105. J. Zhang, T. Wang, P. Liu, S. Liu, R. Dong, X. Zhuang, M. Chen and X. Feng, *Energy & Environmental Science*, 2016, **9**, 2789-2793.
106. D. Wang, Z. Pan, Z. Wu, Z. Wang and Z. Liu, *Journal of Power Sources*, 2014, **264**, 229-234.
107. N. Zhang, S. Gan, T. Wu, W. Ma, D. Han and L. Niu, *ACS Applied Materials & Interfaces*, 2015, **7**, 12193-12202.
108. Y. Yan, B. Xia, N. Li, Z. Xu, A. Fisher and X. Wang, *Journal of Materials Chemistry A*, 2015, **3**, 131-135.
109. H. Yuan, J. Li, C. Yuan and Z. He, *ChemElectroChem*, 2014, **1**, 1828-1833.
110. K. Zhou, J. Liu, Y. Shi, S. Jiang, D. Wang, Y. Hu and Z. Gui, *ACS Applied Materials & Interfaces*, 2015, **7**, 6070-6081.
111. Y. Li, H. Wang, L. Xie, Y. Liang, G. Hong and H. Dai, *Journal of the American Chemical Society*, 2011, **133**, 7296-7299.
112. A. Liu, L. Zhao, J. Zhang, L. Lin and H. Wu, *ACS Applied Materials & Interfaces*, 2016, **8**, 25210-25218.
113. M. Chatti, T. Gengenbach, R. King, L. Spiccia and A. N. Simonov, *Chemistry of Materials*, 2017, **29**, 3092-3099.
114. Y. Sun, F. Alimohammadi, D. Zhang and G. Guo, *Nano Letters*, 2017, **17**, 1963-1969.
115. X. Zhao, H. Zhu and X. Yang, *Nanoscale*, 2014, **6**, 10680-10685.
116. N. H. Attanayake, S. C. Abeyweera, A. C. Thenuwara, B. Anasori, Y. Gogotsi, Y. Sun and D. R. Strongin, *Journal of Materials Chemistry A*, 2018, **6**, 16882-16889.
117. F. Alimohammadi, M. Sharifian Gh, N. H. Attanayake, A. C. Thenuwara, Y. Gogotsi, B. Anasori and D. R. Strongin, *Langmuir*, 2018, **34**, 7192-7200.
118. J. Liu, Y. Liu, D. Xu, Y. Zhu, W. Peng, Y. Li, F. Zhang and X. Fan, *Applied Catalysis B: Environmental*, 2019, **241**, 89-94.
119. L. Huang, L. Ai, M. Wang, J. Jiang and S. Wang, *International Journal of Hydrogen Energy*, 2019, **44**, 965-976.
120. S. Jiao and L. Liu, *Industrial & Engineering Chemistry Research*, 2019, **58**, 18141-18148.
121. K. Huang, C. Li, H. Li, G. Ren, L. Wang, W. Wang and X. Meng, *ACS Applied Nano Materials*, 2020, **3**, 9581-9603.
122. F. Ma, Y. Liang, P. Zhou, F. Tong, Z. Wang, P. Wang, Y. Liu, Y. Dai, Z. Zheng and B. Huang, *Materials Chemistry and Physics*, 2020, **244**, 122642.
123. I. Roger, R. Moca, H. N. Miras, K. G. Crawford, D. A. J. Moran, A. Y. Ganin and M. D. Symes, *Journal of Materials Chemistry A*, 2017, **5**, 1472-1480.
124. B. Soundiraraju and B. K. George, *ACS Nano*, 2017, **11**, 8892-8900.
125. R. Meshkian, L.-Å. Näslund, J. Halim, J. Lu, M. W. Barsoum and J. Rosen, *Scripta Materialia*, 2015, **108**, 147-150.
126. J. Halim, S. Kota, M. R. Lukatskaya, M. Naguib, M.-Q. Zhao, E. J. Moon, J. Pitock, J. Nanda, S. J. May, Y. Gogotsi and M. W. Barsoum, *Advanced Functional Materials*, 2016, **26**, 3118-3127.

127. Z. W. Seh, K. D. Fredrickson, B. Anasori, J. Kibsgaard, A. L. Strickler, M. R. Lukatskaya, Y. Gogotsi, T. F. Jaramillo and A. Vojvodic, *ACS Energy Letters*, 2016, **1**, 589-594.
128. J. Zhou, X. Zha, F. Y. Chen, Q. Ye, P. Eklund, S. Du and Q. Huang, *Angewandte Chemie International Edition*, 2016, **55**, 5008-5013.
129. X. Xiao, H. Wang, P. Urbankowski and Y. Gogotsi, *Chemical Society Reviews*, 2018, **47**, 8744-8765.
130. M. Naguib, O. Mashtalir, J. Carle, V. Presser, J. Lu, L. Hultman, Y. Gogotsi and M. W. Barsoum, *ACS Nano*, 2012, **6**, 1322-1331.
131. D. Dolz, Á. Morales-García, F. Viñes and F. Illas, *Nanomaterials*, 2021, **11**, 127.
132. M. Aresta, A. Dibenedetto and A. Angelini, *Chem Rev*, 2014, **114**, 1709-1742.
133. L. Wang, W. Chen, D. Zhang, Y. Du, R. Amal, S. Qiao, J. Wu and Z. Yin, *Chem Soc Rev*, 2019, **48**, 5310-5349.
134. N. Li, X. Chen, W. J. Ong, D. R. MacFarlane, X. Zhao, A. K. Cheetham and C. Sun, *ACS Nano*, 2017, **11**, 10825-10833.
135. L. Liu and A. Corma, *Chem Rev*, 2018, **118**, 4981-5079.
136. A. J. Meier, A. Garg, B. Sutter, J. N. Kuhn and V. R. Bhethanabotla, *ACS Sustainable Chemistry & Engineering*, 2018, **7**, 265-275.
137. A. Ali and W. C. Oh, *Sci Rep*, 2017, **7**, 1867.
138. Á. Morales-García, A. Fernández-Fernández, F. Viñes and F. Illas, *Journal of Materials Chemistry A*, 2018, **6**, 3381-3385.
139. S. Xie, Q. Zhang, G. Liu and Y. Wang, *Chem Commun (Camb)*, 2016, **52**, 35-59.
140. K. P. Kuhl, E. R. Cave, D. N. Abram and T. F. Jaramillo, *Energy & Environmental Science*, 2012, **5**.
141. A. A. Peterson and J. K. Nørskov, *The Journal of Physical Chemistry Letters*, 2012, **3**, 251-258.
142. S. N. Habisreutinger, L. Schmidt-Mende and J. K. Stolarczyk, *Angew Chem Int Ed Engl*, 2013, **52**, 7372-7408.
143. A. J. Garza, A. T. Bell and M. Head-Gordon, *ACS Catalysis*, 2018, **8**, 1490-1499.
144. S. A. Francis, J. M. Velazquez, I. M. Ferrer, D. A. Torelli, D. Guevarra, M. T. McDowell, K. Sun, X. Zhou, F. H. Saadi, J. John, M. H. Richter, F. P. Hyler, K. M. Papadantonakis, B. S. Brunschwig and N. S. Lewis, *Chemistry of Materials*, 2018, **30**, 4902-4908.
145. A. Vasileff, Y. Zhu, X. Zhi, Y. Zhao, L. Ge, H. M. Chen, Y. Zheng and S. Z. Qiao, *Angewandte Chemie*, 2020, **132**, 19817-19821.
146. K. Chan, C. Tsai, H. A. Hansen and J. K. Nørskov, *ChemCatChem*, 2014, **6**, 1899-1905.
147. F. Abild-Pedersen, J. Greeley, F. Studt, J. Rossmeisl, T. R. Munter, P. G. Moses, E. Skulason, T. Bligaard and J. K. Norskov, *Phys Rev Lett*, 2007, **99**, 016105.
148. F. Calle-Vallejo, D. Loffreda, M. T. Koper and P. Sautet, *Nat Chem*, 2015, **7**, 403-410.
149. X. Hong, K. Chan, C. Tsai and J. K. Nørskov, *ACS Catalysis*, 2016, **6**, 4428-4437.
150. K. Chan, C. Tsai, H. A. Hansen and J. K. Nørskov, *ChemCatChem*, 2014, **6**, 1899-1905.
151. X. Zhang, Z. Zhang, J. Li, X. Zhao, D. Wu and Z. Zhou, *Journal of Materials Chemistry A*, 2017, **5**, 12899-12903.
152. H. Chen, A. D. Handoko, J. Xiao, X. Feng, Y. Fan, T. Wang, D. Legut, Z. W. Seh and Q. Zhang, *ACS Appl Mater Interfaces*, 2019, **11**, 36571-36579.

153. Z. Wang, V. Kochat, P. Pandey, S. Kashyap, S. Chattopadhyay, A. Samanta, S. Sarkar, P. Manimunda, X. Zhang, S. Asif, A. K. Singh, K. Chattopadhyay, C. S. Tiwary and P. M. Ajayan, *Advanced Materials*, 2017, **29**, 1700364.
154. P. Abbasi, M. Asadi, C. Liu, S. Sharifi-Asl, B. Sayahpour, A. Behranginia, P. Zapol, R. Shahbazian-Yassar, L. A. Curtiss and A. Salehi-Khojin, *ACS Nano*, 2016, **11**, 453-460.
155. M. Asadi, B. Kumar, A. Behranginia, B. A. Rosen, A. Baskin, N. Repnin, D. Pisasale, P. Phillips, W. Zhu, R. Haasch, R. F. Klie, P. Kral, J. Abiade and A. Salehi-Khojin, *Nat Commun*, 2014, **5**, 4470.
156. Y. Ji, J. K. Nørskov and K. Chan, *The Journal of Physical Chemistry C*, 2019, **123**, 4256-4261.
157. S. Choi, Z. Shaolin and W. Yang, *Journal of the Korean Physical Society*, 2014, **64**, 1550-1555.
158. K. Lv, C. Teng, M. Shi, Y. Yuan, Y. Zhu, J. Wang, Z. Kong, X. Lu and Y. Zhu, *Advanced Functional Materials*, 2018, **28**.
159. M. Asadi, K. Kim, C. Liu, A. V. Addepalli, P. Abbasi, P. Yasaei, P. Phillips, A. Behranginia, J. M. Cerrato, R. Haasch, P. Zapol, B. Kumar, R. F. Klie, J. Abiade, L. A. Curtiss and A. Salehi-Khojin, *Science*, 2016, **353**, 467-470.
160. B. A. Rosen, J. L. Haan, P. Mukherjee, B. Braunschweig, W. Zhu, A. Salehi-Khojin, D. D. Dlott and R. I. Masel, *The Journal of Physical Chemistry C*, 2012, **116**, 15307-15312.
161. J. He, X. Liu, H. Liu, Z. Zhao, Y. Ding and J. Luo, *Journal of Catalysis*, 2018, **364**, 125-130.
162. M. E. Dry and J. C. Hoogendoorn, *Catalysis Reviews*, 2006, **23**, 265-278.
163. M. Yasin, Y. Jeong, S. Park, J. Jeong, E. Y. Lee, R. W. Lovitt, B. H. Kim, J. Lee and I. S. Chang, *Bioresour Technol*, 2015, **177**, 361-374.
164. M. Mattinen, P. J. King, L. Khriachtchev, K. Meinander, J. T. Gibbon, V. R. Dhanak, J. Raisanen, M. Ritala and M. Leskela, *Small*, 2018, **14**, e1800547.
165. J. Gu, C. S. Hsu, L. Bai, H. M. Chen and X. Hu, *Science*, 2019, **364**, 1091-1094.
166. X. Mao, L. Wang, Y. Xu and Y. Li, *The Journal of Physical Chemistry C*, 2020, **124**, 10523-10529.
167. A. Zhang, R. He, H. Li, Y. Chen, T. Kong, K. Li, H. Ju, J. Zhu, W. Zhu and J. Zeng, *Angew Chem Int Ed Engl*, 2018, **57**, 10954-10958.
168. K. Lv, W. Suo, M. Shao, Y. Zhu, X. Wang, J. Feng, M. Fang and Y. Zhu, *Nano Energy*, 2019, **63**.
169. J. Cavin, A. Ahmadiparidari, L. Majidi, A. S. Thind, S. N. Misal, A. Prajapati, Z. Hemmat, S. Rastegar, A. Beukelman, M. R. Singh, K. A. Unocic, A. Salehi-Khojin and R. Mishra, *Adv Mater*, 2021, **33**, e2100347.
170. J. Xu, X. Li, W. Liu, Y. Sun, Z. Ju, T. Yao, C. Wang, H. Ju, J. Zhu, S. Wei and Y. Xie, *Angew Chem Int Ed Engl*, 2017, **56**, 9121-9125.
171. J. Xu, S. Lai, M. Hu, S. Ge, R. Xie, F. Li, D. Hua, H. Xu, H. Zhou, R. Wu, J. Fu, Y. Qiu, J. He, C. Li, H. Liu, Y. Liu, J. Sun, X. Liu and J. Luo, *Small Methods*, 2020, **4**.
172. M. A. Lukowski, A. S. Daniel, F. Meng, A. Forticaux, L. Li and S. Jin, *J Am Chem Soc*, 2013, **135**, 10274-10277.
173. Q. Ding, F. Meng, C. R. English, M. Caban-Acevedo, M. J. Shearer, D. Liang, A. S. Daniel, R. J. Hamers and S. Jin, *J Am Chem Soc*, 2014, **136**, 8504-8507.

174. A. Aljabour, H. Coskun, X. Zheng, M. G. Kibria, M. Strobel, S. Hild, M. Kehrer, D. Stifter, E. H. Sargent and P. Stadler, *ACS Catalysis*, 2019, **10**, 66-72.
175. G. Shi, L. Yu, X. Ba, X. Zhang, J. Zhou and Y. Yu, *Dalton Trans*, 2017, **46**, 10569-10577.
176. H. Li, X. Liu, S. Chen, D. Yang, Q. Zhang, L. Song, H. Xiao, Q. Zhang, L. Gu and X. Wang, *Advanced Energy Materials*, 2019, **9**.
177. S. Hong, C. K. Rhee and Y. Sohn, *Catalysts*, 2019, **9**.
178. K. F. Mak, C. Lee, J. Hone, J. Shan and T. F. Heinz, *Phys Rev Lett*, 2010, **105**, 136805.
179. C. K. Sumesh and S. C. Peter, *Dalton Trans*, 2019, **48**, 12772-12802.
180. T. F. Jaramillo, K. P. Jorgensen, J. Bonde, J. H. Nielsen, S. Horch and I. Chorkendorff, *Science*, 2007, **317**, 100-102.
181. R. A. Geioushy, S. M. El-Sheikh, I. M. Hegazy, A. Shawky, S. El-Sherbiny and A.-H. T. Kandil, *Materials Research Bulletin*, 2019, **118**.
182. W. He, X. Wu, Y. Li, J. Xiong, Z. Tang, Y. Wei, Z. Zhao, X. Zhang and J. Liu, *Chinese Chemical Letters*, 2020, **31**, 2774-2778.
183. P. De Luna, R. Quintero-Bermudez, C.-T. Dinh, M. B. Ross, O. S. Bushuyev, P. Todorović, T. Regier, S. O. Kelley, P. Yang and E. H. Sargent, *Nature Catalysis*, 2018, **1**, 103-110.
184. L. Jing, Y. Xu, Z. Chen, M. He, M. Xie, J. Liu, H. Xu, S. Huang and H. Li, *ACS Sustainable Chemistry & Engineering*, 2018, **6**, 5132-5141.
185. A. McLaren, T. Valdes-Solis, G. Li and S. C. Tsang, *J Am Chem Soc*, 2009, **131**, 12540-12541.
186. T. Billo, I. Shown, A. k. Anbalagan, T. A. Effendi, A. Sabbah, F.-Y. Fu, C.-M. Chu, W.-Y. Woon, R.-S. Chen, C.-H. Lee, K.-H. Chen and L.-C. Chen, *Nano Energy*, 2020, **72**.
187. W. Dai, J. Yu, Y. Deng, X. Hu, T. Wang and X. Luo, *Applied Surface Science*, 2017, **403**, 230-239.
188. W. Tu, Y. Li, L. Kuai, Y. Zhou, Q. Xu, H. Li, X. Wang, M. Xiao and Z. Zou, *Nanoscale*, 2017, **9**, 9065-9070.
189. X. Jiao, X. Li, X. Jin, Y. Sun, J. Xu, L. Liang, H. Ju, J. Zhu, Y. Pan, W. Yan, Y. Lin and Y. Xie, *J Am Chem Soc*, 2017, **139**, 18044-18051.
190. F. You, J. Wan, J. Qi, D. Mao, N. Yang, Q. Zhang, L. Gu and D. Wang, *Angew Chem Int Ed Engl*, 2020, **59**, 721-724.
191. Q. Zhang and L. Fu, *Chem*, 2019, **5**, 505-525.
192. W. Wang, J. Zhang, Q. Zhang, S. Wan, X. Zhu, Q. Zhang, W. Wang, Y. Zhang, Y. Liu and L. Fu, *Adv Mater*, 2018, **30**, e1804559.
193. Y. Zhou, E. Song, J. Zhou, J. Lin, R. Ma, Y. Wang, W. Qiu, R. Shen, K. Suenaga, Q. Liu, J. Wang, Z. Liu and J. Liu, *ACS Nano*, 2018, **12**, 4486-4493.
194. Y. Zhang, D. Yao, B. Xia, H. Xu, Y. Tang, K. Davey, J. Ran and S.-Z. Qiao, *Small Science*, 2021, **1**.
195. X. Wang, Z. Li, J. Shi and Y. Yu, *Chem Rev*, 2014, **114**, 9346-9384.
196. F. Xu, B. Zhu, B. Cheng, J. Yu and J. Xu, *Advanced Optical Materials*, 2018, **6**, 1800911.
197. Q. Fu, X. Wang, J. Zhou, J. Xia, Q. Zeng, D. Lv, C. Zhu, X. Wang, Y. Shen, X. Li, Y. Hua, F. Liu, Z. Shen, C. Jin and Z. Liu, *Chemistry of Materials*, 2018, **30**, 4001-4007.
198. J. Li, X. Yang, Y. Liu, B. Huang, R. Wu, Z. Zhang, B. Zhao, H. Ma, W. Dang, Z. Wei, K. Wang, Z. Lin, X. Yan, M. Sun, B. Li, X. Pan, J. Luo, G. Zhang, Y. Liu, Y. Huang, X. Duan and X. Duan, *Nature*, 2020, **579**, 368-374.

199. Z. Luo, Y. Li, F. Guo, K. Zhang, K. Liu, W. Jia, Y. Zhao and Y. Sun, *Energies*, 2020, **13**.
200. Y. Wang, Z. Zhang, L. Zhang, Z. Luo, J. Shen, H. Lin, J. Long, J. C. S. Wu, X. Fu, X. Wang and C. Li, *Journal of the American Chemical Society*, 2018, **140**, 14595-14598.
201. H. Qin, R. T. Guo, X. Y. Liu, W. G. Pan, Z. Y. Wang, X. Shi, J. Y. Tang and C. Y. Huang, *Dalton Trans*, 2018, **47**, 15155-15163.
202. S. Yin, J. Li, L. Sun, X. Li, D. Shen, X. Song, P. Huo, H. Wang and Y. Yan, *Inorg Chem*, 2019, **58**, 15590-15601.
203. S. Guo, P. Yang, Y. Zhao, X. Yu, Y. Wu, H. Zhang, B. Yu, B. Han, M. W. George and Z. Liu, *ChemSusChem*, 2020, **13**, 6278-6283.
204. S. Yin, L. Sun, Y. Zhou, X. Li, J. Li, X. Song, P. Huo, H. Wang and Y. Yan, *Chemical Engineering Journal*, 2021, **406**.
205. A. Han, M. Li, S. Zhang, X. Zhu, J. Han, Q. Ge and H. Wang, *Catalysts*, 2019, **9**.
206. H. She, H. Zhou, L. Li, Z. Zhao, M. Jiang, J. Huang, L. Wang and Q. Wang, *ACS Sustainable Chemistry & Engineering*, 2018, **7**, 650-659.
207. P. Puthiaraj, Y.-R. Lee, S. Zhang and W.-S. Ahn, *Journal of Materials Chemistry A*, 2016, **4**, 16288-16311.
208. X. Zhu, C. Tian, G. M. Veith, C. W. Abney, J. Dehaudt and S. Dai, *J Am Chem Soc*, 2016, **138**, 11497-11500.
209. H. Jin, C. Guo, X. Liu, J. Liu, A. Vasileff, Y. Jiao, Y. Zheng and S. Z. Qiao, *Chem Rev*, 2018, **118**, 6337-6408.
210. A. D. Handoko, H. Chen, Y. Lum, Q. Zhang, B. Anasori and Z. W. Seh, *iScience*, 2020, **23**, 101181.
211. Z. Li, Doctor OF Philosophy Graduate Theses and Dissertations, Iowa State University, 2019.
212. A. D. Handoko, K. H. Khoo, T. L. Tan, H. Jin and Z. W. Seh, *Journal of Materials Chemistry A*, 2018, **6**, 21885-21890.
213. N. H. Attanayake, H. R. Banjade, A. C. Thenuwara, B. Anasori, Q. Yan and D. R. Strongin, *Chem Commun (Camb)*, 2021, **57**, 1675-1678.
214. X. Zhang, X. Zhao, D. Wu, Y. Jing and Z. Zhou, *Nanoscale*, 2015, **7**, 16020-16025.
215. M. Ye, X. Wang, E. Liu, J. Ye and D. Wang, *ChemSusChem*, 2018, **11**, 1606-1611.
216. J. Low, L. Zhang, T. Tong, B. Shen and J. Yu, *Journal of Catalysis*, 2018, **361**, 255-266.
217. S. Cao, B. Shen, T. Tong, J. Fu and J. Yu, *Advanced Functional Materials*, 2018, **28**.
218. Q. Tang, Z. Sun, S. Deng, H. Wang and Z. Wu, *J Colloid Interface Sci*, 2020, **564**, 406-417.
219. W. Chen, B. Han, Y. Xie, S. Liang, H. Deng and Z. Lin, *Chemical Engineering Journal*, 2020, **391**.
220. J. Shen, J. Shen, W. Zhang, X. Yu, H. Tang, M. Zhang, Zulfiqar and Q. Liu, *Ceramics International*, 2019, **45**, 24146-24153.
221. F. Li, L. Chen, H. Liu, D. Wang, C. Shi and H. Pan, *The Journal of Physical Chemistry C*, 2019, **123**, 22221-22227.
222. L. M. Azofra, N. Li, D. R. MacFarlane and C. Sun, *Energy & Environmental Science*, 2016, **9**, 2545-2549.
223. J. G. Chen, R. M. Crooks, L. C. Seefeldt, K. L. Bren, R. M. Bullock, M. Y. Darensbourg, P. L. Holland, B. Hoffman, M. J. Janik, A. K. Jones, M. G. Kanatzidis, P. King, K. M. Lancaster, S. V. Lymar, P. Pfromm, W. F. Schneider and R. R. Schrock, *Science*, 2018, **360**, eaar6611.

224. A. J. Martín, T. Shinagawa and J. Pérez-Ramírez, *Chem*, 2019, **5**, 263-283.
225. L. F. Greenlee, J. N. Renner and S. L. Foster, *ACS Catalysis*, 2018, **8**, 7820-7827.
226. C. Tang and S.-Z. Qiao, *Chemical Society Reviews*, 2019, **48**, 3166-3180.
227. R. Lan, J. T. S. Irvine and S. Tao, *Scientific Reports*, 2013, **3**, 1145.
228. G.-F. Chen, S. Ren, L. Zhang, H. Cheng, Y. Luo, K. Zhu, L.-X. Ding and H. Wang, *Small Methods*, 2019, **3**, 1800337.
229. M. A. Shipman and M. D. Symes, *Electrochimica Acta*, 2017, **258**, 618-622.
230. S. Z. Andersen, V. Čolić, S. Yang, J. A. Schwalbe, A. C. Nielander, J. M. McEnaney, K. Enemark-Rasmussen, J. G. Baker, A. R. Singh, B. A. Rohr, M. J. Statt, S. J. Blair, S. Mezzavilla, J. Kibsgaard, P. C. K. Vesborg, M. Cargnello, S. F. Bent, T. F. Jaramillo, I. E. L. Stephens, J. K. Nørskov and I. Chorkendorff, *Nature*, 2019, **570**, 504-508.
231. E. Skúlason, T. Bligaard, S. Gudmundsdóttir, F. Studt, J. Rossmeisl, F. Abild-Pedersen, T. Vegge, H. Jónsson and J. K. Nørskov, *Physical Chemistry Chemical Physics*, 2012, **14**, 1235-1245.
232. J. H. Montoya, C. Tsai, A. Vojvodic and J. K. Nørskov, *ChemSusChem*, 2015, **8**, 2180-2186.
233. A. J. Medford, A. Vojvodic, J. S. Hummelshøj, J. Voss, F. Abild-Pedersen, F. Studt, T. Bligaard, A. Nilsson and J. K. Nørskov, *Journal of Catalysis*, 2015, **328**, 36-42.
234. H. Oschinski, Á. Morales-García and F. Illas, *The Journal of Physical Chemistry C*, 2021, **125**, 2477-2484.
235. L. Zhang, X. Ji, X. Ren, Y. Ma, X. Shi, Z. Tian, A. M. Asiri, L. Chen, B. Tang and X. Sun, *Advanced Materials*, 2018, **30**, 1800191.
236. J. Zhao, L. Zhang, X.-Y. Xie, X. Li, Y. Ma, Q. Liu, W.-H. Fang, X. Shi, G. Cui and X. Sun, *Journal of Materials Chemistry A*, 2018, **6**, 24031-24035.
237. K. S. Exner and H. Over, *Acc Chem Res*, 2017, **50**, 1240-1247.
238. K. S. Exner, J. Anton, T. Jacob and H. Over, *Angew Chem Int Ed Engl*, 2016, **55**, 7501-7504.
239. X. Xu, X. Tian, B. Sun, Z. Liang, H. Cui, J. Tian and M. Shao, *Applied Catalysis B: Environmental*, 2020, **272**, 118984.
240. X. Li, T. Li, Y. Ma, Q. Wei, W. Qiu, H. Guo, X. Shi, P. Zhang, A. M. Asiri, L. Chen, B. Tang and X. Sun, *Advanced Energy Materials*, 2018, **8**, 1801357.
241. L. Zeng, X. Li, S. Chen, J. Wen, F. Rahmati, J. van der Zalm and A. Chen, *Nanoscale*, 2020, **12**, 6029-6036.
242. Y. Zhou, X. Yu, X. Wang, C. Chen, S. Wang and J. Zhang, *Electrochimica Acta*, 2019, **317**, 34-41.
243. L. Zeng, X. Li, S. Chen, J. Wen, W. Huang and A. Chen, *Journal of Materials Chemistry A*, 2020, **8**, 7339-7349.
244. B. H. R. Suryanto, D. Wang, L. M. Azofra, M. Harb, L. Cavallo, R. Jalili, D. R. G. Mitchell, M. Chatti and D. R. MacFarlane, *ACS Energy Letters*, 2019, **4**, 430-435.
245. S. B. Patil, H.-L. Chou, Y.-M. Chen, S.-H. Hsieh, C.-H. Chen, C.-C. Chang, S.-R. Li, Y.-C. Lee, Y.-S. Lin, H. Li, Y. J. Chang, Y.-H. Lai and D.-Y. Wang, *Journal of Materials Chemistry A*, 2021, **9**, 1230-1239.
246. X. Li, X. Ren, X. Liu, J. Zhao, X. Sun, Y. Zhang, X. Kuang, T. Yan, Q. Wei and D. Wu, *Journal of Materials Chemistry A*, 2019, **7**, 2524-2528.

247. Y. Liu, W. Wang, S. Zhang, W. Li, G. Wang, Y. Zhang, M. Han and H. Zhang, *ACS Sustainable Chemistry & Engineering*, 2020, **8**, 2320-2326.
248. K. Chu, Y. P. Liu, Y. B. Li, Y. L. Guo and Y. Tian, *ACS Appl Mater Interfaces*, 2020, **12**, 7081-7090.
249. Z. Zhao, S. Luo, P. Ma, Y. Luo, W. Wu, Y. Long and J. Ma, *ACS Sustainable Chemistry & Engineering*, 2020, **8**, 8814-8822.
250. L. Yang, H. Wang, X. Wang, W. Luo, C. Wu, C.-a. Wang and C. Xu, *Inorganic Chemistry*, 2020, **59**, 12941-12946.
251. H. Wang, J. Si, T. Zhang, Y. Li, B. Yang, Z. Li, J. Chen, Z. Wen, C. Yuan, L. Lei and Y. Hou, *Applied Catalysis B: Environmental*, 2020, **270**, 118892.
252. Q. Li, Y. Guo, Y. Tian, W. Liu and K. Chu, *Journal of Materials Chemistry A*, 2020, **8**, 16195-16202.
253. Y. Wang, A. Chen, S. Lai, X. Peng, S. Zhao, G. Hu, Y. Qiu, J. Ren, X. Liu and J. Luo, *Journal of Catalysis*, 2020, **381**, 78-83.
254. Z. Wu, R. Zhang, H. Fei, R. Liu, D. Wang and X. Liu, *Applied Surface Science*, 2020, **532**, 147372.
255. K. Jia, Y. Wang, L. Qiu, J. Gao, Q. Pan, W. Kong, X. Zhang, A. A. Alshehri, K. A. Alzahrani, B. Zhong, X. Guo and L. Yang, *Inorganic Chemistry Frontiers*, 2019, **6**, 1986-1989.
256. W. Ye, M. Arif, X. Fang, M. A. Mushtaq, X. Chen and D. Yan, *ACS Applied Materials & Interfaces*, 2019, **11**, 28809-28817.
257. H. Maimaitizi, A. Abulizi, T. Zhang, K. Okitsu and J. J. Zhu, *Ultrason Sonochem*, 2020, **63**, 104956.
258. B. Sun, Z. Liang, Y. Qian, X. Xu, Y. Han and J. Tian, *ACS Appl Mater Interfaces*, 2020, **12**, 7257-7269.
259. Y. Liu, M. Han, Q. Xiong, S. Zhang, C. Zhao, W. Gong, G. Wang, H. Zhang and H. Zhao, *Advanced Energy Materials*, 2019, **9**, 1803935.
260. L. Zeng, S. Chen, J. van der Zalm, X. Li and A. Chen, *Chemical Communications*, 2019, **55**, 7386-7389.
261. J. Liang, S. Ma, J. Li, Y. Wang, J. Wu, Q. Zhang, Z. Liu, Z. Yang, K. Qu and W. Cai, *Journal of Materials Chemistry A*, 2020, **8**, 10426-10432.
262. F. Lai, N. Chen, X. Ye, G. He, W. Zong, K. B. Holt, B. Pan, I. P. Parkin, T. Liu and R. Chen, *Advanced Functional Materials*, 2020, **30**, 1907376.
263. H. Li, S. Gu, Z. Sun, F. Guo, Y. Xie, B. Tao, X. He, W. Zhang and H. Chang, *Journal of Materials Chemistry A*, 2020, **8**, 13038-13048.
264. J. Xia, S.-Z. Yang, B. Wang, P. Wu, I. Popovs, H. Li, S. Irle, S. Dai and H. Zhu, *Nano Energy*, 2020, **72**, 104681.
265. Y. Luo, G.-F. Chen, L. Ding, X. Chen, L.-X. Ding and H. Wang, *Joule*, 2019, **3**, 279-289.
266. Y. Guo, T. Wang, Q. Yang, X. Li, H. Li, Y. Wang, T. Jiao, Z. Huang, B. Dong, W. Zhang, J. Fan and C. Zhi, *ACS Nano*, 2020, **14**, 9089-9097.
267. Y. Fang, Z. Liu, J. Han, Z. Jin, Y. Han, F. Wang, Y. Niu, Y. Wu and Y. Xu, *Advanced Energy Materials*, 2019, **9**, 1803406.
268. W. Peng, M. Luo, X. Xu, K. Jiang, M. Peng, D. Chen, T. S. Chan and Y. Tan, *Advanced Energy Materials*, 2020, **10**, 2001364.

269. D. Liu, G. Zhang, Q. Ji, Y. Zhang and J. Li, *ACS Applied Materials & Interfaces*, 2019, **11**, 25758-25765.
270. A. Liu, M. Gao, X. Ren, F. Meng, Y. Yang, Q. Yang, W. Guan, L. Gao, X. Liang and T. Ma, *Nanoscale*, 2020, **12**, 10933-10938.
271. T. Hou, Q. Li, Y. Zhang, W. Zhu, K. Yu, S. Wang, Q. Xu, S. Liang and L. Wang, *Applied Catalysis B: Environmental*, 2020, **273**, 119072.
272. Y. Liao, J. Qian, G. Xie, Q. Han, W. Dang, Y. Wang, L. Lv, S. Zhao, L. Luo, W. Zhang, H.-Y. Jiang and J. Tang, *Applied Catalysis B: Environmental*, 2020, **273**, 119054.
273. C. Hao, Y. Liao, Y. Wu, Y. An, J. Lin, Z. Gu, M. Jiang, S. Hu and X. Wang, *Journal of Physics and Chemistry of Solids*, 2020, **136**, 109141.
274. C. E. Shuck, A. Sarycheva, M. Anayee, A. Levitt, Y. Zhu, S. Uzun, V. Balitskiy, V. Zahorodna, O. Gogotsi and Y. Gogotsi, *Advanced Engineering Materials*, 2020, **22**.
275. A. Kozhakhmetov, R. Torsi, C. Y. Chen and J. A. Robinson, *Journal of Physics: Materials*, 2020, **4**.
276. F. Rehman, M. Delowar Hossain, A. Tyagi, D. Lu, B. Yuan and Z. Luo, *Materials Today*, 2021, **44**, 136-167.
277. T. N. Nguyen and C. T. Dinh, *Chem Soc Rev*, 2020, **49**, 7488-7504.

Converting carbon dioxide into useful C-based products and revolutionizing industrial ammonia generation are two scientific grand challenges with the potential to solve critical global energy and greenhouse gas threats. In this review article, we discuss (photo)electrocatalytic and photocatalytic methods as potential solutions to these grand challenges, specifically by addressing state-of-the-art of 2D transition metal dichalcogenide (TMDC) and transition metal nitrides/carbide (MXene) catalysts. We address the key advantages and challenges for these highly tunable 2D materials for carbon dioxide and nitrogen reduction reactions, and how defects, phases, edge sites, interfaces, doping, and functional groups can be engineered to improve catalytic performance for carbon dioxide and nitrogen reduction reactions. Finally, we provide our perspective on advancing these two material classes within (photo)electrocatalytic and photocatalytic setups before they could be considered industrially viable catalysts. Overall, this review article highlights both key (photo)electrocatalytic and photocatalytic trends and lessons learned for improving 2D TMDC and MXene catalysts for carbon dioxide and nitrogen reduction reactions, with an eye towards next-generation technologies with lower energetic costs and greenhouse gas emissions.